

Studies on phase equilibrium  
states and spatial distributions  
of water-soluble microparticles  
preserved in polar ice sheets

極地氷床に存在する水溶性微粒子の相平衡状態および分布  
に関する研究

Toshimitsu Sakurai

Ph.D. Dissertation

Graduate School of Environmental Science

Hokkaido University

2010



# Contents

## Abstract

1	Introduction .....	1
1.1	Background .....	1
1.2	Previous studies of the existence of water-soluble impurities in ice cores .....	3
1.3	Aim of this study .....	10
2	Methods .....	13
2.1	Ice preparation .....	13
2.1.1	Antarctic ice .....	13
2.1.2	Greenland ice .....	14
2.2	Optical characterization .....	14
2.3	Micro-Raman spectroscopy .....	15
2.3.1	Setup of Cryostat .....	15
2.3.2	Raman spectroscopy .....	17
2.3.3	Reference samples .....	20
2.3.4	Ice preparation .....	23
2.3.5	Measuring microparticles in polar ice .....	23
2.4	Differential Scanning Calorimetry (DSC) .....	27
2.4.1	Setup .....	27
2.4.2	Analytical technique of DSC curve .....	28
2.5	SEM-EDS .....	31
2.6	Ion Chromatography .....	31
3	Changes of chemical form of the microparticles during Termination I .....	33
3.1	Purpose .....	33
3.2	Number of microparticles .....	33
3.3	Chemical form of microparticles .....	34
3.4	Enthalpy of fusion in binary phase system .....	37
4	$(\text{CH}_3\text{SO}_3)_2\text{Mg} \cdot n\text{H}_2\text{O}$ found in the Dome Fuji ice core .....	41
4.1	Purpose .....	41
4.2	Raman spectra of methanesulfonate salts .....	41
4.3	Chemical form of methanesulfonate salts in the ice core .....	43
4.4	Binary phase diagram of methanesulfonate salts .....	44
4.5	The formation mechanism of $(\text{CH}_3\text{SO}_3)_2\text{Mg} \cdot n\text{H}_2\text{O}$ .....	46

4.5.1	In the firn of ice sheet, Antarctica-----	46
4.5.2	In the air of Antarctica's ice edge -----	47
5	Finding of sulfate salts as liquid microparticles in the Dome Fuji ice core -----	49
5.1	Purpose -----	49
5.2	Raman spectroscopy of microparticles in the ice core -----	49
5.3	Ternary phase diagram of Na <sub>2</sub> SO <sub>4</sub> - HCl - H <sub>2</sub> O -----	56
5.4	Chemical form of the sulfate microparticles with Raman peak at 984cm <sup>-1</sup> -----	58
5.5	The implication of finding liquid sulfate in the ice sheet -----	59
6	Spatial distribution of microparticles in Dome Fuji ice core -----	63
6.1	Purpose -----	63
6.2	The diameter and the number concentration of microparticles -----	63
6.3	Spatial distribution of microparticles -----	67
7	Microparticles in the GRIP ice core, Greenland -----	73
7.1	Purpose -----	73
7.2	Number concentration and diameter of microparticles -----	73
7.3	Chemical form of microparticles -----	75
7.4	SEM-EDS -----	76
7.5	Ion chromatography -----	77
7.6	Microparticles identified by Raman spectroscopy -----	78
7.7	Importance of the findings of water-soluble microparticles in GRIP ice core--	79
7.7.1	Ion concentration estimates based on microparticles volume -----	80
7.7.2	Significance of carbon dioxide -----	80
7.7.3	Significance of sulfate and carbonate salts -----	81
8	Summary-----	83
(1)	Chemical forms of water-soluble microparticles in the Antarctic and Greenland ice cores as functions of climate-----	83
(2)	Nature and behavior of water-soluble microparticles as a function of depth---	84
(3)	Miscellaneous remarks-----	86
(4)	Future prospects-----	88
	Acknowledgements-----	91
	References -----	93

# Abstract

The most fundamental aspects of Earth's climate history over the last several hundred thousand years have been preserved in the ice cores retrieved from Greenland and Antarctica. The variability of the ions in these ice cores shows the climate history and that the water-soluble aerosols in the atmosphere of the past could trigger climate changes that cause interglacial and glacial cycles. However, when reconstructing a reliable history from these ions, we must know their chemical form in the ice and how these chemicals behaved during their preservation. Over the past quarter century, the existence and reliability of ions as proxies of climate histories have been widely discussed; it has been speculated that the ions exist as liquid and/or acids on grain boundaries and form a connected vein network between ice grains, which may disturb climate histories. A recent study using the shallower depth of the Dome Fuji ice core from Antarctica showed that several ions exist not as liquid but as solid salts that form microparticles within the ice grains. The behavior of ions in ice sheet progressed rapidly during these years.

This study is based on the recent study results and clarifies the behavior of ions in terms of the phase equilibrium state of salts. In particular, for deep parts of ice sheets, the temperature of ice increases to the pressure melting point of ice due to geothermal heat flux from the bedrock. The temperature is a significant factor when discussing the reliability of past climate histories because the melting of salts may cause a disturbance in the ice, as previously discussed.

In this study, an optical microscope was used to measure the number concentration, and spatial distribution of microparticles. Micro-Raman spectroscopy was used to measure the chemical form of microparticles, and differential scanning calorimetry (DSC) was used to measure the equilibrium states and melting behavior (eutectic temperature) of salts in ice. In particular, this study devised a cryostat equipped with micro-Raman spectroscopy; it can measure cooling from room temperature to  $-90^{\circ}\text{C}$  with high accuracy and measures not just a particular frequency of Raman but also the lower frequencies to determine the phase states of microparticles in the ice sheet. For the DSC measurements, this study measured the binary and ternary phase equilibrium states of the salts. These devices can be used to establish a measurement system for chemical form of microparticles in ice sheets.

The results were as follows:

1. The measurement of microparticles in the ice core from Termination I (climate change from the last glacial maximum to the Holocene) explained the ion balance of the bifurcation diagram in ice sheets well. This study did also find these chemicals in Holocene ice of the Greenland core, under the same acidic conditions observed in Holocene ice of Dome Fuji ice core, and in the glacial periods of ice (less acidic or even alkaline) of the Greenland core, we surely confirmed that the existence of  $\text{CaCO}_3$  in the ice, which were previously suggested. To sum up, these discrepancies in the chemical forms of microparticles found in the Antarctic and Greenland ice cores can be fully explained by a variation in the concentrations of acid and  $\text{Ca}^{2+}$  with climate.

2. This study found that sulfate (coexistence:  $\text{Na}^+$ ,  $\text{SO}_4^{2-}$ ,  $\text{Cl}^-$ ,  $\text{H}^+$ ) exists in liquid phase as microparticles. The phase transition of  $\text{Na}_2\text{SO}_4 \cdot 10\text{H}_2\text{O}$  to liquid sulfate ( $\text{Na}^+$ ,  $\text{SO}_4^{2-}$ ,  $\text{Cl}^-$ ,  $\text{H}^+$ ) and/or liquid sulfate ( $\text{SO}_4^{2-}$ ,  $\text{H}^+$ ) with  $\text{NaCl} \cdot n\text{H}_2\text{O}$  follows the solidus line in the ternary phase diagram of  $\text{Na}_2\text{SO}_4\text{--HCl--H}_2\text{O}$ , which strongly depends on the temperature and concentration of HCl.

3. This study found that microparticles coarsened and had a distinctive spatial distribution in the deep part of ice sheet. In particular, microparticles aggregated on the grain boundaries and air hydrates but not as a connected vein network. This result shows that the preserved ions are dependable proxies of climate histories even in the deepest part of ice sheets and that the resolution depends on the distribution of air hydrates and ice grain size due to microparticles distributed on the air hydrates and grain boundaries at deep regions.

These results help clarify the existence of ions in ice sheets; the evidence of microparticles in ice sheets are particularly important for reconstructing reliable climate histories using ions from the ice cores of Antarctica and Greenland.

# Chapter 1

## Introduction

### 1.1. Background

In general, aerosols are preserved in polar ice cores as water-insoluble (dust) and water-soluble (ions) impurities. These impurities play important role when reconstructing Earth's past climate histories from polar ice cores. For instance, the concentrations of dust in Antarctic ice cores were measured by a laser particle counter in melted ice samples, and the data showed that the dust input to Antarctica was maximum during the glacial maximum (coldest event in a glacial cycle), lower during stadial periods, and minimum in interglacial periods and the Holocene [e.g., [Petit et al., 1999](#)]. These differences play an important role in the climate system for the hydrological cycle [[Lambert et al., 2008](#)], and extent of the continental shelf [[Fujii et al., 2003](#)]. Meanwhile, ions are useful proxies for reconstructing sea ice extent [e.g., [Wolff et al., 2006](#); [Iizuka et al., 2008a](#)], and marine biological activities [e.g., [Wolff et al., 2006](#)]. To focus on the aerosol study, on the other hand, the Intergovernmental Panel on Climate Change ([IPCC, 2007](#)) has suggested that the radiative forcing of sulfate aerosols (as functions of the morphology and concentration of aerosols) since the preindustrial atmosphere produces negative feedback that cools the Earth not only directly but also by the indirect effect of serving as cloud condensation nuclei [e.g., [Penner et al., 2001](#), [Charlson et al., 1987](#)]. The feedback by the aerosols for the past atmosphere provides significant information and may have triggered glacial and interglacial periods. Previous studies used the dust concentration in ice cores to calculate radiative forcing of aerosols between the last glacial maximum (LGM) and Holocene [[Claquin et al., 2003](#); [Chylek and Lohmann, 2008](#)]. However, they excluded water-soluble aerosols due to the difficulty of reconstructing the chemical form of ions in ice as past atmospheric aerosols.

The impurities in ice cores provide significant information on not only Earth's past climate histories but also the past atmospheric aerosols. When reconstructing the Earth's past climate systems and especially the past atmospheric aerosols for radiative forcing of direct and indirect effects from impurities in ice cores, we must confirm the

chemical form of ions and how these impurities behaved during their preservation.

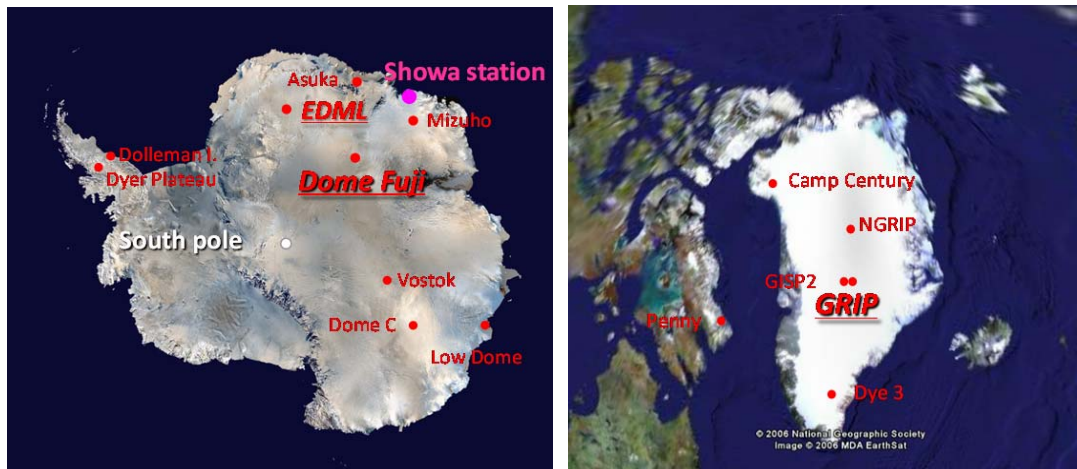


Figure 1.1 Map of ice core sites, Antarctica and Greenland. This study uses the ice cores from Dome Fuji, Antarctica and GRIP, Greenland

## 1.2. Previous studies of the existence of water-soluble impurities in ice cores

The chemical form of dust in ice cores can be determined for each element by using SEM-EDS (Scanning electron microscopy - energy dispersive X-ray spectrometry) [e.g., [Barnes et al., 2002](#); [Baker and Cullen, 2003](#)]. In contrast, ions in ice cores can be measured quantitatively using ion chromatography, which is the fundamental analytical technique in ice core study [e.g., [Legrand et al., 1993](#)]. However, little attention has been paid to the chemical form of ions in ice because measuring the chemical form of ions in ice cores cannot be deduced by ion chromatography. We give a brief overview here of the historical evidence for the chemical form and phase state of species in ice by each anion: sulfate, chloride, nitrate, carbonate, and methanesulfonate.

### *Sulfate ( $SO_4^{2-}$ )*

Sulfate is one of the most abundant ions in both Antarctica and Greenland ice cores, and its origin has been investigated previously. In general, dimethyl sulfide (DMS) is specific to marine biogenic activity, so its concentration in the remote troposphere has been a subject of great interest over the last decade [e.g., [Matrai et al., 2008](#)]. Based on chemical studies of atmospheric aerosol, abundant non sea salt sulfate ( $nssSO_4^{2-}$ ) is formed by the oxidation of DMS and methanesulfonate in the atmosphere [[Hynes et al., 1986](#); [Saigne and Legrand, 1987](#); [Saltelli and Hjorth, 1995](#)]. In addition, sea spray is one of the origins for sea salt aerosols that have a negligible contribution to ice cores [[Fattori et al., 2005](#)]. Volcanic sulfuric acids, another origin of sulfate, is deposited on the surface of ice sheets to produce a relatively higher concentration than the background sulfate concentration ( $nssSO_4^{2-}$ ) in ice [[Gao et al., 2007](#)], but these events are beyond the scope of this study. These sulfates are transported as aerosols over long distances to inland of the ice sheets [[Hara et al., 2004](#)] and deposited on the surface of ice core stations.

Previous studies made efforts to identify and measure the chemicals in ice cores using several techniques. [Wolff et al. \[1984, 1997\]](#) used the electrical conductivity method (ECM) on both polar ice cores and result shows that Holocene ice has a higher electrical conductivity than ice from LGM. The correlation coefficient with various ions showed good results for

sulfate and acids when alternating current (AC)-ECM was used for Dome Fuji ice core, Antarctica [Fujita et al., 2002]. These results suggested that the acids exist as aqueous solutions at the ice grain boundaries. SEM-EDS study found S (sulfur) in ice grain boundaries and suggested that  $\text{SO}_4^{2-}$  exists at ice grain boundaries as a sulfuric acid in the liquid phase; Dolleman [Mulvany et al., 1988] and Dome C [Barnes et al., 2003] ice cores from Antarctica were used. Furthermore, a study using Raman spectroscopy found S–O and N–O symmetric stretching modes and confirmed the existence of sulfuric acid and nitric acid on the triple junction of ice in South Yamato and Nansen ice cores, which were taken from a coastal site in Antarctica [Fukazawa et al., 1998]. Based on this evidence, Rempel et al. [2001, 2002] suggested that pre-melting diffusion by a connecting vein network on ice grain boundaries transports the ions rapidly in ice. More recently, when a shallower depth of the Dome Fuji ice core (185–1351 m) was studied, most  $\text{SO}_4^{2-}$  was found to form salts in the solid ice samples according to micro-Raman spectroscopy [Ohno et al., 2005]. These salts are mostly distributed in ice grains at shallower depths of the ice core; these results suggest that preserved water-soluble impurities are reliable climate proxies and form into microparticles as solid salts. Moreover, the chemical form of the salts altered in each climatic period. In the Dome Fuji ice core, the Holocene and interglacial periods included mainly  $\text{Na}_2\text{SO}_4 \cdot 10\text{H}_2\text{O}$  (mirabilite) and  $\text{MgSO}_4 \cdot 11\text{H}_2\text{O}$  (meridianiite [Genceli et al., 2009]). (Previously, number of hydrates of  $\text{MgSO}_4$  is assumed to be  $12\text{H}_2\text{O}$  for more than a century, but surprisingly Genceli et al. [2007] found number of hydrates of  $\text{MgSO}_4$  as  $11\text{H}_2\text{O}$ . Thus, this study defines as  $11\text{H}_2\text{O}$  of  $\text{MgSO}_4$  instead of  $12\text{H}_2\text{O}$ ). In glacial periods, especially the glacial maximum (the coldest event in the climate changes, hereafter expressed as GM),  $\text{CaSO}_4 \cdot 2\text{H}_2\text{O}$  (gypsum) was mainly present [Ohno et al., 2005]. This difference can be explained by the ion balance, which is measured by ion chromatography [Iizuka et al., 2008b]. In the deep part of the Dome Fuji ice core (1746–2413m), Ohno et al. [2006] reported that the sulfate salt, which has a main peak at  $984\text{ cm}^{-1}$ , becomes the dominant microparticle; the chemical form of the salt may change into another phase in deep regions due to the high pressure of the ice load. As for the phase of the salt, different structures such as heptahydrate or octahydrate of  $\text{Na}_2\text{SO}_4$  were speculated

in deep ice [Oswald et al., 2008]. However, the phase change of hydrates due to several MPa in deep ice compared to the heptahydrate and octahydrate of  $\text{Na}_2\text{SO}_4$  formed due to stable pressure of several GPa is not completely understood.

### *Chloride ( $\text{Cl}^-$ )*

Chloride is a major ion in ice cores. However, the behavior of the chloride ion and its impact in climatic history is not very well understood. Most studies use it as an ion balance for the sodium ion when discussing the sea salt contribution [Röthlisberger et al., 2003; Hara et al., 2004, Fattori et al., 2005]. To the best of our knowledge, the chemical form of water-soluble microparticles in ice cores has not been studied without using melted glacier ice samples, but efforts to measure the ions in melted ice samples have led to the investigation of the existence of chloride as a salt in ice. The  $\text{Cl}^-$  profile is very similar to the  $\text{Na}^+$  profile, suggesting that  $\text{NaCl}$  exists in the LGM ice of Dome Fuji, Antarctica [Iizuka et al., 2004]; there have been discussions on the existence of chloride salts due to the ion balance of  $\text{Na}^+$  and  $\text{Cl}^-$ , Dome C ice core [Röthlisberger et al., 2003] and suggestions that  $\text{NaCl}$  existed at the periods of GMs. In addition, in research on the glacial lake that exists between the ice sheet and bedrock, previous studies have been reported on the inclusion of accretion ice, which is the re-freezing of water from the lake. In the accretion ice of the Vostok ice core, the total ionic content in the shallower depths is variable but remains 5 to 50 times higher than glacier ice [de Angelis et al., 2004]. The most interesting evidence was the finding that  $\text{Cl}^-$  ( $\text{HCl}$ ) may dope in ice and the observation of liquid brine micro-droplets, which was measured by high-resolution synchrotron X-ray micro-fluorescence [de Angelis et al., 2005]. The formation mechanisms are different for glacier and accretion ice, but care must be taken when evaluating deep glacier ice in terms of the doped  $\text{Cl}^-$  ( $\text{HCl}$ ) in ice. Note: the glacier ice is formed by the precipitating of snow on the surface of ice sheets and accretion ice is the re-freezing of water from the lake between bedrock and glacier ice.

### *Nitrate ( $\text{NO}_3^-$ )*

In comparison with other anions, there is relatively little nitrate in ice cores. The origin of nitrate has been previously investigated. In general, as the end product of oxidation for atmospheric nitrogen oxides ( $\text{NO}_x = \text{NO} + \text{NO}_2$ ), nitrate is formed via chemical reaction in the atmosphere [Finlayson-Pitts and Pitts, 2000; von Glasow et al., 2004]. In coastal Antarctica, a previous study [Savarino et al., 2007] reported stable isotope measurements for nitrate ( $\delta^{15}\text{N}$  and  $\delta^{18}\text{O}$ ) in year-round aerosol collections, which suggests the following scenario for nitrate precipitating on ice sheets: (1) sunlight-driven oxidation of  $\text{NO}_x$  ( $\text{NO} + \text{NO}_2$ ) to  $\text{HNO}_3$ ; (2) formation of polar stratospheric clouds (PSCs); and (3) snow reemissions of  $\text{NO}_x$  and  $\text{HNO}_3$  from the surface [see also Iizuka et al., 2006]. When reconstructing past environmental signals, nitrate is very unique in that helps in understanding not only Earth's climate but also that of space. Cosmic rays from supernovas are one source for  $\text{HNO}_3$  formation in the stratosphere due to the oxidation process. Thus, the high concentration of nitrate signals in an ice core can indicate the history of supernovas [Burgess and Zuber, 2000, Dreschhoff, and Laird, 2006]. Therefore, the preserved evidence of nitrate in ice cores is significant, but its behavior (solid, liquid and/or gas) is not so clear in ice.

### *Carbonate ( $\text{CO}_3^{2-}$ )*

Carbonate is one of the most fundamental chemical species on Earth. However, it is one of the least understood species in ice cores. Only evidence is reported which was found on the surface of the Antarctic ice sheet (Talos Dome) [Sala et al., 2008]. On the other hand, there has been some direct and indirect evidence from Greenland GRIP ice core, though not from Antarctica. Based on studies of gas in ice cores, carbonate is sometimes used awkwardly as a species for measuring carbon dioxide in ice. There are two ways to measure carbon dioxide: melting and refreezing ice, and the dry extraction method. The melting-refreezing method shows a carbon dioxide presence that is several tens of parts per million higher than when measured using the dry extraction method [Anklin et al., 1995, 1997]. This evidence suggests that carbonate should exist in Greenland ice core. X-ray diffraction (XRD) by the melting and evaporation method for the Greenland GRIP ice

core suggested  $\text{CaCO}_3$  (calcite) in LGM ice [Svensson et al., 2000]. However, there is uncertainty as to whether the source for the additional carbon dioxide in the ice cores is *in situ* or during measurements. On the other hand, additional carbon dioxide could not appear in the Antarctic ice [Kawamura et al., 2003]. More care needs to be taken when measuring carbonate in ice; thus, information on the distribution of  $\text{CaCO}_3$  in ice cores are needed to discuss the additional carbon dioxide.

### ***Methanesulfonate ( $\text{CH}_3\text{SO}_3^-$ )***

Methanesulfonic acid ( $\text{CH}_3\text{SO}_3\text{H}$ ) is an important compound formed by the oxidation of dimethyl sulfide (DMS), which emitted from marine phytoplankton, in the atmosphere [Hynes et al., 1986; Saigne and Legrand, 1987; Saltelli and Hjorth, 1995]. Therefore,  $\text{CH}_3\text{SO}_3\text{H}$  is specific to marine biogenic activity, so its concentration in the remote troposphere has been the subject of great interest over the last decade. In ice cores,  $\text{CH}_3\text{SO}_3\text{H}$  can be detected through ion chromatography as  $\text{CH}_3\text{SO}_3^-$  by melting ice samples. Its anion has become an important tool for reconstructing several activities related to climate change: marine productivity [Legrand et al., 1991, 1992], sea ice extent [Curran et al., 2003], and major El Niño events [Legrand and Feniet-Saigne, 1991]. However, it is a minor ion in inland ice cores [Fattori et al., 2005].

In the present time period, especially in firn layers, ice core  $\text{CH}_3\text{SO}_3^-$  appears to derive from post-depositional relocation; this process occurs while the acid is in the gas and/or liquid phase [Mulvaney et al., 1992; Jaffrezo et al., 1994; Pasteur and Mulvaney, 1999; Pasteur and Mulvaney, 2000; Smith et al., 2004; McMorrow et al., 2004; Ruth et al., 2005]. Mulvaney et al. [1992] implied that  $\text{CH}_3\text{SO}_3^-$  may have formed as sodium methanesulfonate and/or magnesium methanesulfonate in the firn of the Dolleman ice core. Moreover, the  $\text{CH}_3\text{SO}_3^-$  concentration decreases with depth, which is similar to the observed behavior of nitrate and chloride ions. This trend suggests that  $\text{CH}_3\text{SO}_3^-$  may evaporate from the firn [Wagon et al., 2000; Delmas et al., 2003].

In glacial time periods, on the other hand,  $\text{CH}_3\text{SO}_3^-$  may form salts that probably originate during the fixation of  $\text{CH}_3\text{SO}_3^-$  on alkaline particles of marine or continental origin [Delmas et al., 2003]. In non-melting ice

samples, a recent study using Raman spectroscopy has found and provided new information on the chemical forms of certain water-soluble salts contained in the microparticles of ice cores; it suggested that methanesulfonate may exist as a salt in glacial periods [Ohno et al., 2005, 2006; Barletta et al., 2009]. However, the chemical form of the methanesulfonate salt is still not understood.

When reconstructing past climate histories from reliable proxies, considering the eutectic temperature of each salt is significant for understanding the phase state of ions. The temperature of the ice sheets varies from the surface to the bedrock, and the temperature of the deepest ice near the bedrock is at the pressure melting point of ice. The temperature profile of the ice core gives us significant information for describing the phase states of ions (liquid and/or solid), and some salts as solid phase with relatively high eutectic temperatures may melt in ice [Hondoh et al., 2002, ] (Figure 1.2). For pre-melting liquids separated at ice grain boundaries (especially the triple junction of the ice) pre-melting diffusion of ions by the connecting vein network may transport rapidly in ice [Rempel et al., 2001, 2002]. In the deeper part of the Dome Fuji ice core, pre-melting diffusion over several distance lengths may have occurred through the connecting vein network due to higher temperature conditions in deep parts of the ice core.

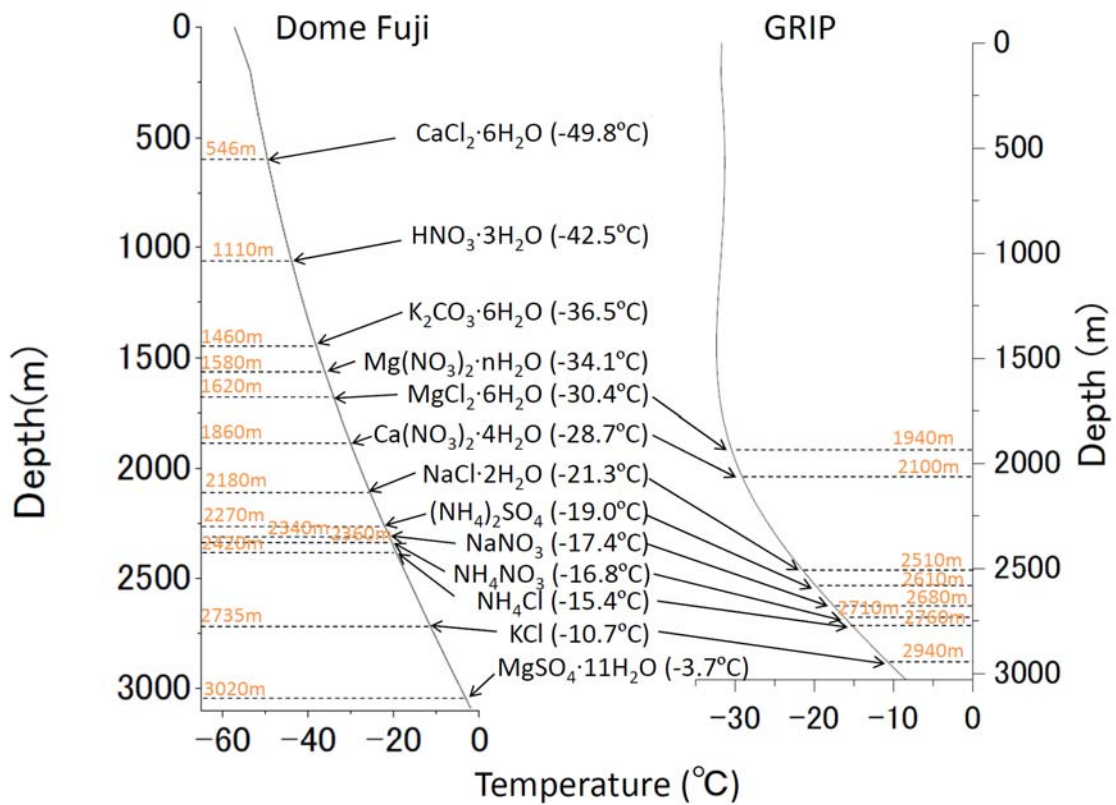


Figure 1.2. The depth of melting salts in the respective ice cores. Ice core temperature of Dome Fuji ice core, Antarctica (Calculated by [Hondoh et al., 2002](#)), GRIP ice core, Greenland [[Johnsen et al., 1995](#)] and eutectic temperature of each salts (unconsidered pressure melting  $\Delta T$ ) are shown.

### 1.3. Aim of this study

This study clarifies that the chemical form and distribution of the water-soluble microparticles as functions of climate, ice core from north and south hemisphere, and the depth of Dome Fuji ice core. To clarify the variability of chemical form of microparticles as functions of climate, we focused on the climate change during the Termination I (from LGM to Holocene) from Dome Fuji ice (Antarctica). To clarify the difference as a function of north and south hemisphere, this study measured the microparticles both Antarctica (Dome Fuji) and Greenland (GRIP) ice cores. Especially, in order to gain insight into the redistribution mechanism of ions, this study focused on the deep part of Dome Fuji ice core in terms of the phase equilibrium state for salts. The issue is important when to reconstruct the reliable past climate records.

Chapter 1 shows the introduction of this thesis such as background, previous studies and aim and composition of this thesis. Chapter 2, methods are shown. This study used based on methods summarized in the chapter. Chapter 3 to 7 shows results and discussions. After these chapters, conclusions are summarized in the chapter 8 and acknowledgements and references are written after chapter 8. The chapters from 3 to 7 are separated for issues as follows.

Chapter 3 shows that difference of the chemical form of the water-soluble microparticles drastically changes during Termination I. This chapter clarifies that the chemical form of the microparticles in respective climate periods is different due to the concentration of acids and  $\text{Ca}^{2+}$  measuring the water-soluble microparticles by Raman spectroscopy and ion balance by Ion Chromatography during Termination I.

Chapter 4 shows that the  $(\text{CH}_3\text{SO}_3)_2\text{Mg} \cdot n\text{H}_2\text{O}$  found in the LGM ice of Dome Fuji ice core, supporting the evidence of lower acidity. During the LGM,  $(\text{CH}_3\text{SO}_3)_2\text{Mg} \cdot n\text{H}_2\text{O}$  could have formed in the atmosphere and/or along the edge of sea ice and later been transported as an aerosol to the surface of ice sheet, where it would have a chance to survive due to the low acidity of the ice.

Chapter 5 shows that the finding of sulfate salts as liquid microparticles in deep ice. This chapter clarified the issue by measuring the chemical form and the phase states of microparticles using low frequency of micro-Raman spectroscopy and DSC to construct the phase equilibrium states of ternary phase to identify the chemical form. This study concluded that the liquid sulfate should contain  $\text{Na}^+$ ,  $\text{SO}_4^{2-}$ ,  $\text{Cl}^-$ , and  $\text{H}^+$  as a disconnected vein network of ice (form microparticle). This evidence is particularly relevant to research reconstructing the oldest climate histories from deep ice cores.

Chapter 6 shows that the distribution of microparticles focused on the deep part of Dome Fuji ice core. This study clarified that in deep ice, microparticles (including liquids and solids) are preserved at the grain boundaries due to their tendency to aggregate (and their larger size). In the deepest part of the ice, almost 30% of microparticles are located on the air hydrates. This chapter clarifies the redistribution of microparticles in the deep part of Dome Fuji ice core and these findings are significant with respect to the resolution of reliable proxies in ice core for the reconstruction of Earth's environmental history.

Chapter 7 shows that the microparticles surely exist as microparticles in the GRIP ice core, Greenland. The issue of this chapter is that the clarification of the existence of water-soluble microparticles as functions of climate and implied the importance of this finding.

Chapter 8 summarizes the main achievements of this research: (1) identifying the chemical forms of water-soluble microparticles in the Antarctic and Greenland ice cores, and describing their variation with climate; (2) analyzing the nature and behavior of water-soluble microparticles as a function of depth; (3) miscellaneous minor results; and (4) future prospects.



# Chapter 2

## Methods

### 2.1 Ice preparation

#### 2.1.1 Antarctic ice

##### *Termination I from Dome Fuji ice core*

The Dome Fuji station placed at the highest altitude in the East Dronning Maud Land Plateau in central Antarctica, 3810m above sea level [[Dome-F Deep Coring Group, 1998](#)]. The first project of Dome Fuji ice core was drilled at the station and the length of the core is 2503m. The core was transported to Institute of Low Temperature Science, Hokkaido Japan and stored in cold room at  $-50^{\circ}\text{C}$ . We used six samples from the Termination I; the last glacial maximum (LGM) to Holocene transition, dated about 20 kyr BP to 10 kyr BP (Before Present). The six core samples are 10.3 (340.38 to 340.43), 11.8 (382.86 to 382.91), 13.2 (414.36 to 414.41), 15.6 (463.85 to 463.90), 18.5 (502.35 to 502.40), 24.5 (576.50 to 576.55) kyrBP (Before Present), respectively [[Watanabe et al., 2003](#)]. These cores were cut with a band saw into 3 sections for 3 measurements which are the number concentration of microparticles, the chemical form of microparticles, and ion concentration. The core sections for measurement of number concentration and chemical form were cut into  $50\times 10\times 2\text{mm}^3$ , respectively. The core section for ion concentration was cut into  $50\times 10\times 10\text{mm}^3$ . These ice sections are used for [section 2.3](#), and for [chapter 3](#), and [4](#).

##### *Deeper part of Dome Fuji ice core*

The second Dome Fuji ice core was excavated from 2004-2006 on the summit of East Dronning Maud Land Plateau (3810 m asl), same part as the first Dome Fuji ice core project. The second project of Dome Fuji ice core was drilled at the station and the length of the core is 3035m. The core was transported to Institute of Low Temperature Science, Hokkaido Japan and stored in cold room at  $-50^{\circ}\text{C}$ . In this study, we analyze  $100\times 50\times 5\text{mm}^3$  sections of the Dome Fuji ice core taken from depths of 2491.0, 2510.5, 2606.5, 2642.5, 2702.5, 2762.5, 2798.5, 2822.5, 2882.5, 2906.5, 2996.5, and 3019.5m. To measure the microparticles, we sliced the samples with a band saw to a thickness of several millimeters and smoothed the resulting section with a microtome. Exactly same

depth of ice samples are cut for two ice section, and one is used for measuring the chemical form by micro Raman spectroscopy [chapter 5], and the other is used for measuring diameter, number concentration and spatial distribution [chapter 6].

## 2.1.2 Greenland ice

The GRIP ice core was recovered at the highest point in central Greenland, 3200 m above sea level (72.6°N, 38.5°W). The core from 783 m to 2282 m was drilled in 1991, and the lower section below 2280 to bedrock was drilled in 1992. More information on the geographical environment of the station is available in the [GRIP members \[1993\]](#) report. After drilling, the core was stored in a cold room at -26 °C, in the University of Copenhagen, Denmark. Five GRIP ice core segments, each 300-400 mm in length, arrived in Japan. The ice core segments were stored in a cold room at -50 °C, after arrival in Japan. The five ice segments are dated from 6.9 kyrBP (1200.35 to 1200.65 m), 9.8 kyrBP (1501.66 to 1502.05 m), 13.5 kyrBP (1700.61 to 1700.91 m), 30.0 kyrBP (2099.90 to 2100.20 m), and 43.1 kyrBP (2300.65 to 2301.05 m) [[Johnsen et al., 1997](#)]. The 6.9 kyrBP and 9.8 kyrBP sections belong to the Holocene. The 30.0 kyrBP and 43.1 kyrBP sections belong to the last glacial period. The 13.5 kyrBP section belongs to Termination I. The 40mm ice samples were sliced from the top of the 6.9kyrBP (1200.35 to 1200.39m), 9.8kyrBP (1501.66 to 1501.70m), and 13.5kyrBP (1700.61 to 1700.65m) ice core sections, and 50mm ice samples were sliced from the top of the 30.0kyrBP (2099.90 to 2099.95m), and 43.1kyrBP (2300.65 to 2300.70m) ice core sections. These sub-cores were cut into three slices of exactly the same depth for analysis by optical microscopy, micro-Raman spectroscopy, and ion chromatography [chapter 7].

## 2.2 Optical characterization

To measure the number and diameters of microparticles, the ice was sliced with a microtome to a thickness of several millimeters and observed with an optical microscope (Olympus BH2 - UMA, with objective lens Olympus ULWD Neo SPlan 50, N.A.:0.55, 50×) in a cold clean room at -15°C. According to the Becke test, the density contrast between microparticles and the surrounding ice is strong enough to distinguish by optical microscopy. We cannot distinguish between dust (insoluble) and salt (water soluble) microparticles, however, so both types are counted. Microparticles with a

diameter greater than 1.0  $\mu\text{m}$  can be measured reliably by this method, but diameters less than 2.0  $\mu\text{m}$  have a large margin of error. All microparticles in the field of view ( $0.14 \times 0.18 \times \text{thickness}$  in  $\text{mm}^3$ ) of the optical microscope were counted and measured, and we randomly picked 100 of sights to calculate the average number per  $\text{mm}^3$  and standard deviation. The density unit was calculated as  $\text{count/mL}$  from  $\text{count/mm}^3$ . In additional measurements to compare the different spatial distribution of microparticles in ice, the microparticles were measured in the field of the microscope ( $0.14 \times 0.18 \times \text{thickness}$   $\text{mm}^3$ ) and 100 views were measured to construct a view of  $1.4 \times 1.8 \times \text{thickness}$  in  $\text{mm}^3$ . To measure the spatial distribution, we selected one view ( $1.4 \times 1.8 \times \text{thickness}$   $\text{mm}^3$ ) which contains a grain boundary and air hydrate, but does not include the plate like inclusions, because we cannot see the microparticles in and bottom of plate like inclusions. Especially in deeper part of Dome Fuji ice core, the thickness of measuring sight has to be several millimeters thick, because we focused on the distribution of microparticles along not only just grain boundary and in ice grain but also the distribution of microparticles related to the air hydrates in ice. In these observations, we have not accounted for a possible influence of seasonal variability on the differences between samples taken from different time periods.

## 2.3 Micro-Raman spectroscopy

This section reports our procedure to determine the chemical form of microparticles in polar ice through micro Raman spectroscopy. Following a brief review of the technique, we will describe our methodology in detail and the importance of settings such as slit width and laser power to how we measure the microparticles. We also provide reference Raman spectra for the most common salts.

### 2.3.1 Setup of Cryostat

To measure the chemical forms of the microparticles, we use a micro Raman spectroscope and a cryostat (Fig.2.1). Both are set on an x-y-z translation stage. A thermocouple is connected to the cryostat with metal to stabilize and measure the interior temperature. Copper is used for the connection because its thermal conductivity ( $4.01 \text{ W cm}^{-1} \text{ K}^{-1}$ ) is greater than that of ice ( $0.02 \text{ W cm}^{-1} \text{ K}^{-1}$ ) [CRC Handbook, 2001]; the metal rapidly equilibrates to the temperature inside the cryostat. In addition to the thermocouple, we place a platinum resistance temperature sensor ( $100\Omega$ ) by the sample to measure its temperature directly.

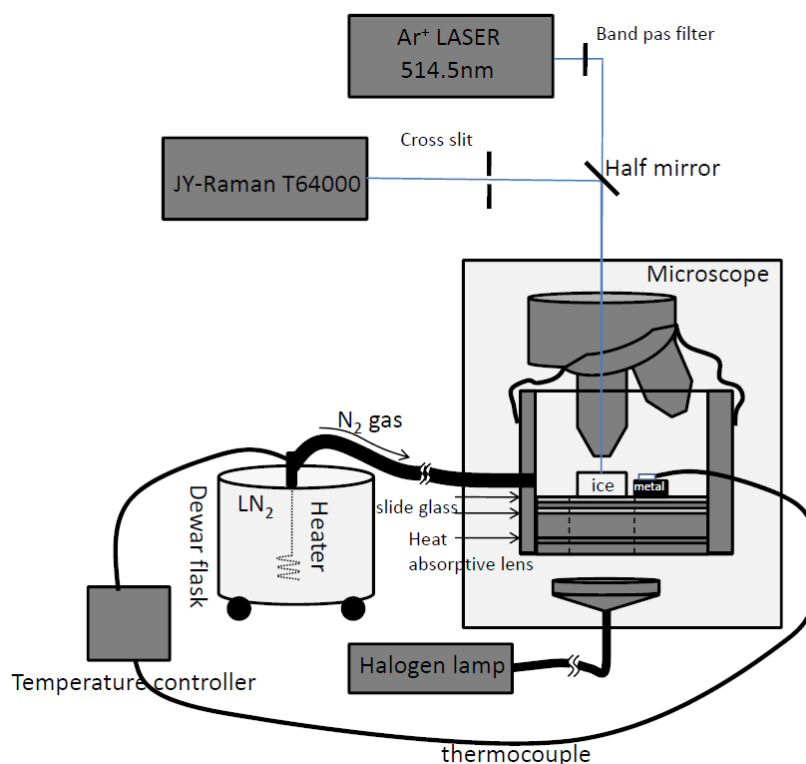


Figure 2.1. Schematic of the cryostat system. The temperature is controlled by  $N_2$  gas, evaporated by a heater inside a Dewar flask containing liquid  $N_2$ . The heater is controlled by and connected to a thermocouple inside the cryostat. The cryostat container is made of chloroethene, and a Styrofoam setting is inside the container. Heat-absorptive lens and slide glasses are set inside the Styrofoam between the ice sample and the halogen light source, to prevent the latter from warming the sample.

To cool the cryostat, we used an  $N_2$  gas flow from liquid nitrogen heated by a sheath coil inside the Dewar. The sheath heater coil emits 400 W and has a resistance of  $25.0 \Omega$ . The coil is connected to a PID (proportional–integral–derivative) temperature controller, which monitors the inside of the cryostat via the thermocouple. [Figure 2.2](#) shows the temperature of the cryostat as it is cooled from room temperature to  $-30.0^\circ\text{C}$  using the PID temperature controller. After a cool-down phase, the cryostat can be maintained at constant temperature for a long period with no significant gradient in the ice sample. During the cool-down phase, however, microparticles may move around inside the ice due to a temperature gradient. Laser light cannot irradiate the microparticles during this phase. To stabilize the temperature at  $-30.0^\circ\text{C} \pm 0.2^\circ\text{C}$  took about 30 minutes for our cryostat.

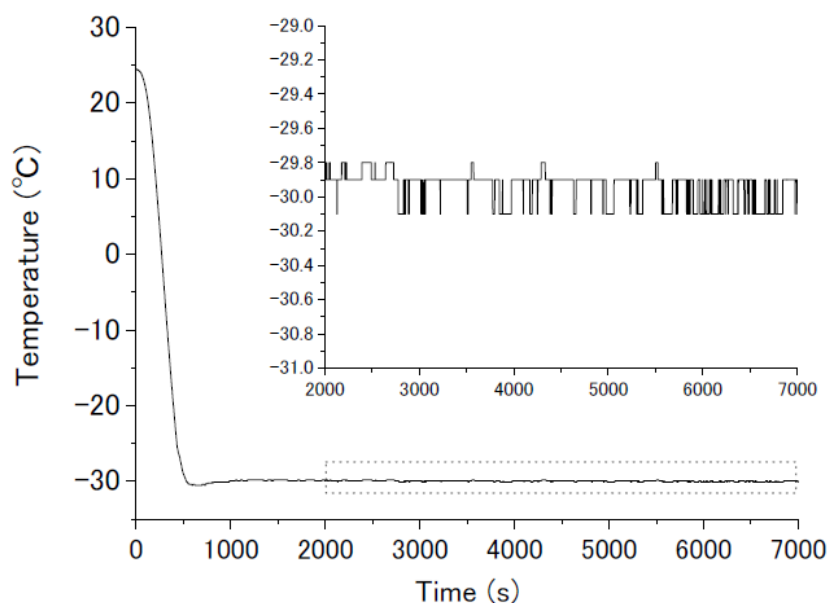


Figure 2.2. Cooling the cryostat. The temperature is reduced from room temperature to a stable value of  $-30.0^{\circ}\text{C}$ . The controller uses the auto PID method.

### 2.3.2 Raman spectroscopy

We employed an Ar ion laser with a wavelength of 514.5 nm (NEC GLG3260) and a maximum beam power of 1000mW at the source. A band pass filter (Edmund Optics 47492-J) is placed just after the laser source. The filter blocks 99.995% of wavelengths in the ranges 434-509nm and 520-670nm (its optical density in this range is better than 5.0) and blocks only 10% of the central wavelength. We verified that the attenuation of the laser was independent of its power at the source by measuring the laser power at the objective lens for several different intensity settings (Figure 2.3). The laser power at the objective lens is always about 10% of the source power.

To detect the Raman spectra, it is necessary to focus the laser on a microparticle through a high-magnification objective lens. However, the focal lengths of such lenses are generally small. In the cryostat, the ice sample has to be kept at a stable temperature so that microparticles and the ice section itself do not move during the measurement. Therefore, managing the heat flux from the objective lens to the ice sample is a significant problem. To avoid creating a temperature gradient between the objective lens and the sample, we chose an objective lens with a super-long working distance (6.0mm focal length) and a numerical aperture (N.A.) of 0.75 (Mitutoyo, M Plan Apo 100 $\times$ ). Please note that the temperature increases of ice during emitting the laser inside of the ice are not confirmed but some chemical form could be.

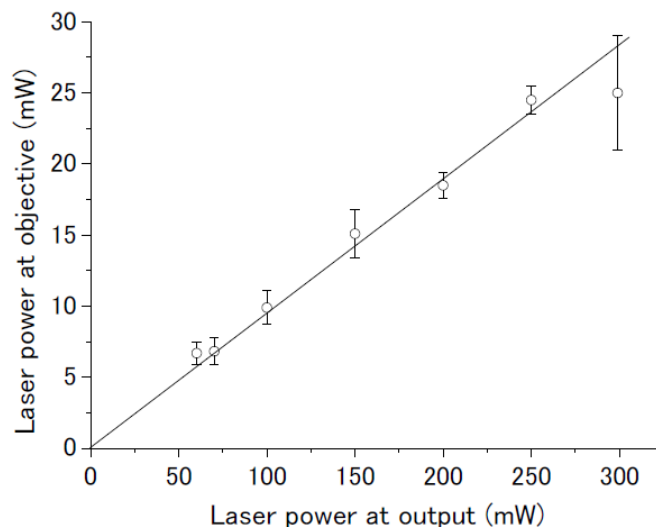


Figure 2.3. Laser power measurements at the source output and objective.

The detectors are a triple monochromator (Jobin-Yvon, T64000) and a CCD detector (Jobin-Yvon, Spectraview-2D, 1024×256 pixels, cooled by liquid nitrogen) with good quantum efficiency from 500 to 900 nm. Using a grating with 1800 lines/mm and an entrance slit of 100 $\mu$ m, the spectral resolution is 0.6 $\text{cm}^{-1}$ . The absolute frequency of the monochromator was calibrated using a neon emission line and silicon wafers.

The cross slit is the one of the most important components of Raman spectroscopy. It allows the researcher to change the size of the laser beam, from several micrometers down to 1 micrometer. [Figure 2.4](#) shows how the shape of the Raman peak from a silicon wafer varies with the beam size. The smallest cross slit results in a low-intensity peak compared to the large cross slits, but all settings greater than 5.0  $\mu$ m yield nearly the same intensity. [Figure 2.5](#) shows the intensity of the peak as a function of laser power at the source for silicon wafers. The relationship is monotonic but nonlinear. These variations in peak intensity will be significant when we discuss the measurement of micron-sized particles in ice.

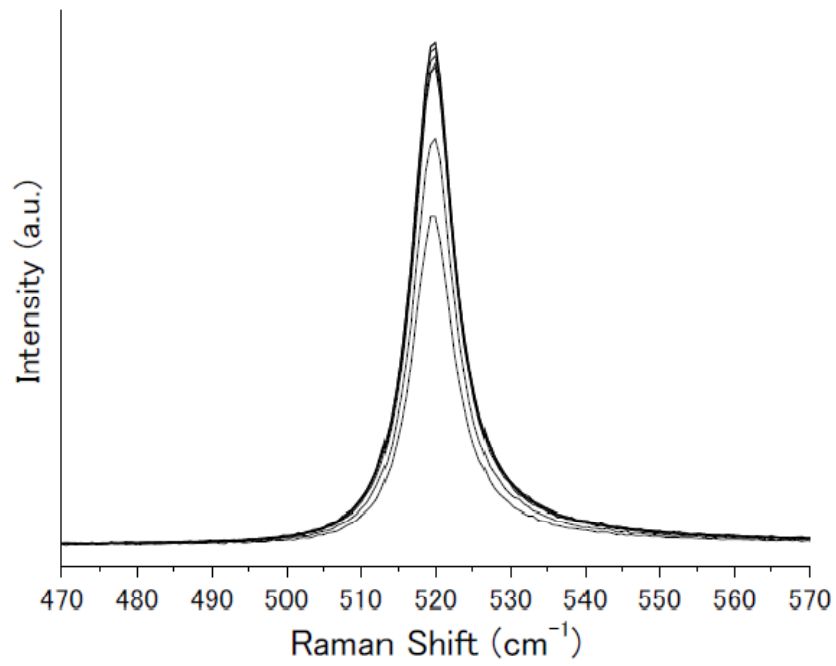


Figure 2.4. The Raman peak intensity of a silicon wafer (1.1.1) depends on the cross slit width, for 1.0 - 5.0  $\mu\text{m}$  slits.

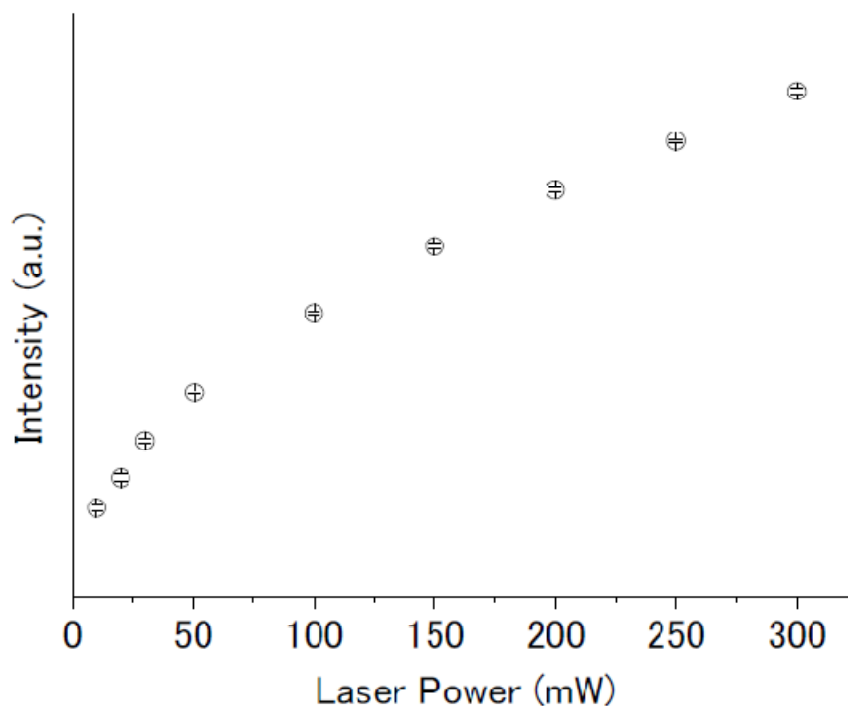


Figure 2.5. The Raman peak intensity of a silicon wafer increases with laser power up to 200 mW.

### 2.3.3 Reference samples

To identify the chemical forms of microparticles in ice cores, we need to know the spectra of the chemicals in advance. A database of reference spectra for various minerals, both water-soluble and insoluble, is available at the RRUFF website (<http://rruff.info/>) among others. However, since we wish to compare quantitative measurements, it is necessary to obtain reference spectra using our own equipment. We measured reference spectra for the following specimens:  $\text{Na}_2\text{SO}_4$  (thenardite),  $\text{Na}_2\text{SO}_4 \cdot 10\text{H}_2\text{O}$  (mirabilite),  $\text{Na}_2\text{SO}_4 \cdot 7\text{H}_2\text{O}$ ,  $\text{NaHSO}_4$ ,  $\text{MgSO}_4 \cdot 7\text{H}_2\text{O}$  (epsomite),  $\text{MgSO}_4 \cdot 11\text{H}_2\text{O}$  (meridianiite),  $\text{CaSO}_4 \cdot 0.5\text{H}_2\text{O}$ ,  $\text{CaSO}_4 \cdot 2\text{H}_2\text{O}$  (gypsum),  $(\text{NH}_4)_2\text{SO}_4$  (mascagnite),  $\text{NaCl} \cdot 2\text{H}_2\text{O}$  (hydrohalite),  $\text{MgCl}_2 \cdot 12\text{H}_2\text{O}$ ,  $\text{NaNO}_3$ ,  $\text{Mg}(\text{NO}_3)_2 \cdot 6\text{H}_2\text{O}$ ,  $\text{Ca}(\text{NO}_3)_2 \cdot 4\text{H}_2\text{O}$ ,  $\text{Na}_2\text{CO}_3$ ,  $\text{Na}_2\text{CO}_3 \cdot 10\text{H}_2\text{O}$ ,  $\text{CaCO}_3$ ,  $\text{CH}_3\text{SO}_3\text{Na}$ ,  $(\text{CH}_3\text{SO}_3)_2\text{Mg}$ ,  $\text{CH}_3\text{SO}_3\text{K}$ , and  $(\text{CH}_3\text{SO}_3)_2\text{Ca}$ . It is necessary to measure these salts below their eutectic temperatures, which can be determined by constructing a phase diagram [e.g. [Uzdowski and Diezel, 1998](#)]. The reference Raman spectra of groups  $\text{SO}_4^{2-}$ ,  $\text{Cl}^-$ ,  $\text{NO}_3^-$ ,  $\text{CO}_3^{2-}$ , and  $\text{CH}_3\text{SO}_3^-$  are shown in [Figures 2.6, 2.7, 2.8, 2.9 and 2.10](#) respectively.

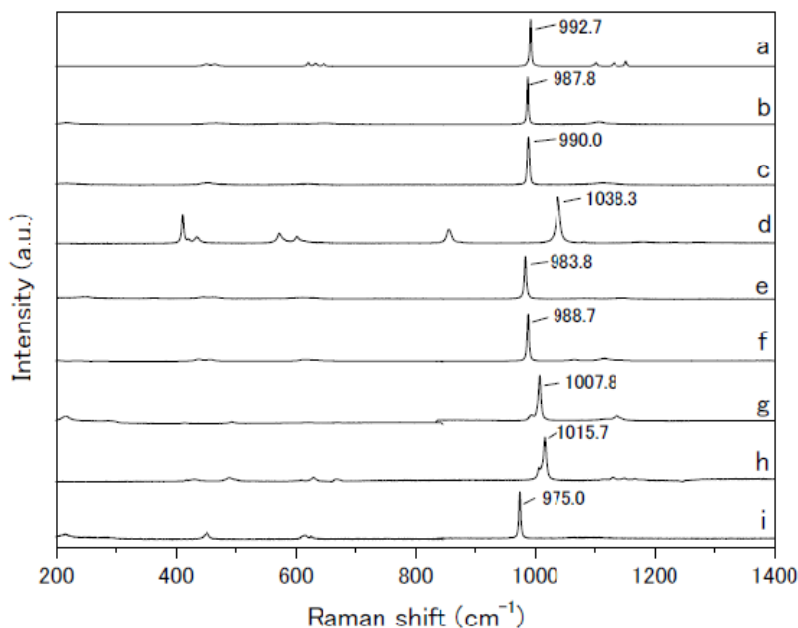


Figure 2.6. Reference Raman spectra of  $\text{SO}_4^{2-}$  salts. a.  $\text{Na}_2\text{SO}_4$ ; b.  $\text{Na}_2\text{SO}_4 \cdot 7\text{H}_2\text{O}$ ; c.  $\text{Na}_2\text{SO}_4 \cdot 10\text{H}_2\text{O}$ ; d.  $\text{NaHSO}_4$ ; e.  $\text{MgSO}_4 \cdot 7\text{H}_2\text{O}$ ; f.  $\text{MgSO}_4 \cdot 11\text{H}_2\text{O}$ ; g.  $\text{CaSO}_4 \cdot 2\text{H}_2\text{O}$ ; h.  $\text{CaSO}_4 \cdot 0.5\text{H}_2\text{O}$ ; i.  $(\text{NH}_4)_2\text{SO}_4$ .

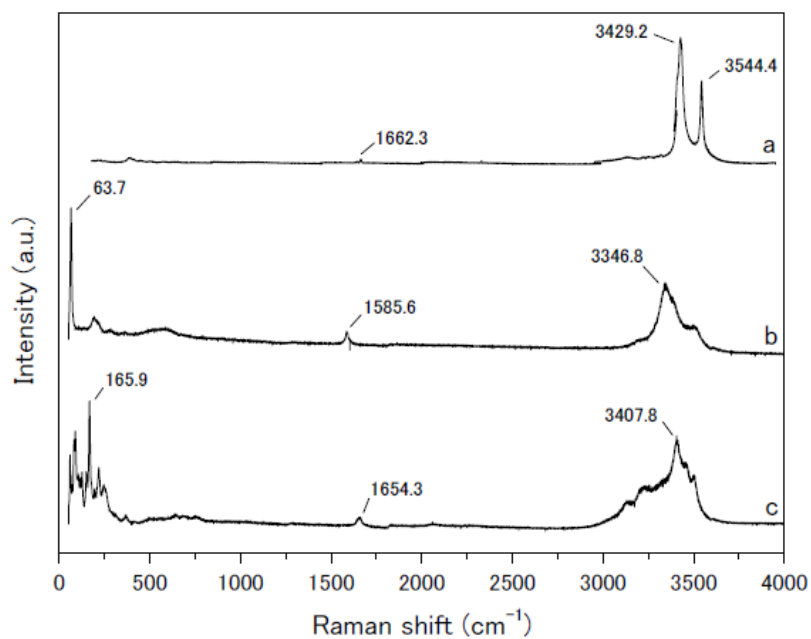


Figure 2.7. Reference Raman spectra of  $\text{Cl}^-$  salts. a.  $\text{NaCl} \cdot 2\text{H}_2\text{O}$ ; b.  $\text{MgCl}_2 \cdot 6\text{H}_2\text{O}$ ; c.  $\text{MgCl}_2 \cdot 12\text{H}_2\text{O}$ .

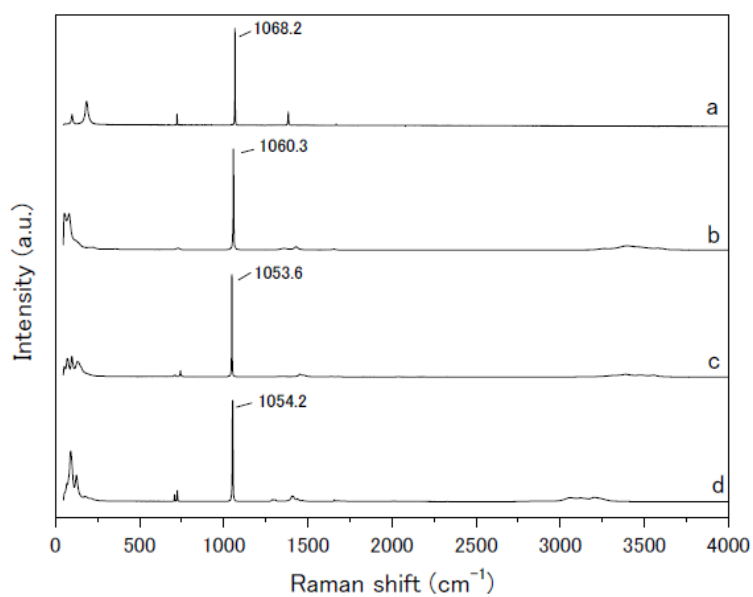


Figure 2.8. Reference Raman spectra of  $\text{NO}_3^-$  salts. a.  $\text{NaNO}_3$ ; b.  $\text{Mg}(\text{NO}_3)_2 \cdot 6\text{H}_2\text{O}$ ; c.  $\text{Ca}(\text{NO}_3)_2 \cdot 4\text{H}_2\text{O}$ ; d.  $\text{NH}_4\text{NO}_3$ .

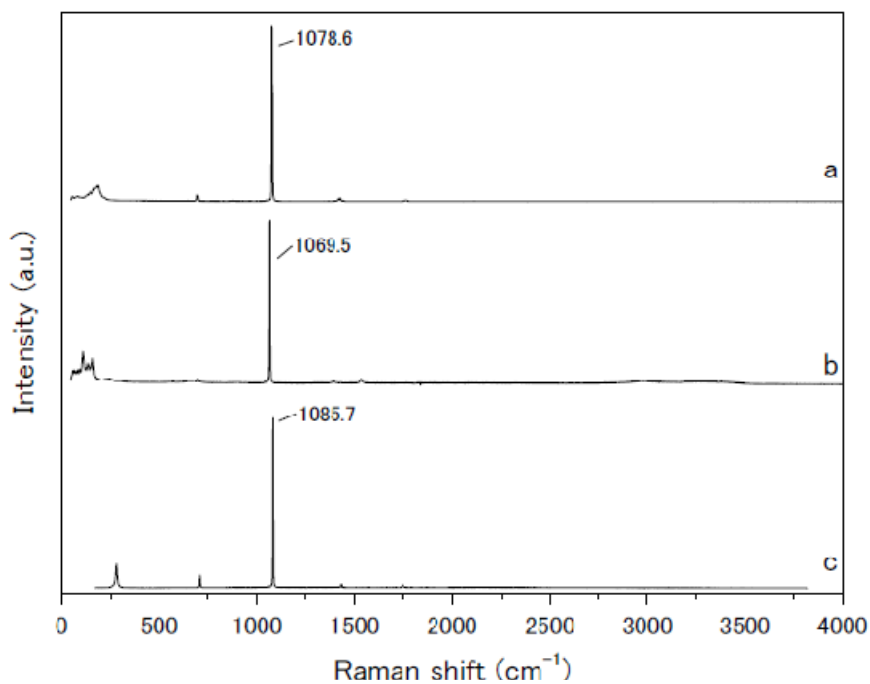


Figure 2.9. Reference Raman spectra of  $\text{CO}_3^{2-}$  salts. a.  $\text{NaCO}_3$ ; b.  $\text{NaCO}_3 \cdot 10\text{H}_2\text{O}$ ; c.  $\text{CaCO}_3$ .

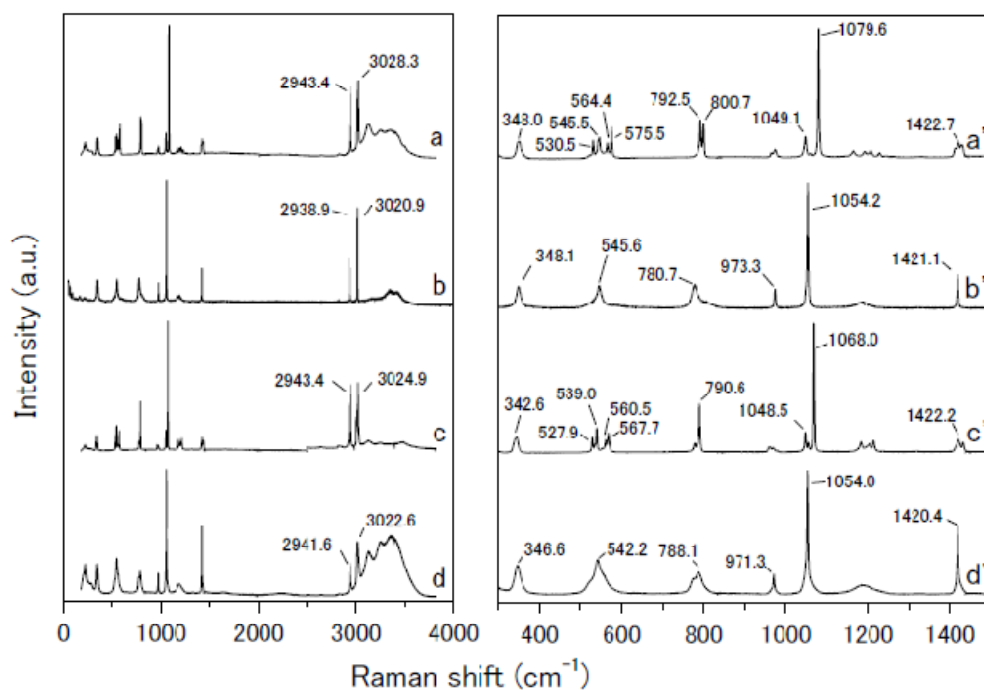


Figure 2.10. Reference Raman spectra of  $\text{CH}_3\text{SO}_3^-$  salts. a.  $\text{CH}_3\text{SO}_3\text{Na} \cdot n\text{H}_2\text{O}$ ; b.  $(\text{CH}_3\text{SO}_3)_2\text{Mg} \cdot n\text{H}_2\text{O}$ ; c.  $(\text{CH}_3\text{SO}_3)_2\text{Ca} \cdot n\text{H}_2\text{O}$ .

### 2.3.4 Ice preparation

Ice sections are cut from the Termination I, Dome Fuji ice core [Section 2.1.1] and planed by microtome to a thickness of several millimeters. To fit inside the cryostat, we usually cut the planed samples down to  $50 \times 30 \times \text{thickness}$  mm<sup>3</sup>. The thickness depends on the grain size of the ice section. If the ice crystals are smaller than the sample thickness, the laser may reflect at a grain boundary and prevent us from clearly seeing the microparticles. Ideally, for the microparticles to be clearly visible, the sample thickness should be approximately equal to the ice grain size.

Several minutes after the sample is placed in the cryostat, the temperature has stabilized. The ice is backlit by a halogen lamp, and we use a low-magnification lens (focal length 33.5mm and N.A. 0.28; Mitsutoyo M Plan Apo 10 $\times$ ) to search for microparticles. When we find one, we focus the laser on the microparticle with the 100 $\times$  lens and record its Raman spectrum.

### 2.3.5 Measuring microparticles in polar ice

To measure microparticles of various diameters in polar ice by micro Raman spectroscopy, it is necessary to take several parameters into account. The two most important considerations are the width of the cross slit and the power of the laser.

We measured microparticles approximately 3.0  $\mu\text{m}$  in diameter to show how the Raman signal changes with cross slit width and laser power. Figure 2.11 shows the dependence of peak intensity on slit width for single microparticles in Dome Fuji ice with the laser power set to 100mW and a total measuring time of 120 seconds. The Raman intensity of the microparticles alone, obtained by subtracting the spectrum of the ice, increases with slit width up to 3.0  $\mu\text{m}$  then decreases gradually for greater widths. Figure 2.12 compares the spectra of mirabilite microparticles in ice with the cross slit set to 1.0  $\mu\text{m}$ , for five different values of the laser power. The intensities obtained rise with the laser power, but beyond 200mW do not change significantly (data in this range are omitted from the figure). The reason for this behavior may be that at 200 mW, the entire microparticle (top to bottom) is influenced by the laser. Taken together, these results suggest that the cross slit should be the same size as the microparticles and the laser power should be less than 200mW. Thus, in this paper, we employed these setting speculated on maximum size of microparticles at 3.0 $\mu\text{m}$ .

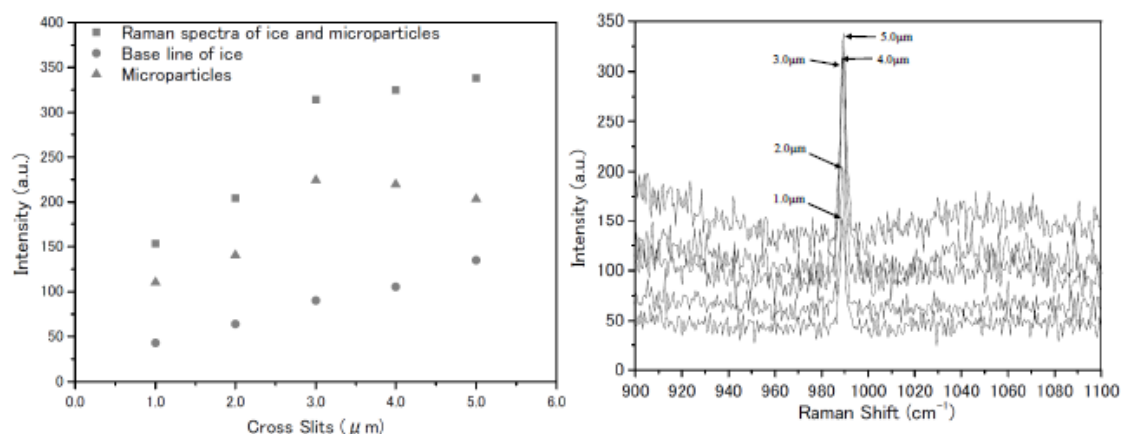


Figure 2.11. The plotted intensities are Raman peaks from the S-O symmetric stretching mode of a mirabilite microparticle found in the Dome Fuji ice core, for several cross slit widths. The left-hand plot (a) shows the peak intensities as a function of slit width. The series “Raman spectra of ice and microparticles” is derived from the raw spectral data. “Base line of ice” is an average of 60 spectra taken from points on the ice without any microparticles. This spectrum is subtracted from the raw spectra of the S-O symmetric stretching mode to obtain the “Microparticle” spectrum. The right-hand plot (b) shows the raw data of each spectra.

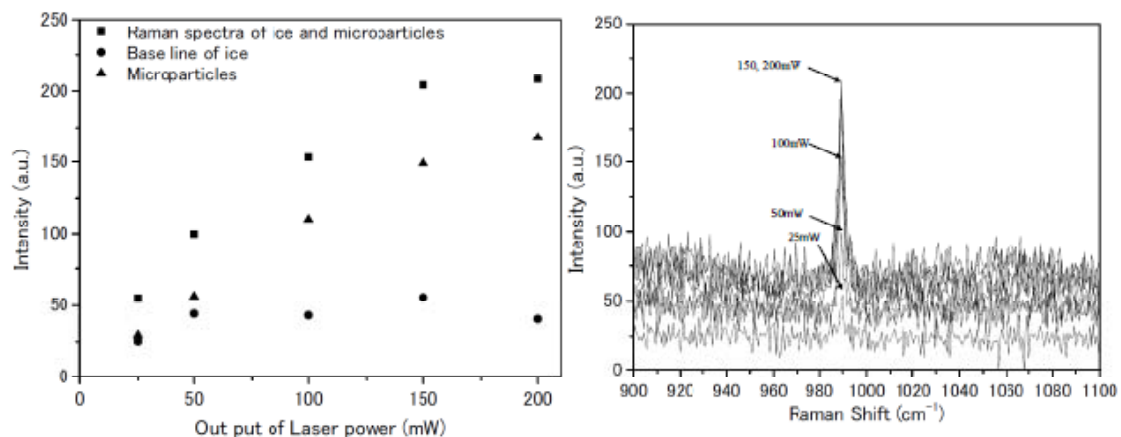


Figure 2.12. As Figure 2.11, expect that the intensities of the S-O symmetric stretching mode are measured for several different laser powers.

Here we show the example of the result from Termination I, Dome Fuji ice core. Figure 2.13 shows the result where microparticles were analyzed using a laser power of 200mW. We found  $\text{CaSO}_4 \cdot 2\text{H}_2\text{O}$  (gypsum),  $\text{Na}_2\text{SO}_4 \cdot 10\text{H}_2\text{O}$  (mirabilite),  $\text{MgSO}_4 \cdot 11\text{H}_2\text{O}$  (meridianiite), nitrate with sulfate,  $(\text{CH}_3\text{SO}_3)_2\text{Mg} \cdot n\text{H}_2\text{O}$  (chapter 6), and another chemical form which we have not yet identified. However, there are still some difficulties to be resolved with this method of analyzing microparticles in polar ice. For instance, some microparticles either give Raman signals too weak to be detected or are

composed of Raman-inactive materials. These are classified as “no Raman signal”. A few microparticles changed shape when we compare their images before and after Raman spectroscopy, so are classified as “broken particles”. These particles probably melted and/or broke apart during measurement due to the high laser power. Thus, we are still unable to measure the chemical form of all microparticles in polar ice, but we insist that the method is very successful and reliable for certain chemical forms. It is especially useful for measuring sulfates ( $\text{CaSO}_4 \cdot 2\text{H}_2\text{O}$ ,  $\text{Na}_2\text{SO}_4 \cdot 10\text{H}_2\text{O}$ ,  $\text{MgSO}_4 \cdot 11\text{H}_2\text{O}$ ), which are relatively abundant compared to other types of microparticles in polar ice.

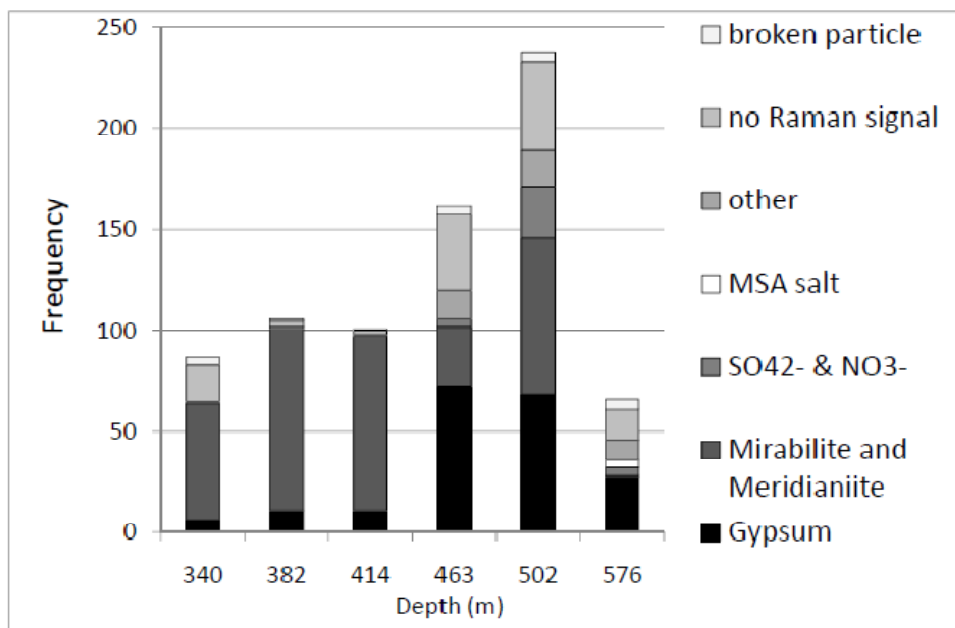


Figure 2.13. The distribution of microparticle chemical forms found in ice samples taken from Termination I of the Dome Fuji ice core. 340m: Holocene, 382 - 502m: Termination I, 576m: Last Glacial Maximum (the coldest event in the last glacial cycle). The numbers of microparticles measured at each depth are 87, 106, 101, 161, 237, and 66 respectively (a total of 758 particles). The numbers of microparticles in the “no Raman signal” category are 18, 3, 2, 37, 44, and 15 respectively. The numbers of “broken particles” are 4, 1, 1, 4, 4, and 5 respectively. Sulfate salts and “no Raman signal” will be discussed in more detail in [chapter 3](#).

An additional factor is the ratio between the width of the slit and the diameter of the microparticle. [Figure 2.14](#) shows the relation of intensity of microparticles and diameter divided by cross slit. Raman intensity of sulfate salts is relatively higher than insoluble dust due to the specific Raman scattering cross section of chemical forms. Thus, to measure the insoluble dust by this method, we have to identify the chemical form of dusts with the several peaks of Raman scattering from dusts. For instance, the

$\text{NaAlSi}_3\text{O}_8$  has several peaks include weaker ones [Chapter 5]. If these peaks corresponded well, then we surely identified the chemical form of mineral dust. If whole peaks not corresponded well, then the microparticles fall into “other” in Figure 2.13.

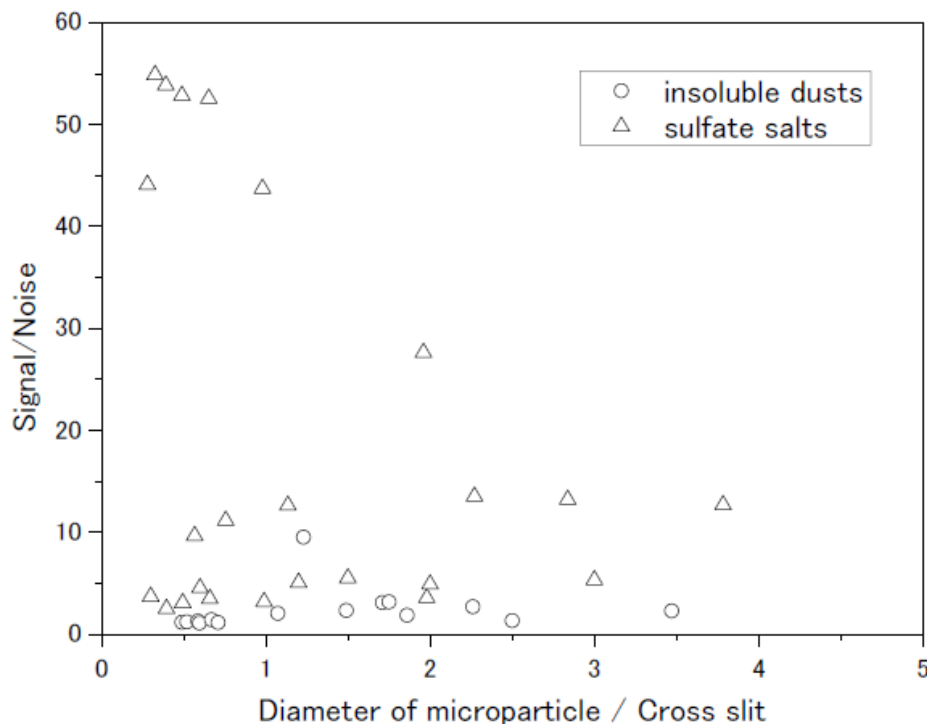


Figure 2.14. The signal-to-noise ratios of the Raman spectra are plotted against the ratio of particle diameter to cross slit width. Sulfate salts yield very intense Raman spectra compared to dust, even though the particles are small.

The theoretical cross-sections of microparticles have previously been described in detail by various aerosol studies [Schweiger, 1987, 1991; Vehring et al., 1995]. The radiant flux  $\Phi$  scattered into a solid angle  $\Omega$  from a single microparticle P with composition A is given by

$$\Phi_{P,A} = \varphi_0 c_A N_a V_P \cdot \int_{\Omega_0} r_A(\lambda_0, \lambda_s) \cdot p(n, x, \theta) d\Omega, \quad (2.1)$$

where  $\varphi_0$  is the radiant flux density of the incident laser beam,  $c_A$  is the molar concentration of composition A,  $N_a$  is Avogadro’s constant, and  $V_P$  is the volume of the microparticle. The Raman scattering cross-section  $r_A$ , included within the integral, depends on the incident wavelength  $\lambda_0$  and Raman wavelength  $\lambda_s$ , but is independent of the microparticle’s morphology. The morphology factor  $p$  is dependent on the refractive index  $n$ , the size  $x$  and the scattering angle  $\theta$ . To understand the relationship between our quantitative Raman spectroscopic measurements and these parameters, it

is necessary to understand the morphology of the microparticles. This is especially true for sulfates, which would not fully understand the refractive index of salts (e.g.  $\text{Na}_2\text{SO}_4 \cdot 10\text{H}_2\text{O}$ ,  $\text{MgSO}_4 \cdot 11\text{H}_2\text{O}$ ,  $\text{CaSO}_4 \cdot 2\text{H}_2\text{O}$ ).

In this study usually uses the best setting of the Raman spectroscopy such as the maximum cross slit is  $3\mu\text{m}$  and the laser power is less than 200mW.

## 2.4 Differential Scanning Calorimetry

### 2.4.1 Setup

We adopted DSC (Rigaku Co., DSC8230) with liquid nitrogen cooling (Figure 2.15). The temperature reproducibility of this instrument is better than  $\pm 0.2^\circ\text{C}$ . Accuracy is based on a three-point temperature calibration using indium ( $156.6^\circ\text{C}$ ), water ( $0.0^\circ\text{C}$ ) ( $18.3\text{m}\Omega$ ) [Schubnell, 2000], and cyclohexane ( $-83.0^\circ\text{C}$ ) [Charsley, 1993]. The DSC cells are made of aluminum. In cases where the samples sublimated during repeated runs, the cells were sealed before use.

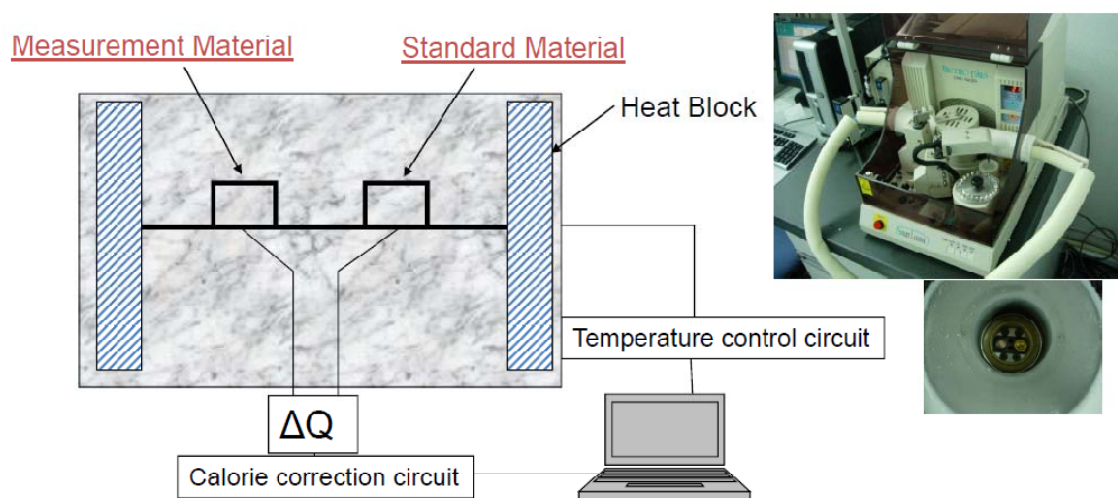


Figure 2.15. Outline of DSC. Standard material is just a blank cell and measurement material is sample solution included in the cell with 10mL of solution.

In this measurement, several binary phase diagrams are reported previously but to discuss the free energy of fusion by our DSC equipment, we measured simple binary phase diagrams focused on  $\text{Na}^+$ ,  $\text{Mg}^{2+}$ ,  $\text{Ca}^{2+}$ ,  $\text{NH}_4^+$ ,  $\text{SO}_4^{2-}$ ,  $\text{NO}_3^-$ ,  $\text{Cl}^-$ ,  $\text{CH}_3\text{SO}_3^-$ ,  $\text{CO}_3^{2-}$  such as  $\text{NaCl} \cdot \text{H}_2\text{O}$ ,  $\text{Na}_2\text{SO}_4 \cdot \text{H}_2\text{O}$ ,  $\text{NaNO}_3 \cdot \text{H}_2\text{O}$ ,  $\text{CH}_3\text{SO}_3\text{Na} \cdot \text{H}_2\text{O}$ ,  $\text{MgCl}_2 \cdot \text{H}_2\text{O}$ ,  $\text{MgSO}_4 \cdot \text{H}_2\text{O}$ ,  $\text{Mg}(\text{NO}_3)_2 \cdot \text{H}_2\text{O}$ ,  $(\text{CH}_3\text{SO}_3)_2\text{Mg} \cdot \text{H}_2\text{O}$ ,  $\text{CaCl}_2 \cdot \text{H}_2\text{O}$ ,  $\text{Ca}(\text{NO}_3)_2 \cdot \text{H}_2\text{O}$ , and  $(\text{CH}_3\text{SO}_3)_2\text{Ca} \cdot \text{H}_2\text{O}$ .

$\text{CaSO}_4 \cdot \text{H}_2\text{O}$  and  $\text{CaCO}_3 \cdot \text{H}_2\text{O}$  could not measure the eutectic temperature of these salts which are very close to the melting of ice (e.g. eutectic of  $\text{CaSO}_4 \cdot \text{H}_2\text{O}$  is  $-0.05^\circ\text{C}$  [Kargel et al., 1992]), because our DSC equipment of minimum error is  $\pm 0.2^\circ\text{C}$ . However, it could not measure whole phase diagram but it can be measured the fusion of eutectic composition. Solutions are prepared with ultrapure water (18.3m $\Omega$ ) by weighing out the required amounts of reagent-grade chemicals 99.5wt% of NaCl (Kishida Chemical), 99.5wt% of  $\text{Na}_2\text{SO}_4$  (Kishida Chemical), 99.0wt% of  $\text{NaNO}_3$  (Kishida Chemical), 98.0wt% of  $\text{MgCl}_2 \cdot 6\text{H}_2\text{O}$  (Kishida Chemical), 99.5wt% of  $\text{MgSO}_4 \cdot 7\text{H}_2\text{O}$  (Kishida Chemical), 99.0wt% of  $\text{Mg}(\text{NO}_3)_2 \cdot 6\text{H}_2\text{O}$  (Kishida Chemical), 95wt% of  $\text{CaCl}_2$  (Kishida Chemical),  $\text{CaSO}_4 \cdot 0.5\text{H}_2\text{O}$  (Kanto Chemical), 98.5wt% of  $\text{Ca}(\text{NO}_3)_2 \cdot 4\text{H}_2\text{O}$  (Kishida Chemical), 98.0wt%  $\text{CH}_3\text{SO}_3\text{Na}$  (Alfa Aesar), 99.0wt%  $(\text{CH}_3\text{SO}_3)_2\text{Mg}$  (Daniels Fine Chemicals), 98.0wt% and 98.0wt%  $(\text{CH}_3\text{SO}_3)_2\text{Ca}$  (Tokyo Kasei Kogyo). Requiring high percentage of these chemicals, we assume that these chemicals are anhydrous, except hydrated in reagent. A cooling and a heating rate are depended on the systems but usually, these rates are  $10^\circ\text{C}/\text{min}$ .

## 2.4.2 Analytical technique of DSC curve

The phase transitions of the solution samples generate typical DSC profiles during the heating (endothermic melting) process. We show the example of phase diagram measured by DSC. One of the chemical species  $\text{NaCl} \cdot \text{H}_2\text{O}$  is measured solution from 0 to 25 wt%. The example of endothermic melting at 1wt% of  $\text{NaCl} \cdot \text{H}_2\text{O}$  solution appeared two endothermal signals (Figure 2.16, 2.17). The definition of temperature is determined by the onset of melting at edge and of latent heat is calculated from the area of fusion. From fusion of temperature and enthalpy, the phase diagram (Figure 2.18) and enthalpy related to latent heat (Figure 2.19) relate to concentration of NaCl can be drawn. The phase diagram shows that the eutectic temperature is  $-21.1^\circ\text{C}$ , meaning the solution of  $\text{NaCl} \cdot \text{H}_2\text{O}$  lower than concentration of 21wt% and the temperature lower than  $-21.1^\circ\text{C}$  form  $\text{NaCl} \cdot n\text{H}_2\text{O}$  (probably  $2\text{H}_2\text{O}$  according to the reference [Usdowski and Dietzel, 1998]). The fitting line of quadratic function, the lowest peak can be calculated by the simple derivation function. On the other hand, when the fitting line could not drawn by the quadratic function, at eutectic composition of solution is measured several samples from same solution and latent heat taken average (e.g.  $\text{CaSO}_4 \cdot \text{H}_2\text{O}$ ). The phase diagram and free energy shows that the most thermodynamically stable concentration of NaCl is 21wt%.

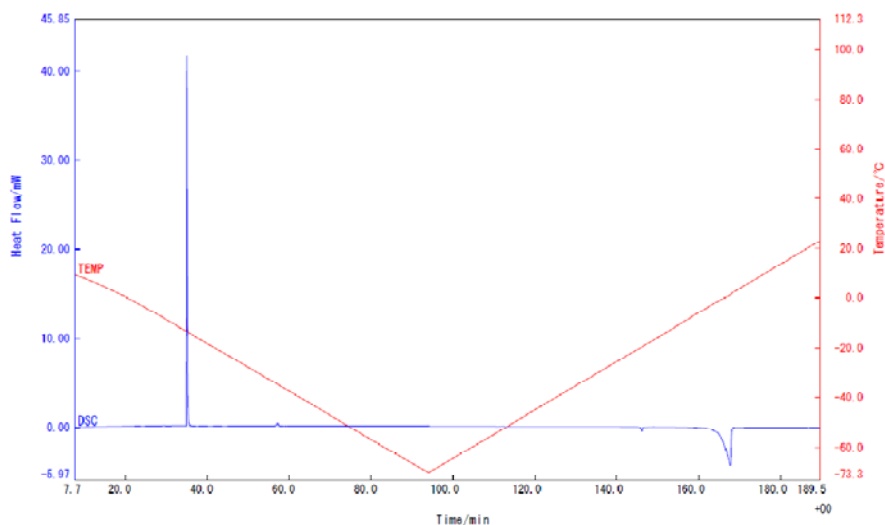


Figure 2.16. Thermogram showing cooling to  $-70^{\circ}\text{C}$  and heating of 1wt% NaCl by DSC. Cooling and heating rate is  $1^{\circ}\text{C}/\text{min}$  for this thermogram. The solution freezes which appears with exothermic heat during cooling process. During heating process, the solution melts which appears with endothermic heat.

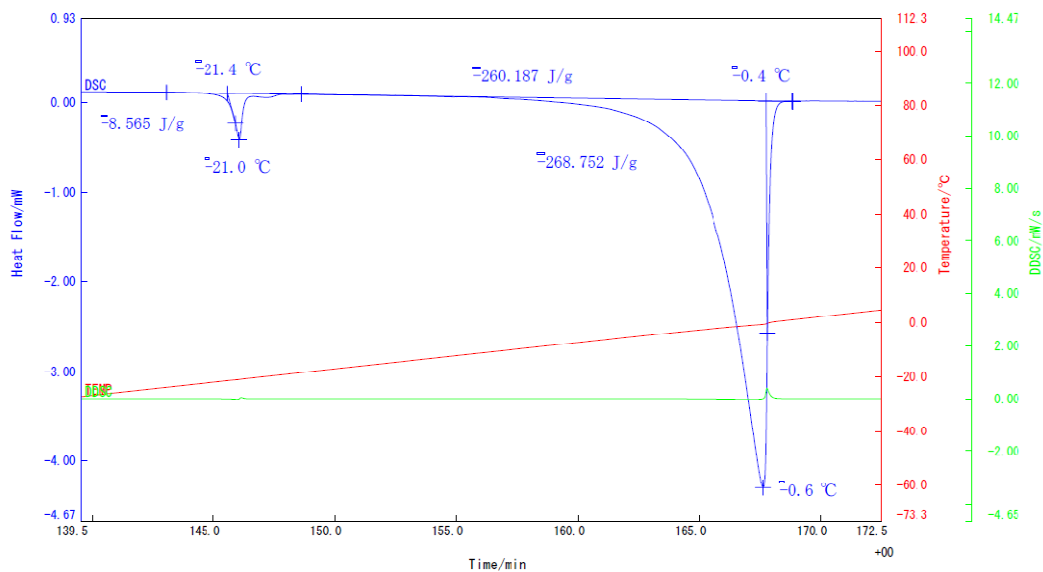


Figure 2.17. Thermograms analytical technique showing heating of 1wt% of NaCl -  $\text{H}_2\text{O}$  at the heating rate at  $1^{\circ}\text{C}/\text{min}$  which are the magnification of heating process of figure 2.16. The areas of two endothermal peaks, such as lower temperature and higher temperature, are latent heat of  $\text{NaCl}\cdot n\text{H}_2\text{O}$  and ice, respectively. These areas and temperature of eutectic and of melting ice are calculated by the software “Thermo Plus 2”, Rigaku co.

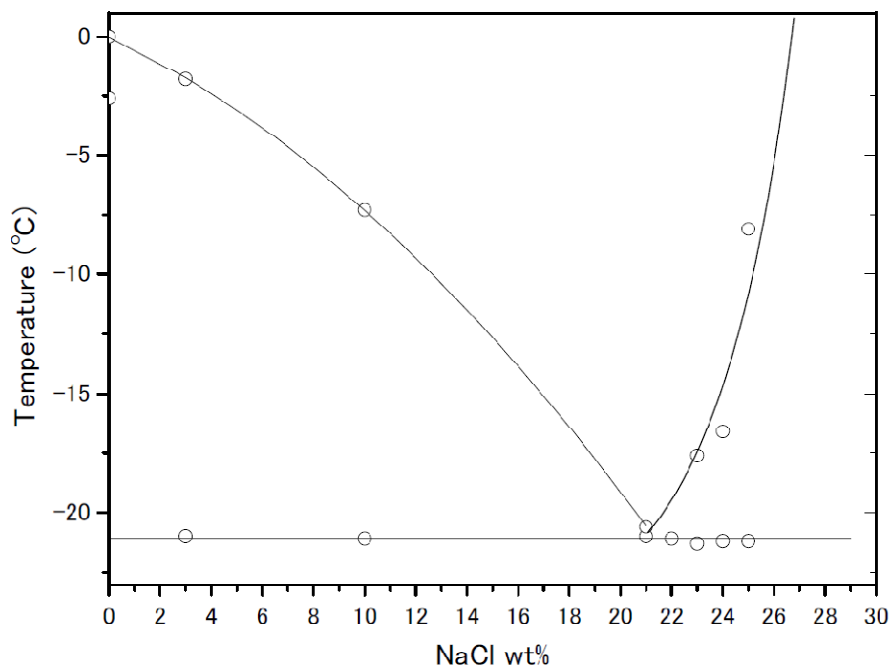


Figure 2.18. Phase diagram of binary system of NaCl - H<sub>2</sub>O. Lines drawn on the phase diagram serve as guides and fitting with the program in the Origin v.7.5. The fitting program for the final melting of ice and solubility line is used quadratic function and eutectic temperature is used just guides at average of eutectic temperature.

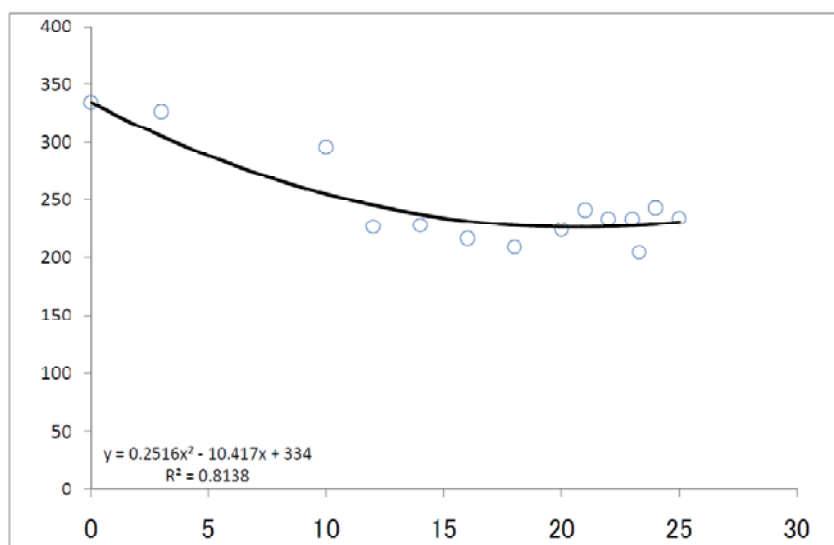


Figure 2.19. Enthalpy of binary system of NaCl - H<sub>2</sub>O. As shown in figure 2.18, the areas of eutectic and final melting are calculated by the software, "Thermo Plus". The area is calculated as a unit of J/g, such as a latent heat of melting. Thus, uniformity the unit, the area is calculated to the unit of kJ/mol considering the density of solution which is measured in advance. The figure shows just the law data of NaCl - H<sub>2</sub>O in unit of J/g. The guide line is calculated by the fitting curve using quadratic function programmed in the Origin v.7.5. The lowest enthalpy of fusion approximately corresponds with the eutectic composition in the system.

## 2.5 SEM-EDS

SEM-EDS analysis determines which chemical elements are present in the microparticles, information that can be used to deduce the chemical compounds. This analysis was performed using a JSM-6360LV (JEOL) SEM system and a JED2201 (JEOL) EDS system. The accelerating voltage of the SEM was 15 keV. The apparatus included an optical probe (Renishaw) to observe the surface of the ice samples. 5.2 mm-diameter cores were extracted from the 6.9 kyrBP (1200.40 m) and 30.0 kyrBP (2099.96 m) sections using a trephine drill (Nobel Biocare). The bases of these specimens were cut down to a height of 3-4 mm using a microtome. Each specimen was put into a stainless steel holder of diameter 5.3 mm and depth 2.5-3.0 mm, held in place with a screw. The sample was kept in an Alto2100 (Gatan) cryo-system during analysis. Inside the SEM chamber, the specimen was sublimated at  $-90\text{ }^{\circ}\text{C}$  until microparticles were exposed on the ice surface. The sublimation rate was approximately  $2\mu\text{m}/\text{min}$  under the condition. The specimen was maintained at  $-135\text{ }^{\circ}\text{C}$  for the remainder of the analysis. The process of sample preparation has previously been described in detail [[Horikawa, personal communications](#)].

## 2.6 Ion Chromatography

Ion chromatography is one of the most common methods of measuring the ionic species present in ice. We decontaminated the ice samples used for ion chromatography by cutting away the surface with a clean ceramic knife, on a clean bench in a clean cold room at  $-15\text{ }^{\circ}\text{C}$ . The decontaminated ice samples were immediately sealed in a clean polyethylene bag. After melting an ice sample in its bag outside the cold room, the sample was passed through a filter with  $0.45\text{ }\mu\text{m}$  pores and then analyzed in a Dionex 500 chromatograph. We measured the concentrations of sodium, magnesium, calcium, chloride, nitrate, and sulfate ions. To test for possible contamination, we measured ultra-pure water using the same methods and found no peaks in the chromatograph spectrum. The process of sample preparation has previously been described in detail [[Iizuka et al., 2006](#)].



# Chapter 3

## Changes of chemical form of the miroparticles during Termination I

### 3.1 Propose

According to previous studies, chemical form of water-soluble microparticles are different in the glacial maximum and interglacial periods (include Holocene) [Ohno et al., 2005, 2006]. This chapter clarify the changes of chemical form of microparticles during drastical climate change (Termination I), in terms of the comparison of the results from measuring the water-soluble microparticles by Raman spectroscopy with the ion balance in terms of the phase equilibrium states of salts.

### 3.2 Number of microparticles

In the ice core samples, various shapes of inclusions were found. When viewed through a 5× objective lens, air hydrates appeared as several hundred microns large, and micro bubbles appeared as several tens of microns large. When viewed through a 50× objective lens, microparticles a few micrometers in diameter were found. The number concentrations of microparticles gradually decreased for ice in the transition from the LGM to the Holocene (Figure 3.1).

The number concentration for the LGM ice was roughly 25 times higher than that for the Holocene ice. The number concentration of the microparticles with the number concentration of dust (1.0–4.0  $\mu\text{m}$ ) was compared. The results show that the water-soluble microparticles had higher concentrations than the insoluble dust microparticles in the ice for each period. The number concentration of microparticles and frequency of the chemical form of microparticles found in ice can be used to calculate the number concentration of each chemical form during Termination I, which is discussed in the following subsections.

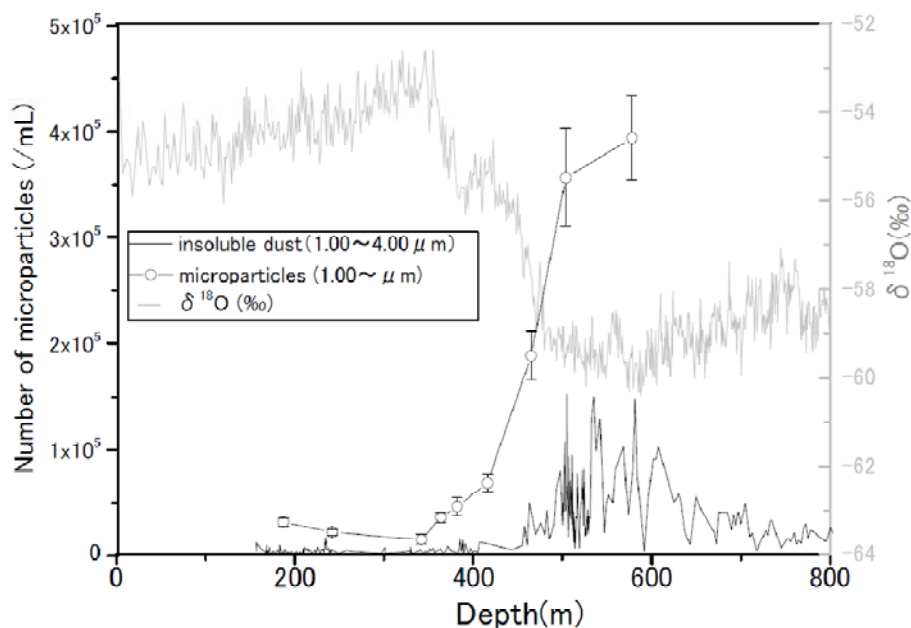


Figure 3.1. The number concentrations of microparticles during Termination I. The data of the insoluble dust and  $\delta^{18}\text{O}$  were from Fujii et al. [2003] and Watanabe et al. [2003], respectively.

### 3.3 Chemical form of microparticles

We found water-soluble microparticles such as mirabilite ( $\text{Na}_2\text{SO}_4 \cdot 10\text{H}_2\text{O}$ ) and meridianiite ( $\text{MgSO}_4 \cdot 11\text{H}_2\text{O}$ ), gypsum ( $\text{CaSO}_4 \cdot 2\text{H}_2\text{O}$ ),  $\text{NO}_3^-$  salt with mirabilite ( $\text{Na}_2\text{SO}_4 \cdot 10\text{H}_2\text{O}$ ) and meridianiite ( $\text{MgSO}_4 \cdot 11\text{H}_2\text{O}$ ), and  $\text{NO}_3^-$  with unknown cation and other chemical forms (probably insoluble dust) during Termination I (Figure 3.2).

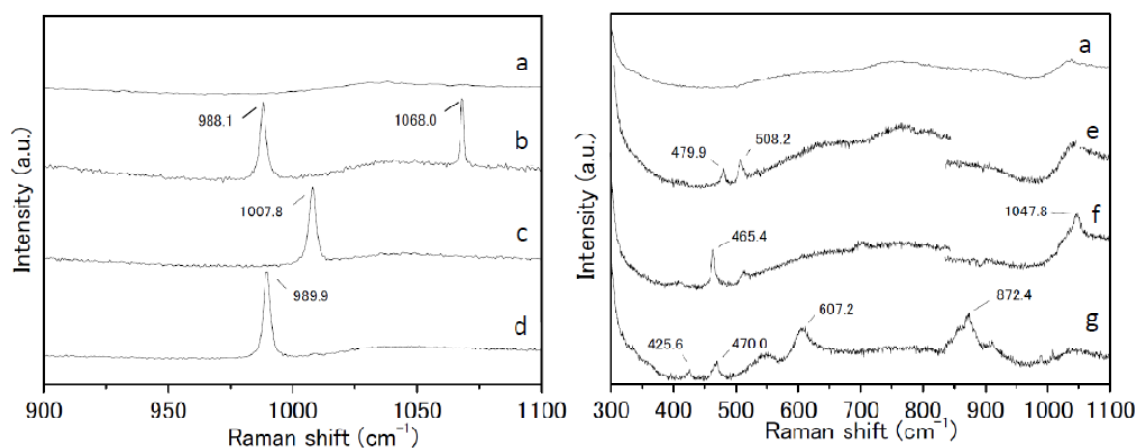


Figure 3.2. The Raman spectra of microparticles found during Termination I in the Dome Fuji ice core: (a) ice, (b)  $\text{SO}_4^{2-}$  and  $\text{NO}_3^-$ , (c)  $\text{CaSO}_4 \cdot 2\text{H}_2\text{O}$  (gypsum), (d)  $\text{Na}_2\text{SO}_4 \cdot 10\text{H}_2\text{O}$  (mirabilite) or  $\text{MgSO}_4 \cdot 11\text{H}_2\text{O}$  (meridianiite), (e)  $\text{NaAlSi}_3\text{O}_8$  (albite), (f)  $\text{SiO}_2$  (quartz), and (g) unknown Raman spectra.

The number concentration for each chemical form was calculated from the number frequency of the chemical forms for microparticles—classified as gypsum, mirabilite and meridianiite, methanesulfonate salts, and other—multiplied by the number concentration of microparticles measured using the optical microscope, as shown in [Figure 3.3](#). The content “other” contained other Raman spectra of insoluble dust, unknown microparticles that could not be identified, no Raman signal other than ice and broken particles ([section 2.3](#)).

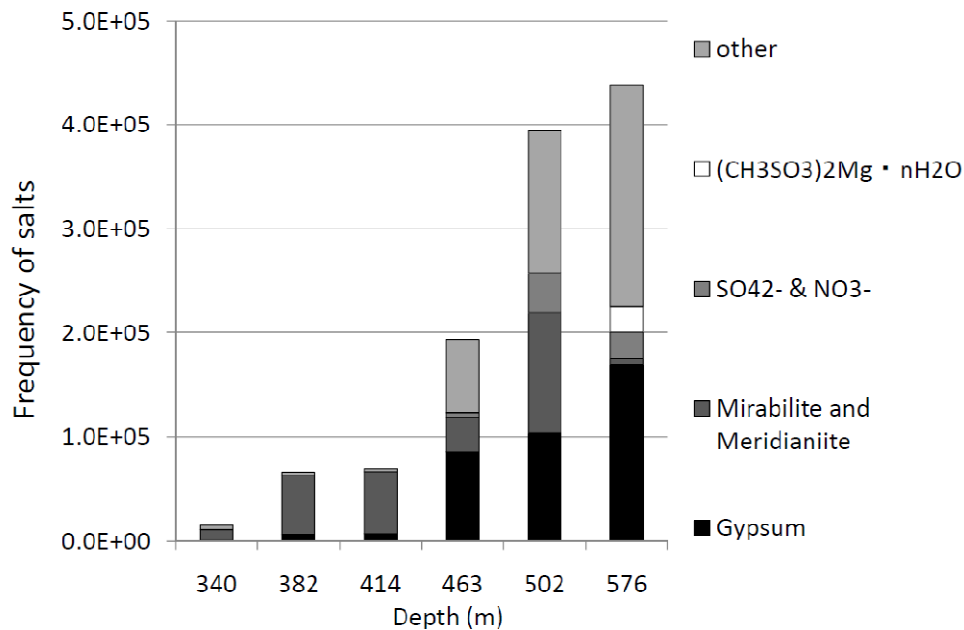


Figure 3.3. Frequency of number concentration of salts during Termination I.

To compare the frequency of salts with the ion concentration in ice, we measured major ions by ion chromatography from samples taken at the exact same depth ([Table 3.1](#)). The relationship between the concentration of Ca<sup>2+</sup> and frequency of CaSO<sub>4</sub>·2H<sub>2</sub>O showed very good correlation. In contrast, the concentration of Na<sup>+</sup> + Mg<sup>2+</sup> (μeq/L) and frequency of Na<sub>2</sub>SO<sub>4</sub>·10H<sub>2</sub>O + MgSO<sub>4</sub>·11H<sub>2</sub>O did not correlate well, especially in the LGM ([Figure 3.4](#)).

depth	Period		Particle Number Concentration	Na <sup>+</sup>	NH <sub>4</sub> <sup>+</sup>	K <sup>+</sup>	Mg <sup>2+</sup>	Ca <sup>2+</sup>	CH <sub>3</sub> SO <sub>3</sub> <sup>-</sup>	Cl <sup>-</sup>	NO <sub>3</sub> <sup>-</sup>	SO <sub>4</sub> <sup>2-</sup>
m	kyr BP		/mL	μmol/L								
340	Holocene	10.3	0.16 × 10 <sup>5</sup>	1.35	0.35	0.35	0.13	0.30	---	1.17	0.54	1.08
382	Termination I	11.8	0.66 × 10 <sup>5</sup>	2.03	0.14	0.21	0.23	0.30	0.20	1.11	0.23	1.08
414	Termination I	13.2	0.69 × 10 <sup>5</sup>	2.55	0.35	0.17	0.30	0.28	0.23	1.15	0.36	1.22
463	Termination I	15.6	1.89 × 10 <sup>5</sup>	3.32	0.20	0.26	0.56	1.06	0.29	3.77	1.37	1.29
502	Termination I	18.5	3.57 × 10 <sup>5</sup>	4.52	0.32	0.39	0.78	1.53	0.20	5.28	1.63	1.99
576	LGM	24.5	3.94 × 10 <sup>5</sup>	5.29	---	0.25	0.89	1.55	0.19	5.36	1.62	2.48

Table 3.1. Microparticles survey during Termination I, Dome Fuji ice core.

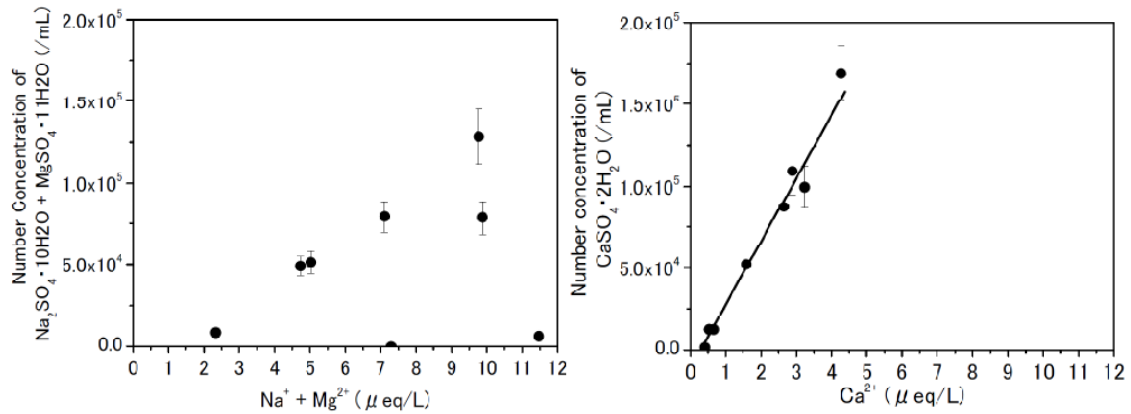


Figure 3.4. The relationship between ion concentration and number of sulfates. The correlation coefficient of  $\text{CaSO}_4 \cdot 2\text{H}_2\text{O}$  and  $\text{Ca}^{2+}$  was 0.86, and that of  $\text{Na}_2\text{SO}_4 \cdot 10\text{H}_2\text{O} + \text{MgSO}_4 \cdot 11\text{H}_2\text{O}$  and  $\text{Na}^+ + \text{Mg}^{2+}$  was 0.08.

Thus, to consider the chemical form of  $\text{Na}^+$  and  $\text{Mg}^{2+}$  in the LGM, we calculated the ion balance with the following equation,

$$\text{noCa}^{2+}\text{SO}_4^{2-} = [\text{SO}_4^{2-} - \text{Ca}^{2+}] - [\text{Na}^+ + \text{Mg}^{2+}] \quad (3.1)$$

and the result is shown in Figure 3.5. The result of this calculation shows the chemical form of  $\text{Na}^+$  and  $\text{Mg}^{2+}$ . If the result of equation 3.1 is close to zero or higher, then  $\text{Na}^+$  and  $\text{Mg}^{2+}$  exist as  $\text{Na}_2\text{SO}_4$  and  $\text{MgSO}_4$ , respectively. If the result is lower than zero, then  $\text{Na}^+$  and  $\text{Mg}^{2+}$  exist in other chemical forms (e.g., chloride, nitrate, methanesulfonate), and this can be seen in Termination I and LGM (except Holocene).

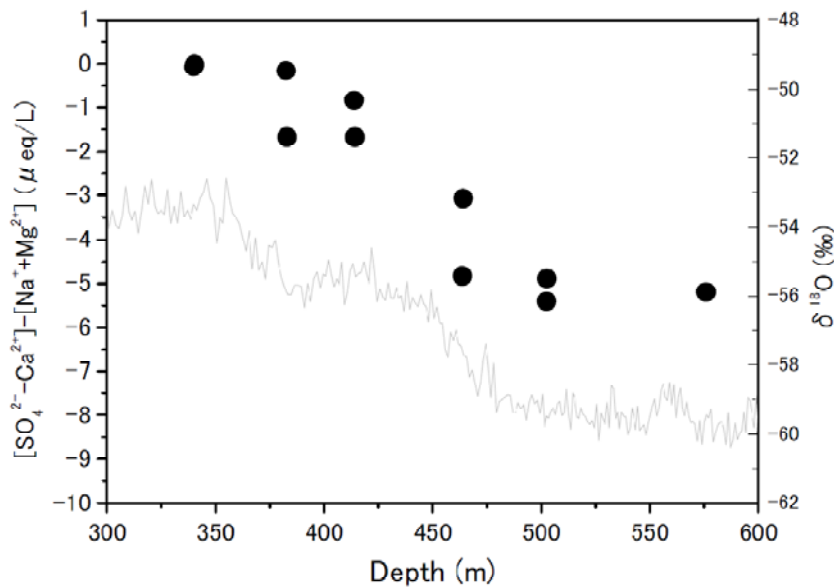


Figure 3.5. Ion balance calculated from equation 3.1, during Termination I. The data of  $\delta^{18}\text{O}$  were from Watanabe et al., 2003.

Previous studies showed that chloride salt may have existed in the LGM [Röthlisberger et al., 2003; Iizuka et al., 2008b]. The above calculation and chemical form measurement results from micro-Raman spectroscopy prove that chloride salts in the region classified as “no Raman spectra” classified into other in figure 3.3.

The question arises as to why this variability can be seen in this Termination and each climatic period. The enthalpy of fusion from the binary phase at eutectic composition of each salts is a key factor in answering this question.

### 3.4 Enthalpy of fusion in binary phase system

The dominant chemical form of a microparticle in phase equilibrium can be inferred by comparing the enthalpies of fusion for each binary phase system measured by DSC (see Chapter 2 for a description of this method). The enthalpy of fusion of a salt-water system, for example, can be decomposed as follows:

$$\Delta H_{\text{dissociation}} = \Delta H_{\text{lattice}} + \Delta H_{\text{hydration}} . \quad (3.2)$$

Here  $\Delta H_{\text{dissociation}}$  is the dissociation energy, which is equal to the enthalpy of fusion,  $\Delta H_{\text{lattice}}$  is the anion-cation lattice energy, and  $\Delta H_{\text{hydration}}$  is the hydration energy. Cation-anion lattice energies (e.g., that of  $\text{Na}_2\text{SO}_4$ ) are reported in numerous sources, but we also have to take into account the hydration number of each chemical form (e.g.,  $\text{Na}_2\text{SO}_4 \cdot 10\text{H}_2\text{O}$ ).

In this study, we compared the enthalpies of fusion (dissociation energies) of binary phase systems for each species found in the microparticles. Each system is assumed to exist in its eutectic composition. For instance, if a cation  $\text{M}^{\text{k}+}$  ( $\text{Na}^+$ ,  $\text{Mg}^{2+}$ , or  $\text{Ca}^{2+}$ ), anions ( $\text{Cl}^-$ ,  $\text{NO}_3^-$  and  $\text{SO}_4^{2-}$ ) and an acid ( $\text{H}^+$ ) coexist in the system, the enthalpy of fusion determines whether  $\text{MSO}_4$  or  $\text{MCl}$  is dominant in the following reaction:



If the enthalpy of fusion of  $\text{MSO}_4 \cdot n\text{H}_2\text{O}$  is higher than that of  $\text{MCl} \cdot n\text{H}_2\text{O}$ , then forming  $\text{MSO}_4 \cdot n\text{H}_2\text{O}$  and  $\text{HCl}$  is relatively frequent in the system.

Table 3.2 shows the enthalpy of fusion for the above reaction at eutectic composition, as a function of temperature and concentration of salt. Based on these enthalpies, the order of salt formation is  $\text{MSO}_4 \cdot n\text{H}_2\text{O} \rightarrow \text{MCl} \cdot n\text{H}_2\text{O} \rightarrow \text{MNO}_3 \cdot n\text{H}_2\text{O}$ , suggesting that sulfate is more likely to form than either chloride or nitrate. This result explains the existence of  $\text{Na}_2\text{SO}_4$  and  $\text{MgSO}_4$  in the Holocene rather than chloride and nitrate salts. It also explains why the less acidic LGM ice [Fujita et al., 2002] has only a smaller amount of  $\text{Na}_2\text{SO}_4$  and  $\text{MgSO}_4$ . These differences have been confirmed directly

by Raman spectroscopy (Figure 3.3).

Since the  $M^{k+}$  binds preferentially to  $SO_4^{2-}$ , the  $Cl^-$  and  $NO_3^-$  ions should exist as excess acids in Holocene ice. Therefore, the ECM signal from Holocene ice should depend mainly on the concentrations of HCl and  $HNO_3$ . In contrast, even though nitrate has the weakest enthalpy of fusion, we found some nitrate in LGM ice due to the abundance of cations that can bind with  $NO_3^-$ . In other words, the ECM signal should decrease due to the existence of nitrate salts. The same relationship holds for chloride salts, which also exist in LGM ice.

	density (solid)	density (liquid)	$\Delta V$ (liquid-solid)	$\Delta H$ (kJ/mol)	eutectic conc.(wt%)	eutectic Temp (°C)	$dt/dp$ (K/bar)	$\Delta T$	$T_m$	depth (m)
NaCl·2H <sub>2</sub> O	1.61	1.17	0.00023	4.9 ± 0.3	23.0	-21.30	0.018	4.0	-17.3	2486
Na <sub>2</sub> SO <sub>4</sub> ·10H <sub>2</sub> O	1.46	1.04	0.00028	5.5 ± 0.6	4.3	-1.30	0.022		-1.3	
NaNO <sub>3</sub>	2.30	1.12	0.00046	3.8 ± 0.3	15.6	-17.50	0.050	11.7	-5.8	2942
MgCl <sub>2</sub> ·6H <sub>2</sub> O	1.57	1.35	0.00010	3.8 ± 0.3	38.6	-31.90	0.009	1.5	-30.4	1863
MgSO <sub>4</sub> ·11H <sub>2</sub> O	1.51	1.19	0.00018	5.8 ± 0.2	17.0	-4.30	0.020	6.1	1.8	
Mg(NO <sub>3</sub> ) <sub>2</sub> ·6H <sub>2</sub> O	1.63	1.08	0.00031	3.6 ± 0.2	13.2	-31.20	0.040	6.4	-24.8	2150
CaCl <sub>2</sub> ·6H <sub>2</sub> O	1.71	1.23	0.00023	3.5 ± 0.2	24.3	-49.90	0.033	1.8	-48.1	737
CaSO <sub>4</sub> ·2H <sub>2</sub> O	2.32	1.00	0.00057	4.4 ± 0.4	0.2	-0.05	0.063		-0.1	
Ca(NO <sub>3</sub> ) <sub>2</sub> ·4H <sub>2</sub> O	1.86	1.50	0.00013	1.7 ± 0.2	38.2	-31.70	0.049	9.0	-22.7	2238
H <sub>2</sub> O	0.92	1.00	-0.00009	6.01		0.00	-0.007	-2.3	-2.3	3080

Table 3.2 Parameters of various water-soluble salts: the densities of solid and liquid, the difference in volume between solid and liquid, the enthalpy of fusion for a binary phase at the eutectic concentration, the eutectic concentration, the eutectic temperature,  $dt/dp$  calculated from the Calusius-Clapeyron equation (the derivative of melting temperature with respect to pressure) at depth in the Dome Fuji ice core, the melting temperature at depth, and the depth at which the salt melts. The hydration numbers given for these salts are informed by the data in this table, but some salts could have a different number of hydrates. For example, Genceli et al. [2007] found  $MgSO_4 \cdot 11H_2O$  but not  $MgSO_4 \cdot 12H_2O$ . The eutectic parameters and enthalpies of fusion were measured during this study (except  $H_2O$ ). The densities are widely reported (e.g., CRC handbook 2001, Chemical Book: [http://www.chemicalbook.com/ProductIndex\\_JP.aspx](http://www.chemicalbook.com/ProductIndex_JP.aspx) and RRUFF: <http://rruff.info/>).

Given the bifurcation diagram of ion species in the ice sheet [Iizuka et al., 2008b], and taking into account the enthalpies of fusion measured for phase equilibrium states, we can estimate the concentration of each chemical form in each climatic period from ion balance principles (Figure 3.6). To demonstrate the validity of this approach, we calculated correlation coefficients  $\rho$  between concentrations estimated by ion balance and those measured by micro-Raman spectroscopy. The results were  $\rho=0.86$  ( $P = 0.01$ ),  $\rho=0.16$  ( $P = 0.1$ ),  $\rho=0.99$  ( $P = 0.05$ ), and  $\rho=0.85$  ( $P = 0.01$ ) for  $CaSO_4 \cdot 2H_2O$  (gypsum),  $Na_2SO_4 \cdot 10H_2O$  and  $MgSO_4 \cdot 11H_2O$ , nitrate salts, and chloride salts (microparticles with no Raman signals) respectively. The strong correlations suggest that estimating correlations by ion balance is mostly correct (total correlation coefficient: 0.58 ( $P = 0.01$ )). The poor correlation of  $Na_2SO_4 \cdot 10H_2O$  and  $MgSO_4 \cdot 11H_2O$  estimates is discussed below.

There is evidence for bias in some of the relationships. [Figure 3.4](#) shows the relationship between the ion concentration and the number of  $\text{CaSO}_4 \cdot 2\text{H}_2\text{O}$  particles. In this analysis we assumed that most of the  $\text{Ca}^{2+}$  ions exist as  $\text{CaSO}_4 \cdot 2\text{H}_2\text{O}$ , but the correlation line at the bottom describes an excess of  $0.17 \mu\text{eq/L}$  of  $\text{Ca}^{2+}$ . That is,  $0.17 \mu\text{eq/L}$  of  $\text{Ca}^{2+}$  must exist in other forms such as  $\text{Ca}(\text{NO}_3)_2 \cdot n\text{H}_2\text{O}$  or  $\text{CaCl}_2 \cdot n\text{H}_2\text{O}$  at each depth. The eutectic temperatures of  $\text{Ca}(\text{NO}_3)_2 \cdot n\text{H}_2\text{O}$  and  $\text{CaCl}_2 \cdot n\text{H}_2\text{O}$  are  $-31.7^\circ$  and  $-49.9^\circ\text{C}$  respectively [[Table 3.2](#)]. Thus, both chemical forms can exist under the temperature conditions that existed during Termination I [[Hondoh et al., 2002](#)].

Our estimations of  $\text{Na}_2\text{SO}_4 \cdot 10\text{H}_2\text{O}$  and  $\text{MgSO}_4 \cdot 11\text{H}_2\text{O}$  were based on their phase equilibrium state in the ice sheet. However, the chemical reactions



would not have completely reached equilibrium even at the Termination I depth (340–576 m). For this reason, our ion balance calculations for the chemical forms  $\text{Na}_2\text{SO}_4 \cdot 10\text{H}_2\text{O}$  and  $\text{MgSO}_4 \cdot 11\text{H}_2\text{O}$  were highly uncertain, explaining the weak correlation coefficient of 0.16 ( $P=0.1$ ).

For equilibrium states in the ice sheet, this research has demonstrated the possibility of chemical formation in ice core but we discussed only including the binary phase diagrams of salts which would suggest that the mechanism of bifurcation of chemical form is needed to discuss with the ternary phases of salts and thus it is still unconcluded.

The chemicals precipitated on ice sheets as water-soluble aerosols, but the above reactions may have occurred in the firn (near the surface of ice sheet) [[Iizuka et al., 2006](#)]. Further study of the firn [e.g., [Tsuchimoto, master thesis](#)] will enhance the accuracy of this estimation method for the chemical forms of  $\text{Na}^+$ ,  $\text{Mg}^{2+}$ ,  $\text{SO}_4^{2-}$ ,  $\text{Cl}^-$ , and  $\text{H}^+$  in past atmospheres.

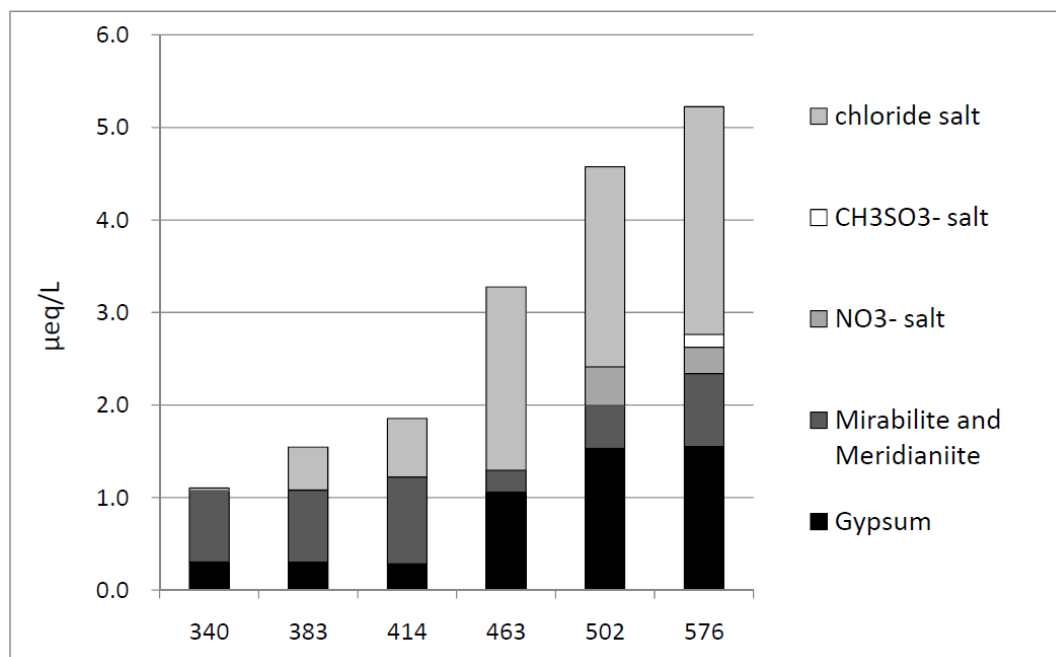


Figure 3.6. Chemical form of microparticles estimated from ion balance.

# Chapter 4

## $(\text{CH}_3\text{SO}_3)_2\text{Mg}\cdot n\text{H}_2\text{O}$ found in the Dome Fuji ice core

### 4.1 Purpose

This study investigate the identification of methanesulfonate salt in ice core using micro Raman spectroscopy and propose the formation process of methanesulfonate salt found in Dome Fuji ice core from the phase diagrams measured by Differential Scanning Calorimetry (DSC) and Raman spectra of methanesulfonate salts.

### 4.2 Raman spectra of methanesulfonate salts

We measured the Raman spectra of several reference specimens: the simple salts  $\text{CH}_3\text{SO}_3\text{Na}$ ,  $(\text{CH}_3\text{SO}_3)_2\text{Mg}$ ,  $\text{CH}_3\text{SO}_3\text{K}$  and  $(\text{CH}_3\text{SO}_3)_2\text{Ca}$  (Figure 4.1), and their solutions at eutectic composition (section 3.3) (Figure 4.2). (In the case of  $(\text{CH}_3\text{SO}_3)_2\text{Ca}$  we measured a 42 wt% solution, which is close to the eutectic composition.) The methanesulfonate salts show three major peaks around  $1050\text{-}1100\text{ cm}^{-1}$ ,  $2930\text{-}2950\text{ cm}^{-1}$ , and  $3010\text{-}3030\text{ cm}^{-1}$ . The peak around  $1050\text{-}1100\text{ cm}^{-1}$  can be assigned to the  $\text{SO}_3^{2-}$  stretching frequencies [Socrates, 2001; Barletta et al., 2009]. The peaks around  $2930\text{-}2950\text{ cm}^{-1}$  and  $3010\text{-}3030\text{ cm}^{-1}$  can be assigned to  $\text{CH}_3$  symmetric stretching and  $\text{CH}_3$  antisymmetric stretching respectively [Socrates, 2001; Durig et al., 2000; Barletta et al., 2009].

The Raman spectra of the simple salt and the spectra of eutectic solutions are significantly different, especially for  $\text{SO}_3^{2-}$ , OH and  $\text{CH}_3$  stretching frequencies. The  $\text{SO}_3^{2-}$  stretching mode causes a peak at  $1084.0\text{ cm}^{-1}$  for the  $(\text{CH}_3\text{SO}_3)_2\text{Mg}$  salt. The  $(\text{CH}_3\text{SO}_3)_2\text{Mg} \cdot \text{H}_2\text{O}$  solution, on the other hand, has a peak at  $1054.9\text{ cm}^{-1}$ . The OH stretching of simple salts could not appear except  $(\text{CH}_3\text{SO}_3)_2\text{Mg}$ , probably from contaminated in reagent of  $(\text{CH}_3\text{SO}_3)_2\text{Mg}$ . The structures in solutions, on the other hand, have a large peak around  $3000\text{ to }3500\text{ cm}^{-1}$  from OH stretching frequencies. More interest result from this measurement is  $\text{CH}_3$  symmetric stretching and antisymmetric

stretching from  $3010\text{-}3030\text{cm}^{-1}$ . These spectra from simple salts, we could detect sprits. For instance,  $(\text{CH}_3\text{SO}_3)_2\text{Mg}$  has  $3021.8$  and  $3028.6\text{cm}^{-1}$  from  $\text{CH}_3$  antisymmetric stretching. From  $(\text{CH}_3\text{SO}_3)_2\text{Mg} \cdot \text{H}_2\text{O}$  sample, on the other hand, could not be detected sprits from  $\text{CH}_3$  antisymmetric stretching but a simple sharp peak at  $3020.9\text{cm}^{-1}$ . These disagreements must cause by the crystal structure. Thus, these results suggest that hydrate is forming in the crystal structure of the methanesulfonate salt, i.e., the structure in solution is  $(\text{CH}_3\text{SO}_3)_2\text{Mg}\cdot n\text{H}_2\text{O}$ .

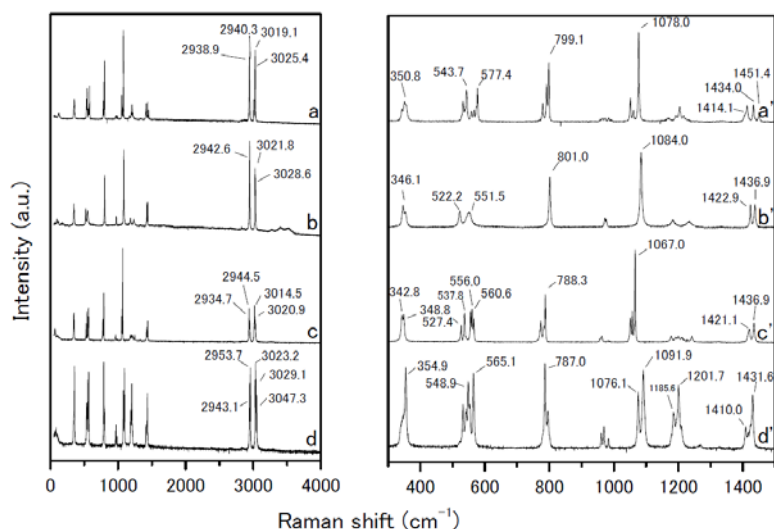


Figure 4.1. Raman spectra a, b, c and d (primes: magnification from  $300 - 1500\text{cm}^{-1}$ ) are regent grade of  $\text{CH}_3\text{SO}_3\text{Na}$ ,  $(\text{CH}_3\text{SO}_3)_2\text{Mg}$ ,  $\text{CH}_3\text{SO}_3\text{K}$  and  $(\text{CH}_3\text{SO}_3)_2\text{Ca}$  respectively. The right-hand spectra are magnifications from  $300$  to  $1500\text{cm}^{-1}$ . Raman spectra of the sharp peaks are also given.

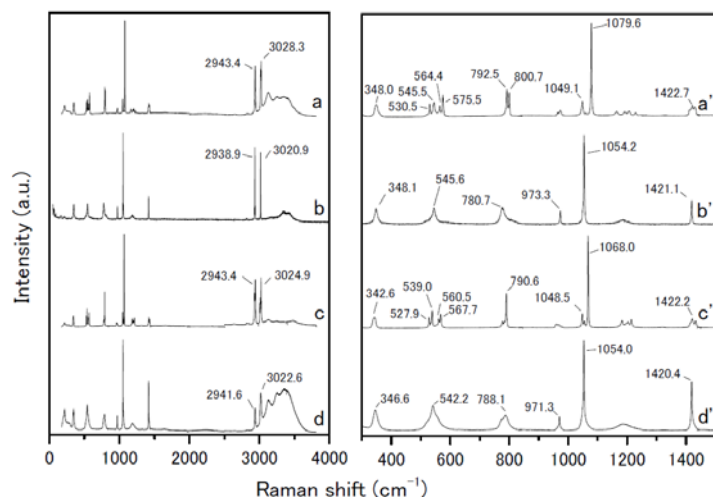


Figure 4.2. Raman spectra a, b, c and d are (primes: magnification from  $300 - 1500\text{cm}^{-1}$ ) eutectic solutions of  $\text{CH}_3\text{SO}_3\text{Na}\cdot n\text{H}_2\text{O}$ ,  $(\text{CH}_3\text{SO}_3)_2\text{Mg}\cdot n\text{H}_2\text{O}$ ,  $\text{CH}_3\text{SO}_3\text{K}\cdot n\text{H}_2\text{O}$  and  $(\text{CH}_3\text{SO}_3)_2\text{Ca}\cdot n\text{H}_2\text{O}$  respectively. The right-hand spectra are magnifications from  $300$  to  $1500\text{cm}^{-1}$ . These spectra were measured at lower than eutectic temperature.

### 4.3 Chemical form of methanesulfonate salts in the ice core

We found micro-inclusions with Raman spectra very similar to methanesulfonate salts. The salt particle was *only* present in LGM (576.50m) ice among the six depths considered here. Furthermore, no other types of methanesulfonate salt were found among the 755 micro-inclusions examined (about 100 micro inclusions were obtained from each of the six core samples). The inclusions were typically several microns in diameter (a photograph is shown in Figure 4.3).

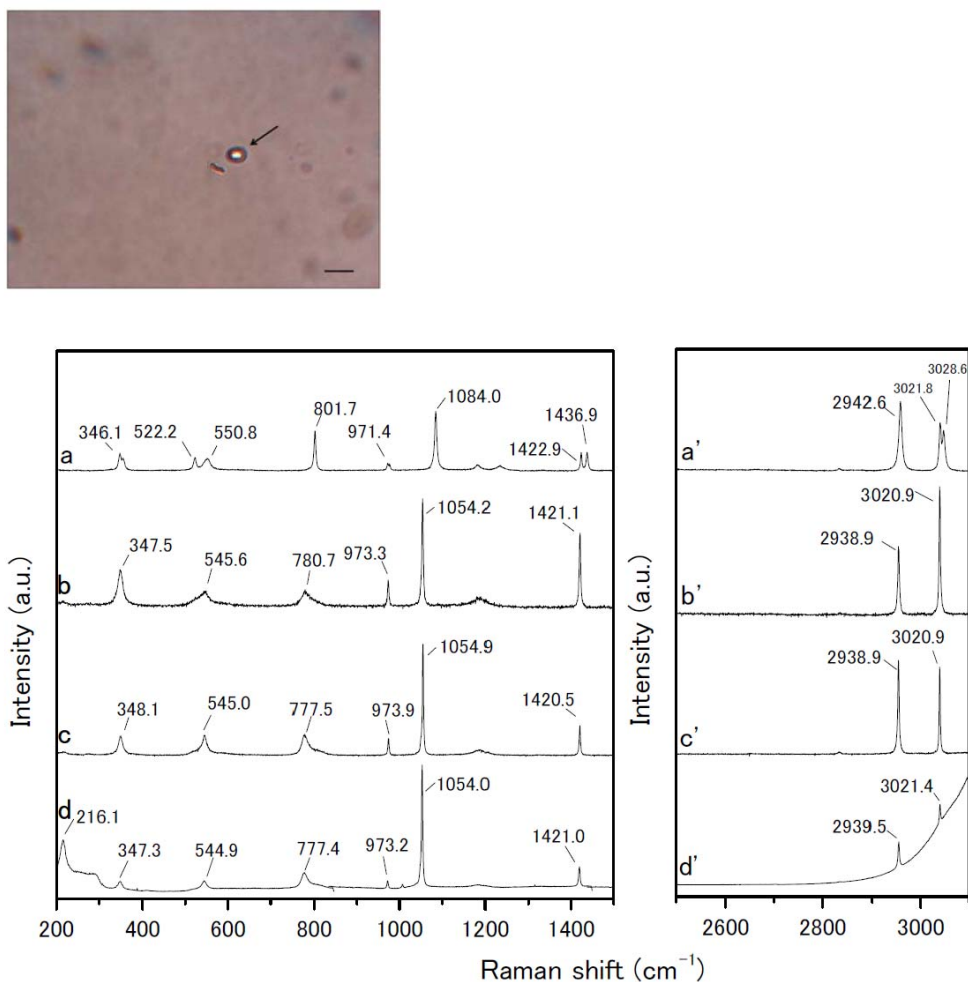


Figure 4.3. Optical microscopy of a methanesulfonate salt inclusion in the ice sample (arrow). The scale bar is  $10\mu\text{m}$ . Raman spectra a, b, c, and d from 200 to  $1500\text{cm}^{-1}$  (primes: from  $2500 - 3100\text{cm}^{-1}$ ) below the photograph come from  $(\text{CH}_3\text{SO}_3)_2\text{Mg}$ ,  $(\text{CH}_3\text{SO}_3)_2\text{Mg}\cdot n\text{H}_2\text{O}$  (after standing at room temperature for several days and measured at  $-30^\circ\text{C}$ ),  $(\text{CH}_3\text{SO}_3)_2\text{Mg}\cdot n\text{H}_2\text{O}$ , and methanesulfonate salt inclusion from the Dome Fuji ice core (arrow in picture), respectively.

To identify the chemical form of the methanesulfonate salts present in the ice core, the Raman spectra of micro-inclusions (Figure 6.3) were compared to reference spectra. The Raman spectra of methanesulfonate salt inclusions found in the Dome Fuji ice were found to correspond with the  $(\text{CH}_3\text{SO}_3)_2\text{Mg}\cdot n\text{H}_2\text{O}$  reference specimen, *not* with the anhydrous  $(\text{CH}_3\text{SO}_3)_2\text{Mg}$  specimen or any other form. The Raman spectra of  $(\text{CH}_3\text{SO}_3)_2\text{Ca}\cdot n\text{H}_2\text{O}$  and  $(\text{CH}_3\text{SO}_3)_2\text{Mg}\cdot n\text{H}_2\text{O}$  are very similar in many respects. The two spectra can be distinguished by their symmetric and antisymmetric  $\text{CH}_3$  stretching frequencies:  $2938.9\text{ cm}^{-1}$  and  $3020.9\text{ cm}^{-1}$  for  $(\text{CH}_3\text{SO}_3)_2\text{Mg}\cdot n\text{H}_2\text{O}$ , and  $2941.6\text{ cm}^{-1}$  and  $3023.1\text{ cm}^{-1}$  for  $(\text{CH}_3\text{SO}_3)_2\text{Ca}\cdot n\text{H}_2\text{O}$ . We used Gaussian fitting to estimate the positions and half-bandwidths of the peaks, and the differences between corresponding. The half-bandwidths of  $2938.9\text{ cm}^{-1}$  and  $3020.9\text{ cm}^{-1}$  for methanesulfonate salt in ice core are  $3.9\pm 0.1\text{ cm}^{-1}$  and  $2.9\pm 0.9\text{ cm}^{-1}$ , and the half-bandwidths of  $2941.6\text{ cm}^{-1}$  and  $3023.1\text{ cm}^{-1}$  for  $(\text{CH}_3\text{SO}_3)_2\text{Ca}\cdot n\text{H}_2\text{O}$  are  $15.8\pm 0.2\text{ cm}^{-1}$  and  $23.7\pm 3.4\text{ cm}^{-1}$ , respectively. This result strongly suggests that the methanesulfonate salt found in the ice core is *not*  $(\text{CH}_3\text{SO}_3)_2\text{Ca}\cdot n\text{H}_2\text{O}$  *but*  $(\text{CH}_3\text{SO}_3)_2\text{Mg}\cdot n\text{H}_2\text{O}$ .

To evaluate the structural phase transition during preservation, we left the  $(\text{CH}_3\text{SO}_3)_2\text{Mg}\cdot \text{H}_2\text{O}$  solution in a Petri dish at room temperature for several days to sublimate the water, then measured the Raman spectrum of the sample. The resulting spectrum is clearly  $(\text{CH}_3\text{SO}_3)_2\text{Mg}\cdot n\text{H}_2\text{O}$ , not  $(\text{CH}_3\text{SO}_3)_2\text{Mg}$  (Figure 4.3 b, c). This result suggests that once  $(\text{CH}_3\text{SO}_3)_2\text{Mg}\cdot n\text{H}_2\text{O}$  has formed, it can be preserved as a structure of hydrate.

## 4.4 Binary phase diagram of methanesulfonate salts

The phase transitions of  $\text{CH}_3\text{SO}_3\text{Na}\cdot \text{H}_2\text{O}$ ,  $(\text{CH}_3\text{SO}_3)_2\text{Mg}\cdot \text{H}_2\text{O}$ ,  $\text{CH}_3\text{SO}_3\text{K}\cdot \text{H}_2\text{O}$ , and  $(\text{CH}_3\text{SO}_3)_2\text{Ca}\cdot \text{H}_2\text{O}$  generate typical DSC profiles during the heating (endothermic melting) process. The phase diagrams of the solutions are shown in Figure 4.4.

**$\text{CH}_3\text{SO}_3\text{Na} - \text{H}_2\text{O}$ .** We performed measurements in the composition range 0 to 52wt% (Figure 4.4a). From the lower endothermic peak, the eutectic temperature of this salt is  $-29.3 \pm 0.2^\circ\text{C}$ . The higher endothermic peak is attributed to a decrease in the melting point of the ice. Concentrations higher than 50wt%  $\text{CH}_3\text{SO}_3\text{Na}\cdot \text{H}_2\text{O}$  were deposited from the solution at room temperature. The enthalpy of fusion at a eutectic composition of 50 wt% is  $\Delta H_{\text{Na}} = 12.6 \pm 0.9\text{ kJ/mol}$ .

**$(\text{CH}_3\text{SO}_3)_2\text{Mg} - \text{H}_2\text{O}$ .** We performed measurements in the composition range 0 to 36wt%

(Figure 4.4b). The average eutectic transition temperature over all samples is  $-5.0 \pm 0.5^\circ\text{C}$ . Above a solute concentration of 14wt%, salt deposition occurred at room temperature. The enthalpy of fusion at a eutectic composition of 14wt% is  $\Delta H_{\text{Mg}}=13.3 \pm 0.04\text{kJ/mol}$ .

**$\text{CH}_3\text{SO}_3\text{K} - \text{H}_2\text{O}$ .** We performed measurements in the composition range 0 to 60 wt% (Figure 4.4c). The average eutectic transition temperature is  $-17.8 \pm 0.1^\circ\text{C}$ . The enthalpy of fusion at a eutectic composition of 44 wt% is  $\Delta H_{\text{K}}=17.9 \pm 0.08\text{kJ/mol}$ .

**$(\text{CH}_3\text{SO}_3)_2\text{Ca} - \text{H}_2\text{O}$ .** We performed measurements in the composition range 0 to 44wt% (Figure 4.4d). The average eutectic transition temperature is  $-32.6 \pm 0.2^\circ\text{C}$ . At compositions of 44 wt% or higher, our measurements of this compound were not easily reproducible although other species were detectable at their eutectic compositions. We therefore do not have a good estimate for the enthalpy of fusion, but one profile gave  $\Delta H_{\text{Ca}}=0.46\pm 0.04\text{ kJ/mol}$ .

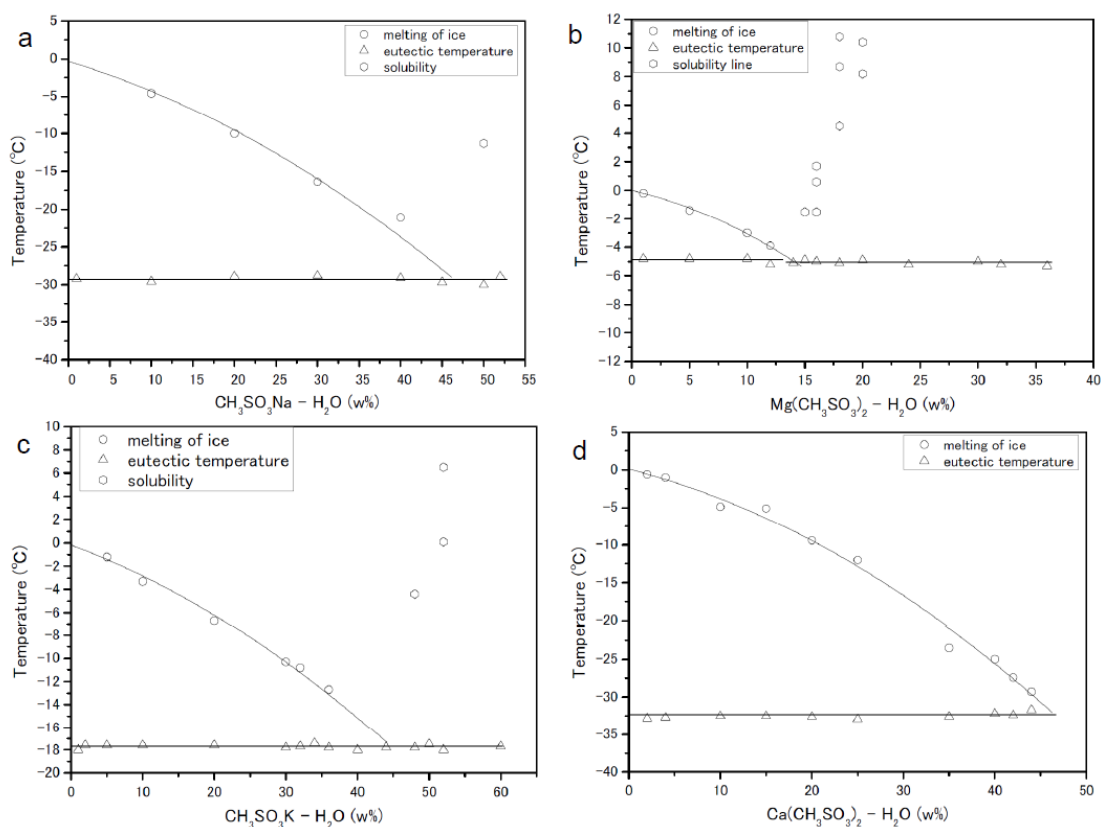


Figure 6.4. Phase diagrams a, b, c and d correspond to  $\text{CH}_3\text{SO}_3\text{Na} \cdot \text{H}_2\text{O}$  ( $-29.3\pm 0.2$ ),  $(\text{CH}_3\text{SO}_3)_2\text{Mg} \cdot \text{H}_2\text{O}$  ( $-5.0\pm 0.5$ ),  $\text{CH}_3\text{SO}_3\text{K} \cdot \text{H}_2\text{O}$  ( $-17.8\pm 0.1$ ), and  $(\text{CH}_3\text{SO}_3)_2\text{Ca} \cdot \text{H}_2\text{O}$  ( $-32.6\pm 0.2^\circ\text{C}$ ) respectively.

## 4.5 The Formation mechanism of $(\text{CH}_3\text{SO}_3)_2\text{Mg}\cdot n\text{H}_2\text{O}$

The eutectic temperature of  $(\text{CH}_3\text{SO}_3)_2\text{Mg}\cdot n\text{H}_2\text{O}$  ( $-5.0 \pm 0.5^\circ\text{C}$ ) is much higher than that of the Dome Fuji ice core. The average temperature of the core at a depth of 10 m is  $-58^\circ\text{C}$ , and its deepest recorded temperature (from the first Dome Fuji ice core project) at 2503 m is about  $-10^\circ\text{C}$  [Hondoh et al., 2002]. This result indicates that  $(\text{CH}_3\text{SO}_3)_2\text{Mg}\cdot n\text{H}_2\text{O}$  is thermodynamically stable in the Dome Fuji ice core between the surface and 2503 m.

We shall now propose two formation mechanisms for  $(\text{CH}_3\text{SO}_3)_2\text{Mg}\cdot n\text{H}_2\text{O}$  in Antarctica, one in the firn of ice sheet and the other in the air of the ice edge.

### 4.5.1 In the firn of ice sheet, Antarctica

In a previous study using ion chromatography on a coastal ice core obtained at Dolleman Island, Antarctica, Mulvaney et al. [1992] suggested that the concentration of  $\text{CH}_3\text{SO}_3^-$  in the winter layer, which was relocated from the summer layer, determined whether sodium methanesulfonate or magnesium methanesulfonate would form in a depth of several meters. In their core the temperature at 10 m depth was  $-16.8^\circ\text{C}$ , suggesting that deeper ice might be at higher temperatures. Taking into consideration our data on the eutectic temperatures of methanesulfonate salts,  $\text{CH}_3\text{SO}_3\text{Na}\cdot n\text{H}_2\text{O}$  ( $-29.3^\circ\text{C}$ ) could *not* be present in the Dolleman Island ice core but  $(\text{CH}_3\text{SO}_3)_2\text{Mg}\cdot n\text{H}_2\text{O}$  ( $-5.0^\circ\text{C}$ ) should be.

It is also possible for methanesulfonate salt to form in the firn of Antarctica's inland ice sheet. At present the annual mean temperature at Dome Fuji station is  $-54.4^\circ\text{C}$  [Yamanouchi et al., 2003]. During the LGM, the surface temperature was determined to be roughly  $-60^\circ\text{C}$  from stable isotope study [Watanabe et al., 2003], and  $\text{Na}^+$  is the most abundant and  $\text{Mg}^{2+}$  is one of minor among cation in both period of ice, according to the ion chromatography [e.g. Watanabe et al., 2003, Iizuka et al., 2004, 2006]. These previous ice core studies suggest that  $\text{CH}_3\text{SO}_3\text{Na}\cdot n\text{H}_2\text{O}$  can form at the surface of the Dome Fuji ice during both periods, and  $(\text{CH}_3\text{SO}_3)_2\text{Mg}\cdot n\text{H}_2\text{O}$  is probably minor compound in Dome Fuji ice core. However, except  $(\text{CH}_3\text{SO}_3)_2\text{Mg}\cdot n\text{H}_2\text{O}$  in LGM ice, we did not find any methanesulfonate salts among 755 micro-inclusions from our ice core samples. In the firn of Dome Fuji ice core, this result may be explained if after the formation of methanesulfonate salts through the reaction of  $\text{CH}_3\text{SO}_3\text{H}$  and sea salt, a reverse reaction is dominant between methanesulfonate salts and other acids to form

other salts, especially in Holocene and Termination I which is acidic ice condition [Röthlisberger et al., 2003; Iizuka et al., 2008].

In the LGM, the formation process is fixation on alkaline particles of marine or continental origin during long-range aerosol transport to polar areas [Delmas et al., 2003], and the formation of HCl was strongly reduced because high levels of dust neutralized the acids [Röthlisberger et al., 2003] to form (chloride) salts [Iizuka et al., 2008]. The neutralization in the LGM ice can explain the existence of  $(\text{CH}_3\text{SO}_3)_2\text{Mg}\cdot n\text{H}_2\text{O}$ , but the above discussion in Dome Fuji ice core cannot explain where it was formed as the reverse reaction would have produced acidic conditions in the LGM ice and/or at least  $\text{CH}_3\text{SO}_3\text{H}$  might sublime from firm after reverse reaction. Hence, we propose the other formation mechanism that  $(\text{CH}_3\text{SO}_3)_2\text{Mg}\cdot n\text{H}_2\text{O}$  may be transported as an aerosol in the LGM atmosphere. The salt was then deposited on the ice sheet, where it had a chance to survive and be preserved in ice as neutralized the acids.

### 4.5.2 In the air of Antarctica's ice edge

Taking into account the possibility of neutralized acid in the LGM, we propose that  $(\text{CH}_3\text{SO}_3)_2\text{Mg}\cdot n\text{H}_2\text{O}$  formed in the air around Antarctica's ice edge.  $\text{CH}_3\text{SO}_3\text{H}$  is formed by the oxidation of DMS, which is emitted by biological activities [e.g. Saltelli et al., 1995] on the open sea. Sea salts are emitted by sea spray, and probably accumulate in certain forms of surface sea ice (such as frost flowers) [e.g. Rankin et al., 2002]. The various salts present in a frost flower would fractionate according to their eutectic temperatures and ratios in bulk sea water [Beaudon and Moore, 2009], suggesting that  $\text{MgCl}_2\cdot 12\text{H}_2\text{O}$  (eutectic temperature:  $-36.0^\circ\text{C}$  [Marion et al., 1999]) can exist in frost flowers.

The air temperature at the surface of the sea ice is a key factor to discuss the formation process of  $(\text{CH}_3\text{SO}_3)_2\text{Mg}\cdot n\text{H}_2\text{O}$ . For instance, the air temperature ranges from  $+2^\circ\text{C}$  to  $-21^\circ\text{C}$  in Bellingshausen Sea, Antarctica; the surface temperature close to the ice edge should be slightly higher [Turner et al., 2003]. Then, given our data on the eutectic temperatures of various methanesulfonates, we find that  $(\text{CH}_3\text{SO}_3)_2\text{Mg}\cdot n\text{H}_2\text{O}$  is the salt that most readily forms at the edges of sea ice. The chemical reaction is between  $\text{CH}_3\text{SO}_3\text{H}$  and  $\text{MgCl}_2$  (probably in the liquid phase), and probably occurs on the frost flower and in the air. This could explain why only  $(\text{CH}_3\text{SO}_3)_2\text{Mg}\cdot n\text{H}_2\text{O}$  among the methanesulfonate salts is found in the LGM ice. Our preservation experiment (Figure

4.3) suggests that no structural phase transition of  $(\text{CH}_3\text{SO}_3)_2\text{Mg}\cdot n\text{H}_2\text{O}$  occurs, even at the high temperature, during its transportation from the ice edge to the inland ice sheet. The temperature of inland Antarctica drops as one travels from Syowa station (on the coast) to Dome Fuji [Takahashi et al., 1998]. These facts suggest that  $(\text{CH}_3\text{SO}_3)_2\text{Mg}\cdot n\text{H}_2\text{O}$  formed easily during its transportation from the coast to inland Antarctica.

# Chapter 5

## Finding of sulfate salts as liquid microparticles in the Dome Fuji ice core

### 5.1 Purpose

In this work, we present the chemical forms of microparticles found in deeper parts of the Dome Fuji ice core, focusing on the sulfate with a Raman peak at  $984\text{cm}^{-1}$  whose chemical form was not previously known [Ohno et al., 2006]. We will use a combination of micro-Raman spectroscopy and Differential Scanning Calorimetry (DSC) to clarify the phase equilibrium state of this sulfate.

### 5.2 Raman spectroscopy of microparticles in the ice core

#### *Raman spectra at constant temperature in the cryostat*

All the microparticles (total: 423 microparticles) were measured at  $-27.3\pm 0.2^\circ\text{C}$  from 15 ice samples in deep Dome Fuji ice core. We found several peaks in their Raman spectra, ranging from  $50$  to  $1250\text{cm}^{-1}$  [Figure 5.1a-o]. Figure 5.1h shows the spectrum of an ice sample without microparticles, with a peak at  $216.3\text{cm}^{-1}$  and a shoulder at  $312\text{cm}^{-1}$ . Spectra a-c come from sulfate salts whose presence in the ice had already been confirmed:  $\text{Na}_2\text{SO}_4\cdot 10\text{H}_2\text{O}$ ,  $\text{MgSO}_4\cdot 11\text{H}_2\text{O}$ , and  $\text{CaSO}_4\cdot 2\text{H}_2\text{O}$  [Ohno et al., 2005, chapter 2]. Spectrum d is the unidentified sulfate with a single S-O symmetric stretching mode at  $984\text{cm}^{-1}$ , previously reported by Ohno et al., 2006. Details on this spectrum are given in the discussion. Some microparticles (spectra e-g) yielded several sharp peaks but no evidence of sulfates. Each of these spectra comes from a single microparticle, which appear no different from the sulfate microparticles. The four large peaks in spectrum 1e correspond well with  $\text{NaAlSi}_3\text{O}_8$  (albite) [McKeown, 2005], the five peaks in spectrum 1f correspond well with  $\text{TiO}_2$  (Anatase) [Zhang et al., 2000], and the two peaks in figure 5.1g correspond well with  $\text{SiO}_2$  (quartz) [Jayaraman et al., 1987]. Still other microparticles produce mixed spectra (5.1i-o). These mixed particles could never be identified in a melted ice sample. (The result of mixed particles is relevant to the

refractive index of mixed aerosol [Liu and Daum, 2008], which is needed to reconstruct the role of radiative forcing during interglacial and glacial cycles.)

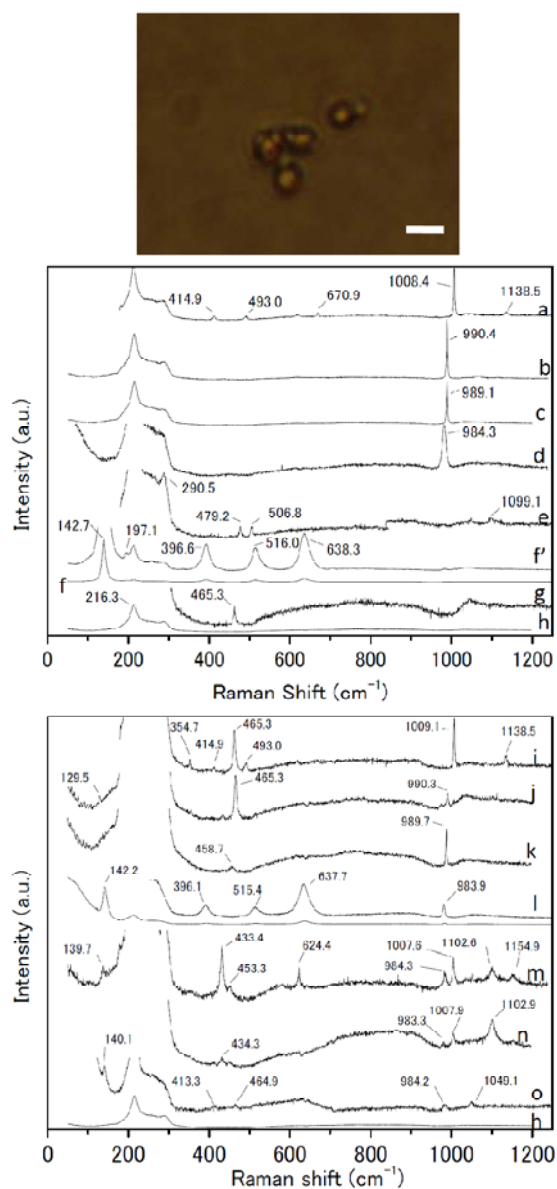


Figure 5.1. Microparticles in the Dome Fuji ice core (photo). The scale bar is 2  $\mu\text{m}$ . The Raman spectra of various microparticles are shown below the photo as curves a-o. Spectra (a-h) are  $\text{CaSO}_4 \cdot 2\text{H}_2\text{O}$ ,  $\text{MgSO}_4 \cdot 11\text{H}_2\text{O}$ ,  $\text{Na}_2\text{SO}_4 \cdot 10\text{H}_2\text{O}$ , an unidentified sulfate with a peak at  $984 \text{ cm}^{-1}$ ,  $\text{NaAlSi}_3\text{O}_8$  (albite),  $\text{TiO}_2$  (anatase),  $\text{SiO}_2$  (quartz), and ice respectively. Spectrum f' is a magnification of spectrum f. Curves (i-o) are the Raman spectra of various minerals mixed with sulfate salt. Spectrum (i) is a mixture of  $\text{SiO}_2$ ,  $\text{CaSO}_4 \cdot 2\text{H}_2\text{O}$ , and some other chemical with a peak at  $354.7 \text{ cm}^{-1}$ . Spectrum (j) is a mixture of  $\text{SiO}_2$  and  $\text{Na}_2\text{SO}_4 \cdot 10\text{H}_2\text{O}$ . Spectrum (k) is a mixture of  $\text{MgSO}_4 \cdot 11\text{H}_2\text{O}$  and other chemicals. Spectrum (l) is a mixture of sulfate (the peak at  $984.3 \text{ cm}^{-1}$ ) and  $\text{TiO}_2$ . Spectra (m) and (n) are both mixtures of several minerals, including  $\text{CaSO}_4 \cdot 2\text{H}_2\text{O}$  and the sulfate with a peak at  $984 \text{ cm}^{-1}$ . Spectrum (o) is mixture of the sulfate with a peak at  $984.2 \text{ cm}^{-1}$ ,  $\text{SiO}_2$ , and other chemicals. As these spectra show, sulfate salts can exist either independently or as a mixture with dust. Spectrum (h) is an ice.

Figure 5.2 shows the number of microparticles classified as each chemical form by comparing their Raman spectra with those of the reference specimens. The percentage of mixed microparticles (containing both sulfate and dust) does not significantly vary with depth.  $\text{CaSO}_4 \cdot 2\text{H}_2\text{O}$  is the most abundant chemical form in the periods of glacial maximum. These results are as expected, but an interesting anomaly appears when we consider the sulfates.

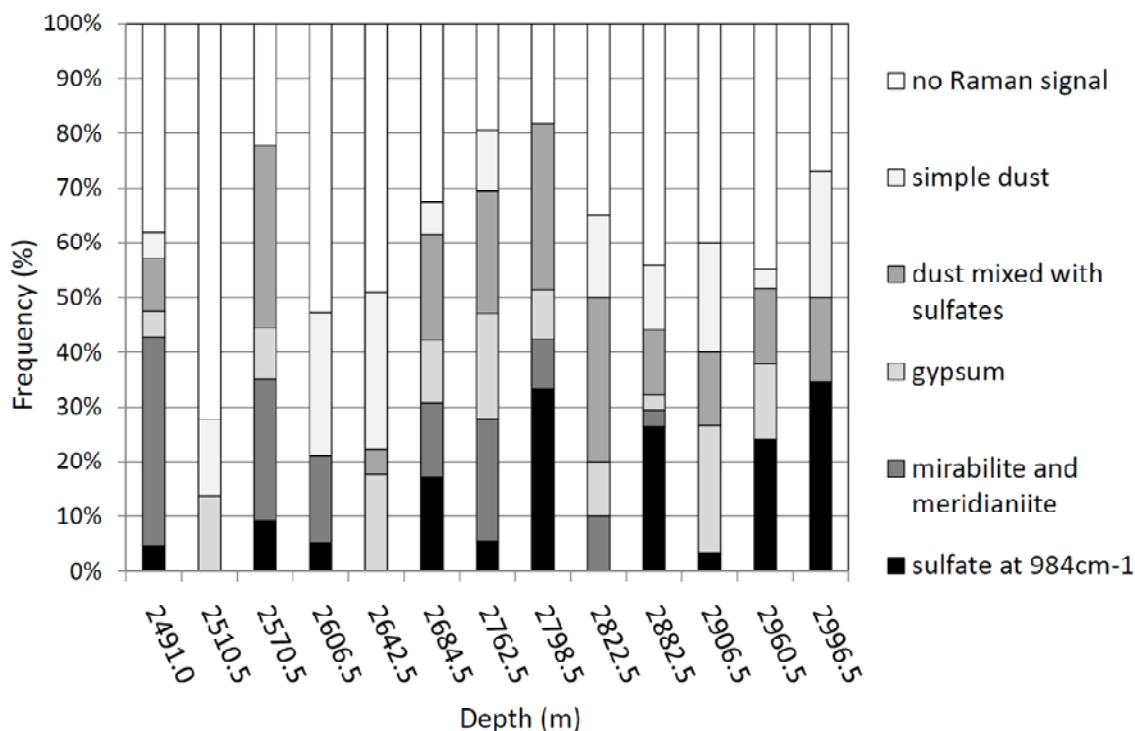


Figure 5.2. Distribution of microparticles classified into 6 types. “Sulfate at  $984\text{ cm}^{-1}$ ”, “mirabilite ( $\text{Na}_2\text{SO}_4 \cdot 10\text{H}_2\text{O}$ ) and/or meridianiite ( $\text{MgSO}_4 \cdot 11\text{H}_2\text{O}$ )”, and “gypsum ( $\text{CaSO}_4 \cdot 2\text{H}_2\text{O}$ )” are mainly distinguished by the position of the S-O symmetric stretching mode at  $984$ ,  $989$  ( $990$ ), or  $1008\text{ cm}^{-1}$  respectively. “Dust mixed with sulfates” refers to particles with Raman spectra similar to (i-o) in Figure 5.1. “Simple dust” particles have Raman spectra of pure dust such as (e-g) of Figure 5.1. Microparticles producing no spectral features other than those of ice are classified as “no Raman signal”.

In shallow interglacial periods (e.g.  $2491.0\text{ m}$ ),  $\text{Na}_2\text{SO}_4 \cdot 10\text{H}_2\text{O}$  and  $\text{MgSO}_4 \cdot 11\text{H}_2\text{O}$  are major chemical forms. In deep interglacial periods ( $2996.5\text{ m}$ ), however,  $\text{Na}_2\text{SO}_4 \cdot 10\text{H}_2\text{O}$  and  $\text{MgSO}_4 \cdot 11\text{H}_2\text{O}$  could not be found (Figure 5.2). The eutectic temperatures of these two sulfates ( $-1.3^\circ\text{C}$  and  $-3.7^\circ\text{C}$  respectively) are much higher than the temperature of the deepest of our samples ( $-4.2^\circ\text{C}$ , at  $2996.5\text{ m}$ ), suggesting that  $\text{Na}_2\text{SO}_4 \cdot 10\text{H}_2\text{O}$  and  $\text{MgSO}_4 \cdot 11\text{H}_2\text{O}$  should be present in deep ice. The unknown sulfate salt with an S-O symmetric stretching mode at  $984\text{ cm}^{-1}$  does become increasingly common with depth. This combination of results suggests that the sulfate at  $984\text{ cm}^{-1}$  is a key factor to understanding the presence or absence of  $\text{Na}^+$  and  $\text{SO}_4^{2-}$ .

### *The temperature dependence of Raman spectra for sulfate microparticles with a feature at 984 cm<sup>-1</sup>*

We actually found two types of sulfate with a Raman peak at 984 cm<sup>-1</sup>, with the measuring temperature at -27.3°C. One has a single peak, and the other has a split peak. The latter is rare in Dome Fuji ice core. To identify the sulfate with a single peak at 984 cm<sup>-1</sup>, we measured the temperature dependence of one such microparticle. In an ice sample from 2798.5 m, at the depth temperature is approximately -9.5°C [Hondoh et al., 2002]. Thus, we measured its Raman spectrum between 0 and 1250 cm<sup>-1</sup> while varying the cryostat temperature from -27.3±0.2 to -8.0±0.2°C. We observed that the shape of microparticle at -8.0°C was different from its shape at -27.3°C (Figures 5.3A, B). We also detected very low-frequency Raman features (around 5 cm<sup>-1</sup>) from the microparticle at -27.3°C (spectrum3 a), which were not present in the spectrum of pure ice at the same temperature (spectrum3 f). The new low-frequency features intensified somewhat with temperature, especially at -8.0°C (spectrum e), while the ice spectrum remained unchanged (spectrum g).

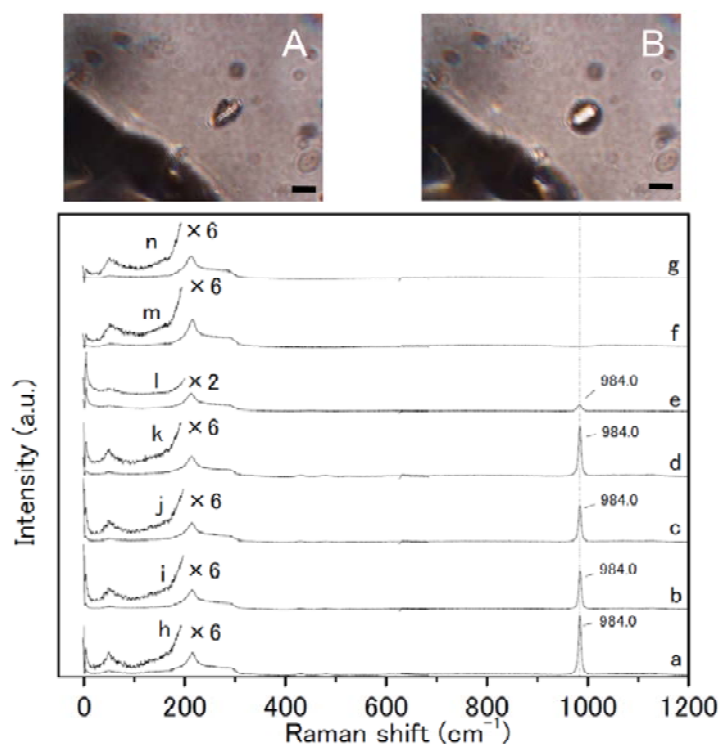


Figure 5.3. The temperature dependence of Raman spectra from a sulfate microparticle with a peak at 984 cm<sup>-1</sup> found in the ice core at a depth of 2798.5 m. The same particle is shown in photos A and B at temperatures of -27.3 and -8°C respectively. The black particles on the left side of these pictures are dissociated air hydrates. The scale bar is 10 μm. Spectra a, b, c, d and e were taken at -27.3, -25, -20, -15 and -8°C respectively. Spectra f and g are pure ice at -27.3, and -8.0°C, respectively.

We also measured a microparticle of the sulfate with a split peak at 984 cm<sup>-1</sup>. This type of particle is rare, but we found one in a sample of 2798.5 m ice. In a series of Raman spectra measured at -79.8±0.5°C, -27.3°C, and -8.0°C, we could see the splitting occur (Figure 5.4 a, b). At -27.3°C and -79.8°C (spectra a and b), the feature

can be decomposed into three lines at 983.6, 989.5, and 993.5  $\text{cm}^{-1}$ , suggesting a mixture of chemical forms (i.e.,  $\text{H}_2\text{SO}_4$ ,  $\text{Na}_2\text{SO}_4 \cdot 10\text{H}_2\text{O}$ , and probably anhydrous  $\text{Na}_2\text{SO}_4$ ). At  $-8.0^\circ\text{C}$ , the spectrum (c) shows single peak at  $984\text{cm}^{-1}$ . This result suggests that a phase transition occurs between  $-27.3^\circ\text{C}$  and  $-8.0^\circ\text{C}$ .

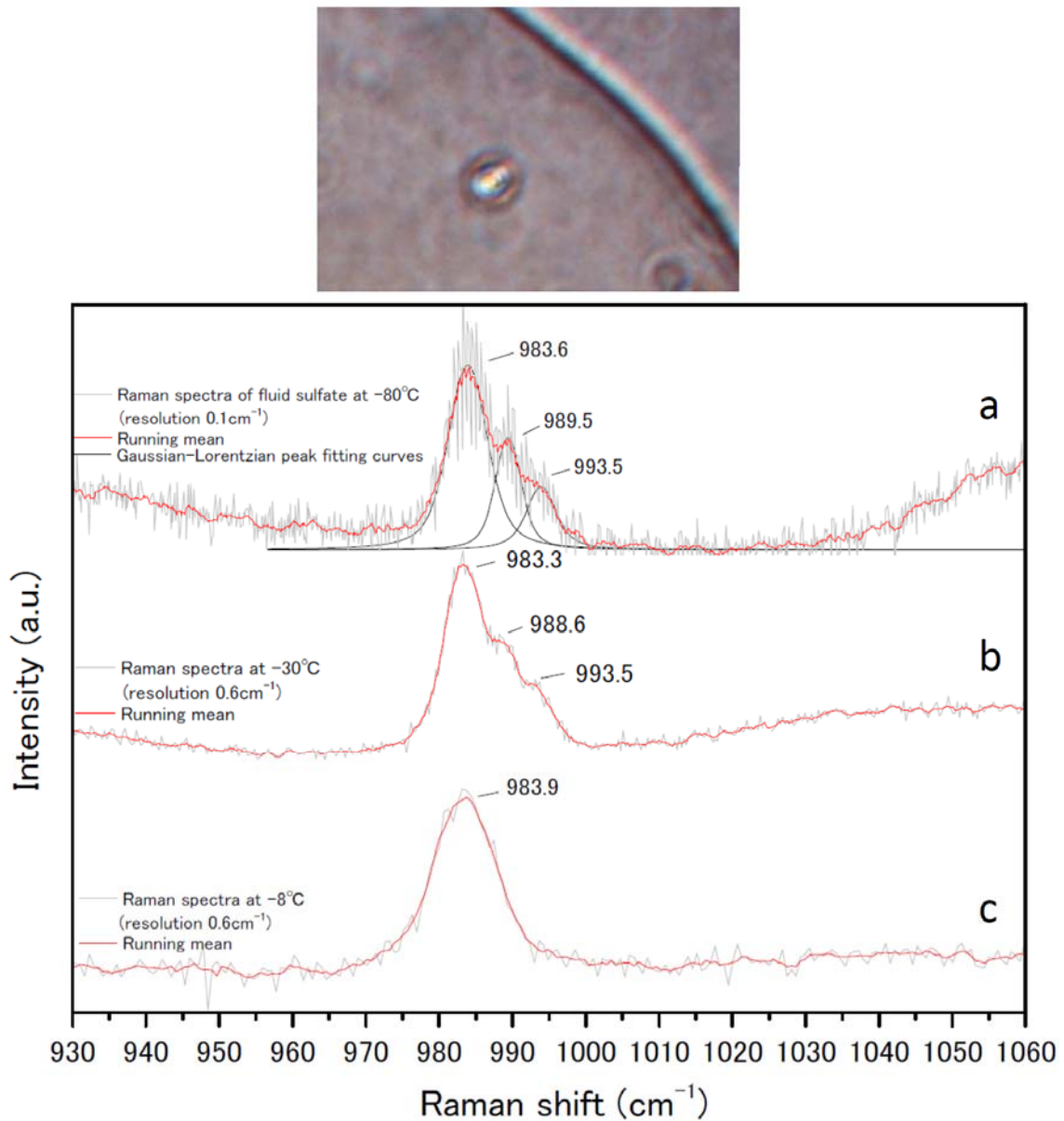


Figure 5.4. The photograph shows a  $7.3\mu\text{m}$ -diameter microparticle found at a depth of 2798.5 m at  $-8.0^\circ\text{C}$  when the photo was taken. Raman spectra a, b, and c of this particle were taken at  $-79.8^\circ\text{C}$ ,  $-27.3^\circ\text{C}$  and  $-8.0^\circ\text{C}$  respectively. The gray lines are the original Raman spectra ( $0.6\text{cm}^{-1}$  resolution for b and c,  $0.1\text{cm}^{-1}$  resolution for a). The red lines are ten-point running means. The black lines are Gaussian-Lorentzian fits calculated by the software (Origin Professional).

**Reference spectra of chemical forms with a feature at 984 cm<sup>-1</sup>.**

To identify the sulfate with a single 984 cm<sup>-1</sup> peak, we measured reference spectra for several chemical mixtures at the temperature of -27.3°C (Figure 5.5). We obtained peaks near 984 cm<sup>-1</sup> from the binary phase H<sub>2</sub>SO<sub>4</sub> · H<sub>2</sub>O, the ternary phase Na<sub>2</sub>SO<sub>4</sub> · HCl · H<sub>2</sub>O, and the ternary phase Na<sub>2</sub>SO<sub>4</sub> · H<sub>2</sub>SO<sub>4</sub> · H<sub>2</sub>O. The latter is a split peak with maxima at 984 cm<sup>-1</sup> and 989 cm<sup>-1</sup>. The ternary phase Na<sub>2</sub>SO<sub>4</sub> · NaCl · H<sub>2</sub>O (spectrum a) has a peak at 988.9 cm<sup>-1</sup>, too distant to be an acceptable match. Previous studies have mentioned that the hydrate of Na<sub>2</sub>SO<sub>4</sub> experiences a phase transition at high pressure (several GPa) [Oswald et al., 2008], but not the heptahydrate of Na<sub>2</sub>SO<sub>4</sub> [Figure 5.6]. We also found the sulfate at 984cm<sup>-1</sup> from EDML ice core from shallow depth (539.9m) which is Holocene ice [Unpublished data]. This result also suggests that the sulfate at 984cm<sup>-1</sup> is not related to the pressure but the temperature of ice. This finding was significantly important to realize the phase state and chemical form of the sulfate at 984cm<sup>-1</sup>. Further study on the characteristics of water-soluble microparticles in EDML ice core is being undertaken.

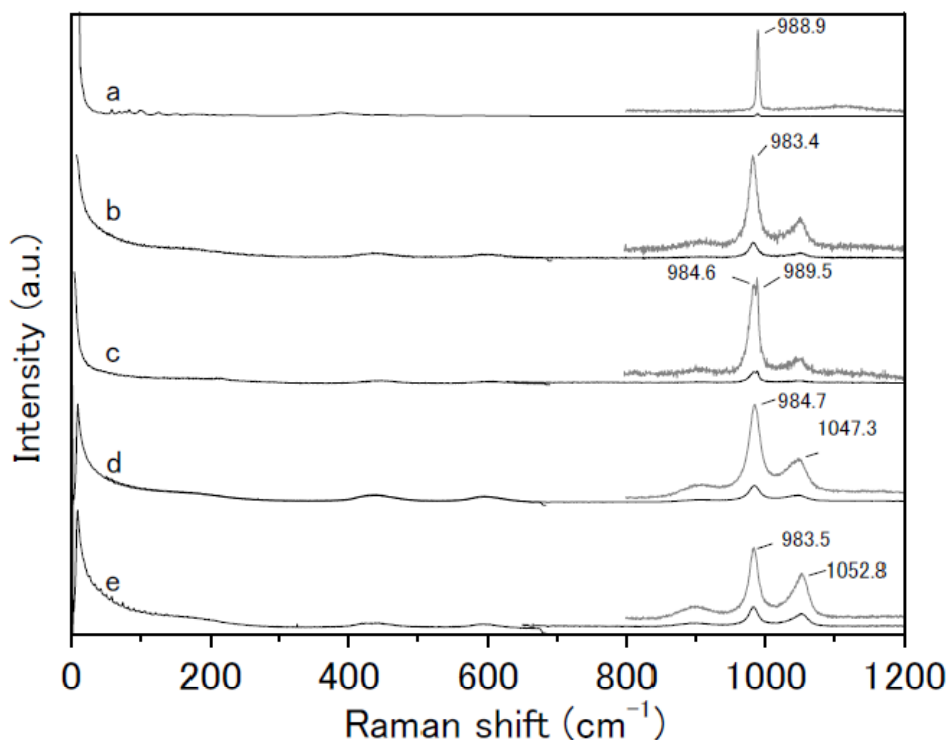


Figure 5.5. Raman spectra of various sulfate solutions with peaks near 984 cm<sup>-1</sup>. From top to bottom, the chemical forms and temperatures are (a) Na<sub>2</sub>SO<sub>4</sub> (2.1wt%) · NaCl (12wt%) · H<sub>2</sub>O at -27.3°C, (b) Na<sub>2</sub>SO<sub>4</sub> (2.1wt%) · H<sub>2</sub>SO<sub>4</sub> (16.0wt%) · H<sub>2</sub>O at -12.7°C, (c) Na<sub>2</sub>SO<sub>4</sub> (2.1wt%) · H<sub>2</sub>SO<sub>4</sub> (16.0wt%) · H<sub>2</sub>O at -27.3°C, (d) H<sub>2</sub>SO<sub>4</sub> (16.0wt%) · H<sub>2</sub>O at -27.3°C, and (e) Na<sub>2</sub>SO<sub>4</sub> (2.1wt%) · HCl (2.1wt%) · H<sub>2</sub>O at -27.3°C. The gray spectra are magnifications from 800 to 1200cm<sup>-1</sup>.

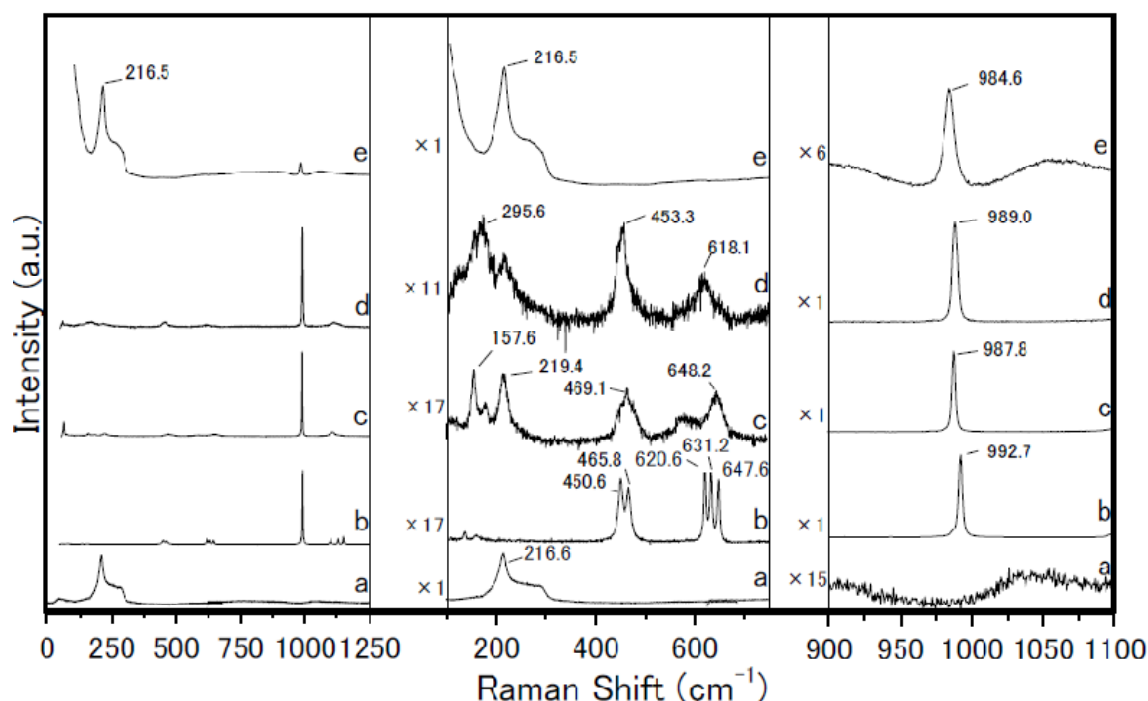


Figure 5.6. The Raman spectra of reference specimens and the sulfate with a peak at  $984\text{ cm}^{-1}$ . (a) ice, (b)  $\text{Na}_2\text{SO}_4$ , (c)  $\text{Na}_2\text{SO}_4 \cdot 7\text{H}_2\text{O}$ , (d)  $\text{Na}_2\text{SO}_4 \cdot 10\text{H}_2\text{O}$ , (e) the unidentified sulfate from the Dome Fuji ice core. Specimens (c) and (d) are eutectic concentrations of  $\text{Na}_2\text{SO}_4 \cdot \text{H}_2\text{O}$ . The center and right columns are magnifications of the spectra.

The binary phase  $\text{H}_2\text{SO}_4 \cdot \text{H}_2\text{O}$  at  $-27.3^\circ\text{C}$  can be recognized as a liquid phase from the shape of its low-frequency Raman spectrum around  $5\text{ cm}^{-1}$  (Figure 5.3a-e), which can be interpreted as the superposition of one Debye-type relaxation mode and two damped harmonic oscillators [Mizoguchi et al., 1992]. In addition, the binary phase diagram of  $\text{H}_2\text{SO}_4 \cdot \text{H}_2\text{O}$  confirms that the solution must be liquid at temperatures below  $-27.3^\circ\text{C}$  [Beyer et al., 2003]. Likewise, spectrum (Figure 5.4b) reveals the liquid phase of  $\text{Na}_2\text{SO}_4 \cdot \text{H}_2\text{SO}_4 \cdot \text{H}_2\text{O}$  at  $-27.3^\circ\text{C}$  in addition to  $\text{Na}_2\text{SO}_4 \cdot 10\text{H}_2\text{O}$  (the  $989\text{ cm}^{-1}$  peak). According to the ternary phase diagram of  $\text{Na}_2\text{SO}_4 \cdot \text{H}_2\text{SO}_4 \cdot \text{H}_2\text{O}$ , the liquid and solid ( $\text{Na}_2\text{SO}_4 \cdot 10\text{H}_2\text{O}$ ) phases should coexist at  $-27.3^\circ\text{C}$ . The high molality of  $\text{H}_2\text{SO}_4$  might be expected to change the phases into  $\text{Na}_3\text{H}(\text{SO}_4)_2$  and  $\text{NaHSO}_4 \cdot \text{H}_2\text{O}$  [Marion et al., 2002]. However, the Raman spectra of  $\text{Na}_3\text{H}(\text{SO}_4)_2$  [Videnova-Adrabinska, 1990] and  $\text{NaHSO}_4 \cdot \text{H}_2\text{O}$  do not have the S-O symmetric stretching mode at  $984\text{ cm}^{-1}$  (Section 2.3). The ternary phase  $\text{Na}_2\text{SO}_4 \cdot \text{HCl} \cdot \text{H}_2\text{O}$  can be recognized as a liquid (spectrum e), but little is known about its phase diagram. This is the most likely combination to form from the ions of chemical form of sulfate at  $984\text{ cm}^{-1}$  in ice cores due containing  $\text{Na}^+$ ,  $\text{SO}_4^{2-}$ , and  $\text{Cl}^-$  in ice.

### 5.3 Ternary phase diagram of $\text{Na}_2\text{SO}_4$ - $\text{HCl}$ - $\text{H}_2\text{O}$

Solutions of  $\text{Na}_2\text{SO}_4$  -  $\text{HCl}$  -  $\text{H}_2\text{O}$  were prepared with ultrapure water (18.3 m $\Omega$ ) by diluting 35-37wt%, reagent-grade  $\text{HCl}$  (Kanto Chemical co.) and 99.5wt%, reagent-grade, anhydrous  $\text{Na}_2\text{SO}_4$  (Kishida Chemical co.). First a solution of  $\text{Na}_2\text{SO}_4$  -  $\text{H}_2\text{O}$  is prepared with 8.6wt%, and then a solution of  $\text{HCl}$  -  $\text{H}_2\text{O}$  is added until the eutectic concentration of  $\text{Na}_2\text{SO}_4$  -  $\text{H}_2\text{O}$  such as 4.3wt% [Usdowski and Dietzel, 1998] decreases to the desired value. A typical sample was cooled to  $-120^\circ\text{C}$  at  $10^\circ\text{C}/\text{min}$ , and then warmed to  $25^\circ\text{C}$ . Warming took place at either  $10^\circ\text{C}/\text{min}$  or  $1^\circ\text{C}/\text{min}$ , for the open Pt pan and sealed Au pan respectively. Supercooled solution of liquid with  $\text{HCl}$  -  $\text{H}_2\text{O}$  below  $-123^\circ\text{C}$  is recognized previously [Abbatt et al., 1992]. Thus, we put a piece of gold in the sample pan (and standard pan) to set off the crystallization of the solutions. Using these procedures, we constructed the ternary phase diagram of  $\text{Na}_2\text{SO}_4$  -  $\text{HCl}$  -  $\text{H}_2\text{O}$  (Figure 5.7a). We performed measurements in the  $\text{HCl}$  composition range 0 to 17wt%. At compositions of 17 wt% or higher, our measurements were not easily reproducible. The labeled regions were identified by Raman spectroscopy. The melting temperature of  $\text{Na}_2\text{SO}_4 \cdot 10\text{H}_2\text{O}$  decreases as the concentration of  $\text{HCl}$  increases. The eutectic transition temperature of  $\text{NaCl} \cdot n\text{H}_2\text{O}$  is  $-42.7 \pm 0.4^\circ\text{C}$ . Hydrated  $\text{NaCl}$  appears when the  $\text{HCl}$  composition is approximately 2.1wt% or greater. This threshold is a bit higher than the molar equilibrium of  $\text{SO}_4^{2-}$  and  $\text{Cl}^-$ . The enthalpy of total fusion for this phase diagram is shown in Figure 5.7b. At an  $\text{HCl}$  concentration of about 10.5wt% we reach the enthalpy minimum, where the composition is thermodynamically stable (phase equilibrium state).

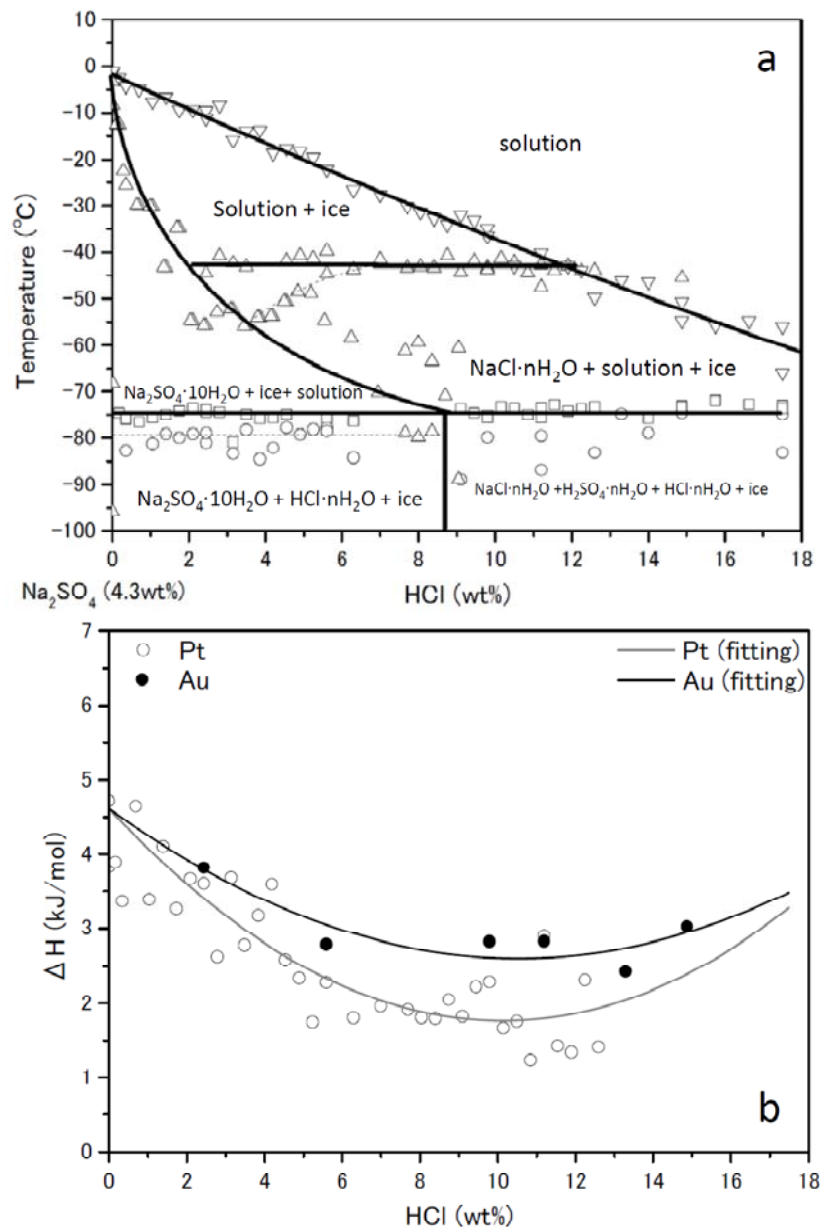


Figure 5.7. (a) Ternary phase diagram of Na<sub>2</sub>SO<sub>4</sub> - HCl - H<sub>2</sub>O. At low HCl concentrations, HCl·nH<sub>2</sub>O metastable line can be seen at  $-79.7 \pm 4.0^\circ\text{C}$  and there is a stable line at  $-73.6 \pm 1.9^\circ\text{C}$ . At high HCl concentrations, NaCl appears from close to the molar equilibrium (2.1 wt %) of Cl<sup>-</sup> and SO<sub>4</sub><sup>2-</sup>. The eutectic temperature of this transition is  $-42.7 \pm 1.7^\circ\text{C}$ . The phase transition to “NaCl·nH<sub>2</sub>O + solution + ice” and “solution + ice” from “Na<sub>2</sub>SO<sub>4</sub>·10H<sub>2</sub>O + solution + ice” is a glass transition. The regions are determined by Raman spectroscopy of samples at the temperatures and concentrations indicated by triangles. The hydration numbers are therefore not known, except for Na<sub>2</sub>SO<sub>4</sub>·10H<sub>2</sub>O. (b) Thermal equilibrium compositions measured by DSC, in both a sealed Au pan and an open Pt pan. The open pan shows less latent heat because some HCl evaporated during the measurement. The enthalpy decreases with HCl concentration up to about 10.5wt%, and then increases again.

## 5.4 Chemical form of the sulfate microparticles with Raman peak at $984\text{ cm}^{-1}$

We examined several reference spectra of binary and ternary phases containing  $\text{SO}_4^{2-}$ ,  $\text{Na}^+$ , and  $\text{H}_2\text{O}$  to identify the sulfate microparticles with a Raman peak at  $984\text{ cm}^{-1}$ . The reference spectra and phase diagrams of all candidate compositions agree on this point: the microparticles with a Raman peak at  $984\text{ cm}^{-1}$  must exist as liquid sulfate in the ice core.

There are two types of plausible chemical forms for a liquid sulfate, the ternary phases  $\text{Na}_2\text{SO}_4 \cdot \text{HCl} \cdot \text{H}_2\text{O}$  at the different concentration of HCl. One is higher concentration of HCl than molar equilibrium of  $\text{Cl}^-$  and  $\text{SO}_4^{2-}$  [Figure 5.3], and the other is much lower than molar equilibrium of  $\text{Cl}^-$  and  $\text{SO}_4^{2-}$  which is rare in deep Dome Fuji ice [Figure 5.4]. Thus, we insist that the most of the sulfate microparticles with a Raman peak at  $984\text{ cm}^{-1}$  consist of  $\text{Na}_2\text{SO}_4 \cdot \text{HCl} \cdot \text{H}_2\text{O}$  with high HCl concentrated. The phase diagram of  $\text{Na}_2\text{SO}_4 \cdot \text{HCl} \cdot \text{H}_2\text{O}$  [Figure 5.7a] in the region of HCl concentrations higher than the molar equilibrium of  $\text{Cl}^-$  and  $\text{SO}_4^{2-}$  shows that the eutectic temperature is  $-42.7^\circ\text{C}$ , and that the phase transition from  $\text{Na}_2\text{SO}_4 \cdot 10\text{H}_2\text{O}$  to liquid sulfate and/or  $\text{NaCl} \cdot n\text{H}_2\text{O}$  is a function of both temperature and HCl concentration. The pressure melting point of 2.1wt% of HCl, for instance, can be calculated from Calusius-Clapeyron equation, and the parameters are enthalpy fusion, density of liquid (solution measured) and solid ( $\text{NaCl} \cdot 2\text{H}_2\text{O}$ ), and the temperature at  $-42.7^\circ\text{C}$  and the result gives  $dT/dp = 4 \times 10^{-2}\text{ K/bar}$ . Thus, melting temperature increases  $5.3^\circ\text{C}$ , then melting temperature of  $\text{Na}_2\text{SO}_4 \cdot \text{HCl} \cdot \text{H}_2\text{O}$  at the composition of 2.1wt% of HCl is  $-37.4^\circ\text{C}$  which the depth approximately 1500m. In fact, the shallowest depth at which Ohno et al. [2006] found these sulfate particles was 1746m, where the ice temperature is approximately  $-32.7^\circ\text{C}$ . Their finding is very reasonable. Fukazawa et al. [1998] also found sulfate particles with a Raman peak at  $980\text{ cm}^{-1}$  on the grain boundary of the Nansen and South Yamato ice cores, taken from a coastal site in Antarctica. This finding is also reasonable in light of our phase diagram for  $\text{Na}_2\text{SO}_4 \cdot \text{HCl} \cdot \text{H}_2\text{O}$ , because the surface temperature of Nansen and South Yamato ice core sites are  $-42^\circ\text{C}$  and  $-36^\circ\text{C}$ , respectively, and their measuring temperature is  $-20^\circ\text{C}$ , which is much higher than the eutectic temperature of  $\text{Na}_2\text{SO}_4 \cdot \text{HCl} \cdot \text{H}_2\text{O}$ .

## 5.5 The implications of finding liquid sulfate in the ice sheet

To determine whether liquid exists along the grain boundary or as a microparticle, it is necessary to understand the relationship between the two interface energies balance:

$$\gamma_{gb} = 2\gamma_{sl}\cos\theta , \quad (5.1)$$

for a liquid fusiform-shaped particle with a vertex angle  $2\theta$ ,

$$\gamma_{gb} > 2\gamma_{sl} , \quad (5.2)$$

for a liquid film along the grain boundary, where  $\gamma_{gb}$  is the grain boundary energy and  $\gamma_{sl}$  is the surface energy of the liquid-ice interface [Nye and Mae, 1972]. According to a previous study [Fletcher, 1970],  $\gamma_{sl}$  is  $22\text{mJ/m}^2$  and  $\gamma_{gb}$  is  $60\text{mJ/m}^2$ ; the former being less than half of the latter, it can be concluded that the water should be distributed along the grain boundary. As mentioned earlier, this process may disturb climate signals [Rempel et al., 2001, 2002]. If the water-ice interface energy is greater ( $31.7\pm 2.7\text{ mJ/m}^2$ ) [Hillig, et al., 1997] than half of the grain boundary energy ( $60\text{mJ/m}^2$ ), on the other hand, the water should not diffuse along the grain boundary. Moreover, the grain boundary energy tends to decrease for ice grains arranged in a high-density coincidence site lattice [Hondoh and Higashi, 1978, 1979, Higashi, 1978], as is often the case in deep ice [Paterson, 1994]. Therefore, this effect plays an important role in the shaping of liquid sulfate, especially in deep ice.

In order to reconstruct a reliable past climate history from the ion concentrations observed in ice cores, we have to know whether the ions are present in liquid or solid form in addition to identifying their chemical forms. Previous studies have suggested that liquid compounds may exist on the grain boundaries [Mulvaney et al., 1988, Fukazawa et al., 1998] but never confirmed their chemical form. This research has unambiguously identified liquid microparticles containing sulfate, sodium, chloride and acid. To understand why the liquid sulfate exists as disconnected microparticles rather than diffusing along the vein network, we have to take into account the wettability of the ice. The spreading coefficient  $S$  can be expressed as

$$S = \gamma_{gb} - 2\gamma_{sl}\cos\theta , \quad (5.3)$$

but  $S$  also relates to the ion polarizabilities. This relation is approximately expressed as

$$S = k(\alpha_s - \alpha_l)\alpha_l , \quad (5.4)$$

where  $\alpha_s$  and  $\alpha_l$  are the ion polarizabilities of solid ice and liquid sulfate respectively, and

$k$  is a constant [de Gennes, 1985]. When  $S$  is positive, the liquid sulfate should diffuse along the grain boundary; when  $S$  is negative, the liquid should form a particle. In the case of a liquid containing several ions such as sulfate, sodium, chloride and acid, the latter case should hold because the polarizability of liquid sulfate is higher than that of solid ice.

Thus, while it is possible in principle for sulfate ions to occupy grain boundaries and disturb climate signals by diffusing through the network, according to our measurements the necessary conditions are not present in the core. Thus, we insist that most of sulfate ions exist as microparticles, especially in deep ice.

To summarize the above analysis, liquid sulfate should exist as microparticles if 1) the liquid-ice surface energy is greater than half of the grain boundary energy, and 2) the polarizability of the sulfate ions is greater than that of the ice. In addition, the grain boundary energy tends to decrease for ice grains arranged in a high-density coincidence site lattice especially in deep ice and thus favors the first condition. As both conditions hold in the core, we claim that liquid sulfate is not present in the vein network and therefore the ions ( $\text{Na}^+$ ,  $\text{SO}_4^{2-}$ ,  $\text{Cl}^-$ ) can serve as dependable proxies of past climate even in deep ice cores.

The existence of liquid sulfate is also important when considering the electrical conductivity of ice cores. In fact, experiments have shown that both dielectric and electrical conductivity are higher in interglacial ice than in glacial ice [Fujita et al., 2002; EPICA member, 2004]. This difference can be attributed to the distribution of HCl, and implies that HCl actually substitutes for  $\text{H}_2\text{O}$  molecules in the lattice (i.e., the ice crystals are doped with HCl). Thus, we speculate that the  $\text{Cl}^-$  (HCl) concentration controls the electrical conductivity while the amount of liquid sulfate controls the dielectric profile. Finding liquid sulfate in a polar ice core not only explains the existence of ions, but also provides a reasonable interpretation of electrical conductivity measurements. In addition, the dielectric properties of doped HCl ice are well known by previously [Takei et al., 1997]. According to their data, the dielectric properties change with the frequency (Hz) from pure ice. Therefore, we insist on that the existence of doped HCl can be detected by dielectric measurement by several hundred Hz from ice core on further measurement.

Lu et al. [2009] show that the effective diffusion coefficient of  $\text{D}_2\text{O}$  is  $2\pm 1\times 10^{-4}$  mol fraction of HCl (much high order of Antarctic ice) doped in ice are related to the temperature dependent. According to their data, the diffusion coefficient of  $\text{D}_2\text{O}$  in ice is one order of magnitude lower than the level of HCl doping with the order of  $10^{-10}\text{m}^2/\text{s}$ .

We assume that the diffusion coefficient of HCl is approximately equal to that of D<sub>2</sub>O. The maximum distance of HCl diffusion (several meters) suggests that Cl<sup>-</sup> and D<sub>2</sub>O can be mixing and lost the climate signals but our result of phase diagram of Na<sub>2</sub>SO<sub>4</sub> - HCl - H<sub>2</sub>O suggest that the Cl<sup>-</sup> (HCl) should be aggregated to the Na<sub>2</sub>SO<sub>4</sub> to form liquid sulfate. Therefore, Cl<sup>-</sup> (HCl) diffusion may inhibit by the microparticles and the behavior of Cl<sup>-</sup> (HCl) should take place with SO<sub>4</sub><sup>2-</sup> in equilibrium states in ice.



# Chapter 6

## Spatial distribution of microparticles in Dome Fuji ice core

### 6.1 Purpose

Particularly focused on the grain growth of ice and the effect of impurities in ice, “a numerical model” provides evidence for the fact that the existence of dust dominantly affects the grain growth kinetics [Durand et al., 2006]. In order to reconstruct the past climate histories from these impurities, we have to clarify where these impurities existed and how the minimum resolution required for analyzing the ice cores is suitable for the reliable proxies. In this study, we have measured the size, number concentration, and the spatial distribution of microparticles in the deep part of the Dome Fuji ice core in order to clarify the existence of microparticles by “measurement”.

### 6.2 The diameter and the number concentration of microparticles

Figure 6.1 shows the mean diameter of the microparticles. The diameter of the microparticles at a shallow depth was approximately  $2.0 \pm 0.3 \mu\text{m}$ , but in the deep part of the ice core, the average diameter increased with an increase in depth. With respect to the size variability of the diameter of the microparticles, the percentage of microparticles with a diameter of more than  $3 \mu\text{m}$  in each depth is shown in Figure 6.2 and with respect to their age is shown in Figure 6.3. The percentage of microparticles with an anomalous diameter of more than  $3 \mu\text{m}$  is different for different climate stages. In the interglacial periods of ice, the number ratio of microparticles with a diameter of more than  $2.5 \mu\text{m}$  gradually increased with an increase in depth, but in the glacial

maximum periods of ice, it increased drastically after the depth of 2822.5 m. This result can be explained on the basis of the fact that liquid sulfate as microparticles is coarse because of the aggregation of HCl into the sulfate salts that are dominant in the interglacial periods in deep ice [Chapter 4]. On the other hand, the drastic increase in the diameter after the depth of 2822.5 m in the glacial maximum period was probably due to the aggregation of the microparticles brought about by the grain boundary migrations.

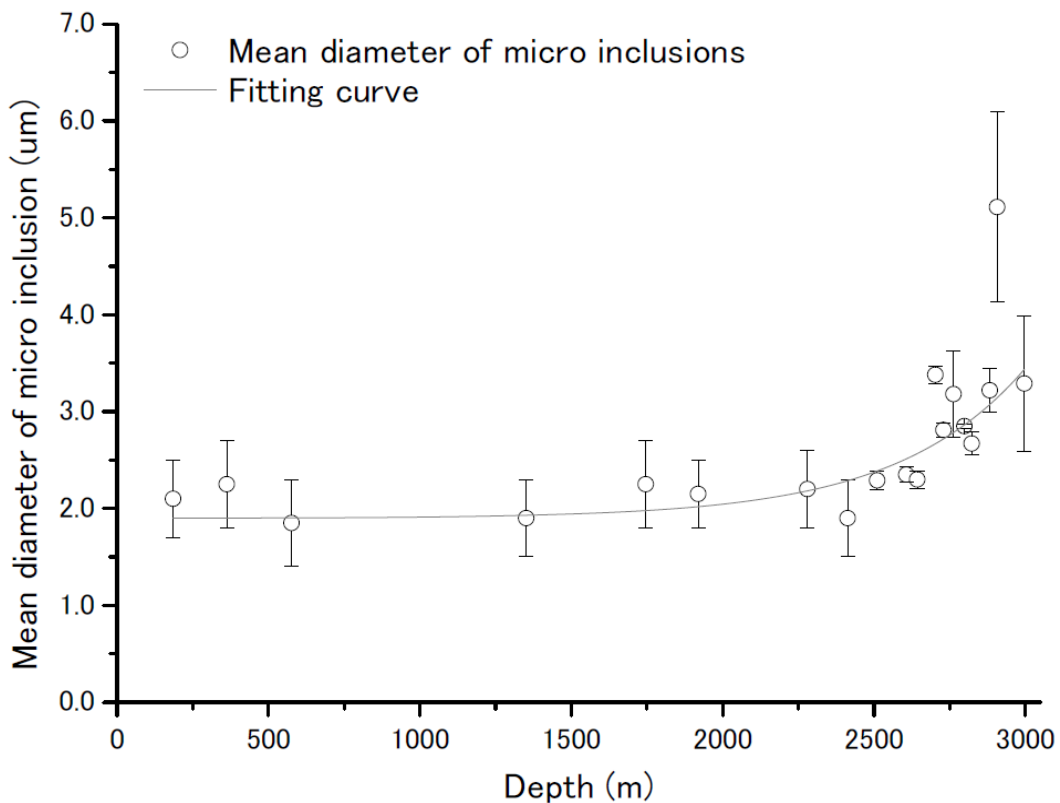


Figure 6.1 Mean diameter of microparticles. The error bar is one sigma and the line is fitting curve by exponential factor, calculated by Origin.Pro.7.5.

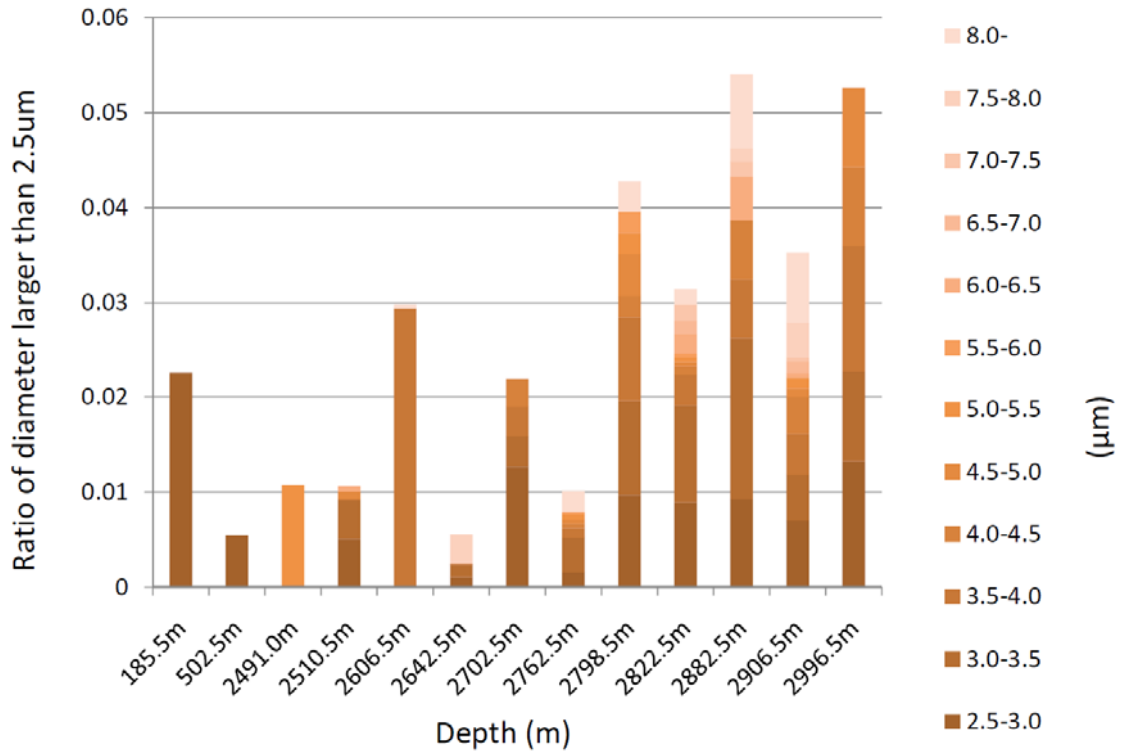


Figure 6.2. The distribution of anomalous large microparticles in respective depth.

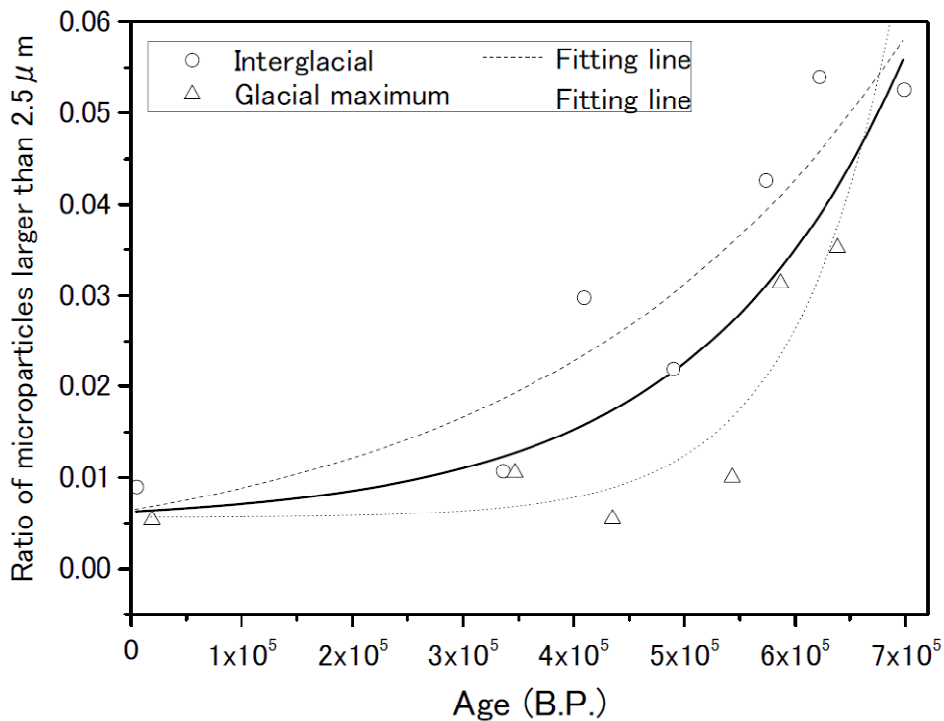


Figure 6.3. The ratio of microparticles larger than 2.5µm. The best fitting lines are total (solid line):  $y = 0.0012e^{\left(\frac{x}{185062}\right)} + 0.0051$ , interglacial (bloken line):  $y = 0.0065e^{\left(\frac{x}{319033.15}\right)} + 0.002$ , and glacial maximum (dashed line):  $y = 2 \times 10^{-5}e^{\left(\frac{x}{99116}\right)} + 0.006$ , calculated by Origin pro. 7.5.

The number concentration is calculated by the number of microparticles and the volume of the 100 sites with dimensions of  $1.8\text{mm} \times 1.4\text{mm} \times \text{ice thickness mm}^3$ . The number of microparticles having a spatial distribution in the grains and around the grain boundaries is compared. At a shallow depth, the number concentration of the microparticles around a grain boundary at the depths of 185.5 and 502.5 m is  $4.2 (\pm 0.7) \times 10^4$  and  $3.6 (\pm 0.4) \times 10^5$  ( $\text{mL}^{-1}$ ), respectively, and in the grain at the same depths of 185.5 and 502.5 m is  $3.5 (\pm 0.4) \times 10^4$  and  $3.1 (\pm 0.3) \times 10^5$ , respectively. These results show comparable such means that the almost same result can be obtained from the grain and around grain boundary at the shallower depth. Therefore, we measured the spatial distribution in the grain and calculated the number concentration of the microparticles in the deep part of the ice core (Figure 6.4). The result shows that the number concentration of the microparticles tends to decrease with an increase in the depth. However, focusing on the regional sight, we observed that some of the microparticles aggregated strongly in the deep ice (Figure 6.5). Therefore, in order to clarify the trend of the decrease in the number concentration of microparticles in a deep part and the aggregation of the microparticles, the spatial distribution of microparticles is now necessary to understand the existence of microparticles in deep ice.

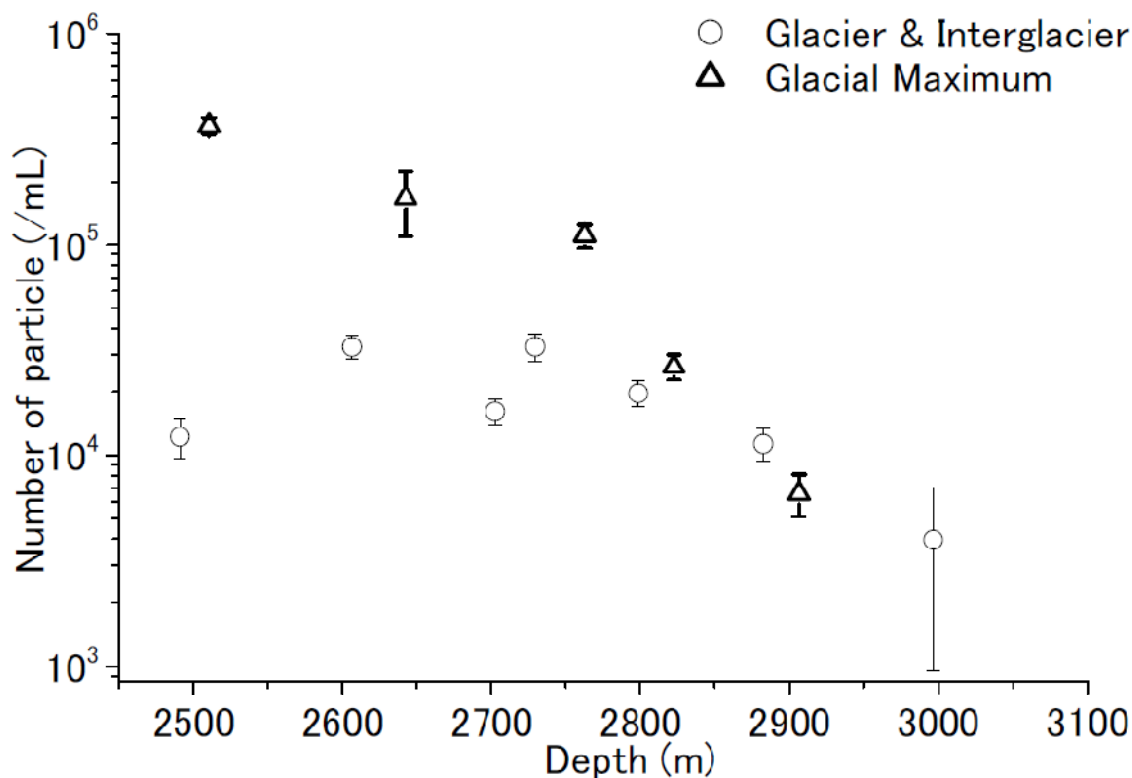


Figure 6.4 Number of concentration of microparticles in ice grain.

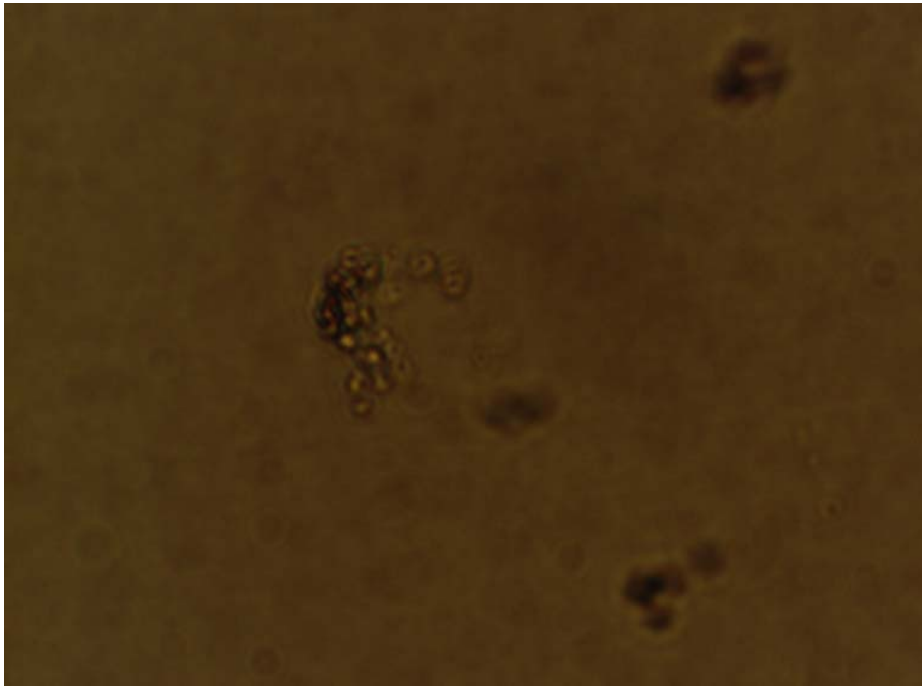
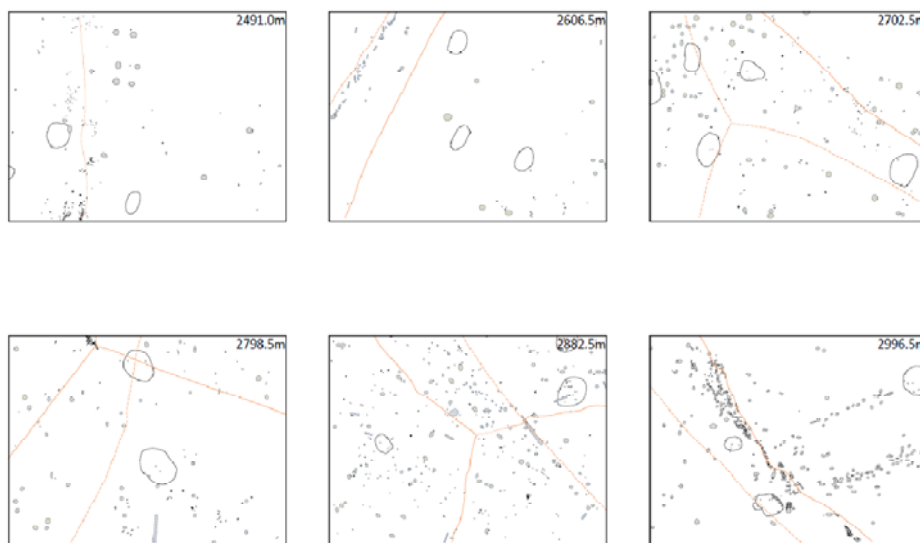


Figure 6.5 The picture of optical microscope in 2822.5m. Distribution of microparticles is partly aggregated in deep ice. The scale of this picture is 0.18×0.14 (mm).

### 6.3 Spatial distribution of microparticles

The microparticles are distributed either as clusters or individual particles; however, we could not clearly establish the relation between the grain boundary and the microparticles at a shallow depth of 502.5 m. [Figure 6.6](#) shows that the spatial distribution of the microparticles in the deep part of the Dome Fuji ice core along with the respective climate stages. In this part of the Dome Fuji ice core, the aggregation of microparticles is significant, and a large number of microparticles are distributed as a string of several micrometers; the longest string is more than 100 micrometers, but each microparticle is isolated (disconnected). Therefore, the number of microparticles around an ice grain boundary is larger than that in an ice grain ([Figure 6.7](#)). This result shows that the decrease in the number concentration of the microparticles in the ice grain is remarkable both in the case of the interglacial period and the glacial maximum; however, the number concentration of the microparticles around the grain boundary in both the interglacial period and the glacial maximum is almost constant. In other words, the number of concentration decrease in the ice grain seems to be increasing the number around grain boundary but the particles coarsening. The coarsening of microparticles should explain of the discrepancy.

a); interglacial and glacial periods (2491.0, 2606.5, 2702.5, 2798.5, 2882.5, 2996.5m, respectively).



b); glacial maximum periods (2510.5, 2642.5, 2762.5, 2822.5a, 2822.5b, 2906.5m, respectively).

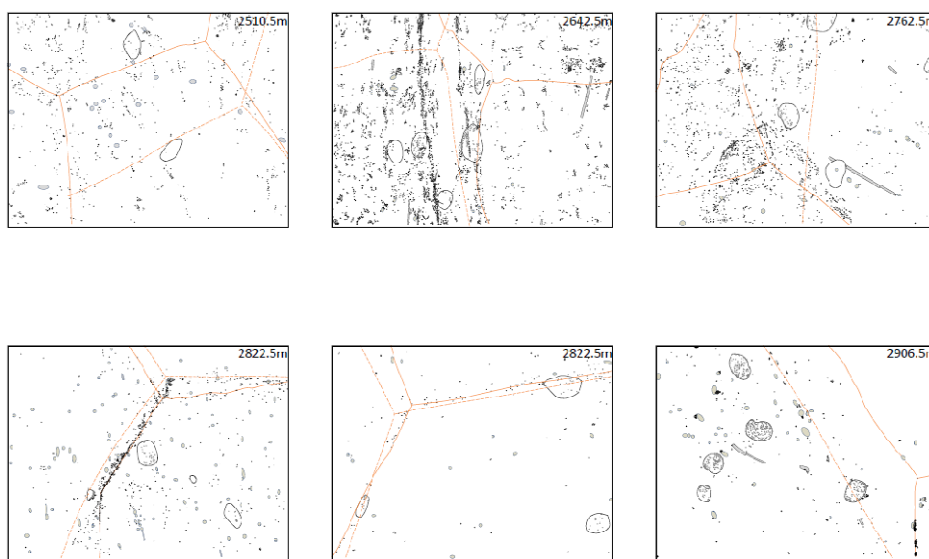


Figure 6.6 Spatial distribution of microparticles. a); interglacial and glacial period of ice, b); glacial maximum of ice. Black dots: microparticles, white circle: air hydrate, line: grain boundary at top, broken line: grain boundary at bottom, black circle: air bobble.

We also measured two sites at the depth of 2822.5 m in order to clarify the variability of the number concentration in the ice section; these sites were only 1 cm apart in the direction of the core depth (Figure 6.6b). The number of microparticles in these sites was 218 and 733, respectively (Table 6.1). This result shows that the microparticles were inhomogeneously distributed in the ice. If the diffusion of the

water-soluble microparticles took place in the ice through a connected vein network, then the distribution of the microparticles should be the same in both these close sites. Therefore, we can inform that the microparticles as proxies of climate signals can be preserved even in a few centimeters of ice. On the other hand, by focusing on the distribution of microparticles in ice with respect to the grain boundary, we counted the number of microparticles within the grain boundary in the site shown in Figure 6.6. The number concentration of the microparticles within the grain boundary increased after the depth of 2798.5 m, as shown in Figure 6.8. In this case, the distribution of the microparticles aggregated on the grain boundary drastically increased after the depth of 2798.5 m, but at the depths of 2960.5 and 2996.5 m, the number concentration of the microparticles within the grain boundary decreased because the distribution of microparticles was dominant on the air hydrates at these depths.

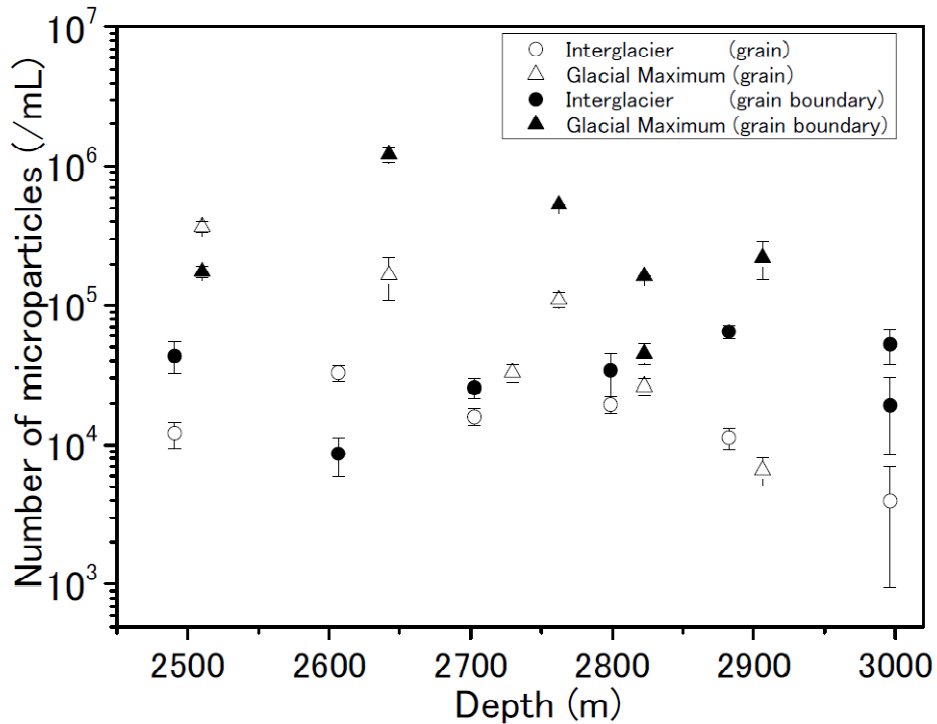


Figure 6.7 The number concentration of microparticles in ice grain and around ice grain boundary.

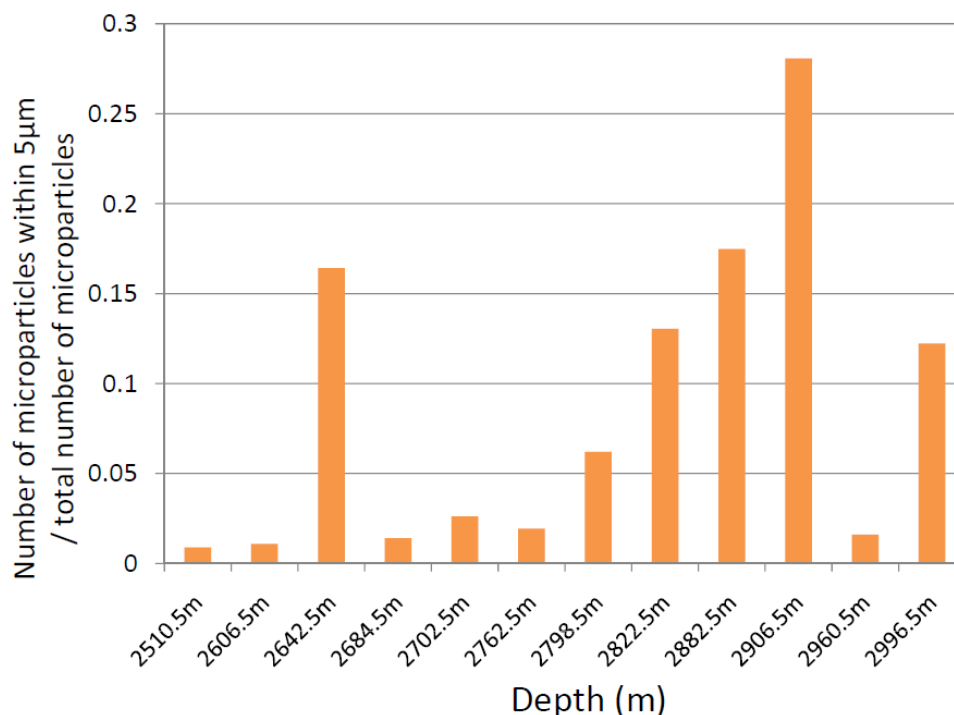


Figure 6.8 Number of microparticles, within grain boundary, calculated from Figure 6.6.

We found that the some microparticles are partly aggregated not always to the grain boundary but related to the existence on the air hydrates, especially deep part. The ratio of the microparticles on the air hydrates was calculated, and the result showed that the number of microparticles on the air hydrates increased with an increase in the depth (Figure 6.9). In other words, microparticles are strongly aggregated especially on the air hydrates. This result tells us that the air hydrate plays an important role as a storage site of microparticles.

These results of the distribution of microparticles are especially important for a discussion on the minimum resolution depth profiles of the microparticles as dependable proxies of the past climate histories. On the basis of these evidences, we can definitely confirm that in order to measure the minimum resolution depth of the microparticles as a dependable proxy of the past climate histories, we have to follow the grain size and distribution of air hydrates which needed for further study.

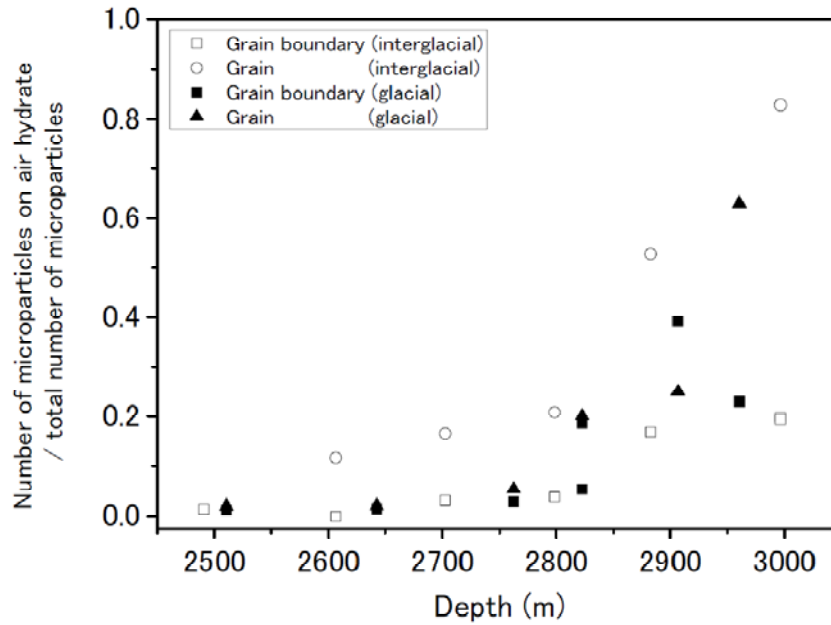


Figure 6.9 The ratio of microparticles on air hydrates in respective climate stages. “Grain boundary”; the sight include the grain boundary, “Grain”; exclude the grain boundary.

Depth m	Measuring sight	Climate period	Number concentration /mL	Number of particle N	Ice thickness mm	Average diameter µm
185.5	hydrate & grain boundary	Holocene	$0.42(\pm 0.07) \times 10^5$	221	2.0	$1.72(\pm 0.02)$
502.5	hydrate & grain boundary	Glacial Maximum	$3.64(\pm 0.36) \times 10^5$	736	1.7	$1.68(\pm 0.01)$
2491.0	hydrate & grain boundary	Interglacier	$0.43(\pm 0.11) \times 10^5$	91	1.4	$1.55(\pm 0.05)$
2510.5	hydrate & grain boundary	Glacial Maximum	$1.76(\pm 0.88) \times 10^5$	891	2.2	$1.74(\pm 0.01)$
2606.5	hydrate & grain boundary	Interglacier	$0.08(\pm 0.01) \times 10^5$	33	1.9	$1.81(\pm 0.04)$
2642.5	hydrate & grain boundary	Glacial Maximum	$12.1(\pm 1.5) \times 10^5$	3592	2.2	$1.72(\pm 0.01)$
2702.5	hydrate & grain boundary	Interglacier	$0.26(\pm 0.04) \times 10^5$	152	2.5	$1.82(\pm 0.28)$
2762.5	hydrate & grain boundary	Glacial Maximum	$5.32(\pm 0.68) \times 10^5$	2167	1.7	$1.66(\pm 0.01)$
2798.5	hydrate & grain boundary	Interglacier	$0.34(\pm 0.11) \times 10^5$	128	2.0	$1.79(\pm 0.02)$
2822.5	hydrate & grain boundary	Glacial Maximum	$0.45(\pm 0.08) \times 10^5$	218	2.0	$1.68(\pm 0.03)$
2822.5	hydrate & grain boundary	Glacial Maximum	$1.63(\pm 0.01) \times 10^5$	733	2.0	$1.78(\pm 0.01)$
2882.5	hydrate & grain boundary	Interglacier	$0.65(\pm 0.07) \times 10^5$	327	2.2	$1.84(\pm 0.02)$
2906.5	hydrate & grain boundary	Glacial Maximum	$2.22(\pm 0.66) \times 10^5$	1227	2.4	$1.98(\pm 0.06)$
2996.5	hydrate & grain boundary	Interglacier	$0.19(\pm 0.11) \times 10^5$	99	2.3	$1.99(\pm 0.10)$
2996.5	hydrate & grain boundary	Interglacier	$0.52(\pm 0.15) \times 10^5$	272	2.3	$1.82(\pm 0.01)$

Table 6.1 Microparticle survey. The table shows that the Number concentration ( $\text{mL}^{-1}$ ), Number of microparticles in the site (N), ice thickness (mm) and mean diameter ( $\mu\text{m}$ ).



# Chapter 7

## Microparticles in the GRIP ice core, Greenland

### 7.1 Purpose

In order to understand better the aerosol content of past atmospheres on North hemisphere in contrast to South hemisphere such as Antarctic ice cores, this paper undertakes a detailed analysis of the chemical form and abundance of salt inclusions found in the GRIP ice samples. We use several techniques: optical microscopy, micro-Raman spectroscopy, SEM-EDS, and ion chromatography. We measure the number density and size of micro-inclusions, and the total ion concentration of the ice samples. The results are published to the *Journal of Glaciology* (International Glaciological Society) [Sakurai et al., 2009].

### 7.2 Number density and diameter of microparticles

The number densities  $n$  ( $\text{mL}^{-1}$ ) and mean diameters  $d$  ( $\mu\text{m}$ ) of the microparticles found in each sample are shown in [Table 7.1](#). The number density of microparticles is more than an order of magnitude lower in the Holocene than in the glacial period. The mean diameter of the microparticles is about the same at each depth. The diameter distributions for each climate period are shown in [Figure 7.1](#). The overall shape of the distribution is the same in each period, in that the percentage of microparticles decreases with increasing diameter. The shapes of these distributions correspond well to the size distribution curves of larger dust particles [Steffensen, 1997], except for the outstanding abundance of 2.0-2.5  $\mu\text{m}$  inclusions in Holocene ice. This similarity suggests that water-soluble microparticles smaller than 2.0  $\mu\text{m}$  may have a distribution similar to that of dust. The excess of 2.0-2.5  $\mu\text{m}$  inclusions remains to be explained, but it seems likely that water-soluble compounds are responsible.

To illustrate the spatial distribution of microparticles, including both dust and water-soluble compounds, [Figure 7.2](#) illustrates the microparticles, clathrate hydrates, air bubbles, and grain boundaries observed in two samples of 6.9 and 30.0 kyrBP ice.

Note that the microparticles are not distributed uniformly in either sample; they tend to be found in tight groups. Previous research has postulated that the water-soluble impurities used as climate proxies are influenced by diffusion through a vein network [e.g. Rempel et al., 2001]. If the water soluble impurities exist as liquid phase, then these may diffuse through a vein network. However, we find that most of the microparticles (water soluble and dust) are distributed in the ice grain at these depths, and chemical forms of water soluble microparticles are measured by micro-Raman spectroscopy.

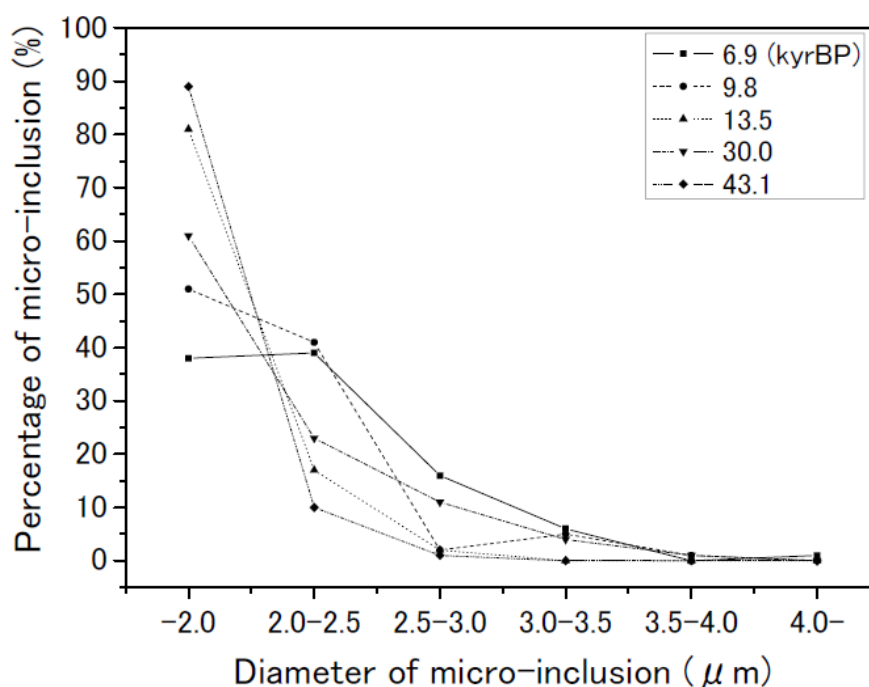


Figure 7.1. Percentage of microparticles in six diameter ranges. Inclusions of less than  $2.0\ \mu\text{m}$  diameter are merged into a single bin because their sizes have a large uncertainty. Inclusions of diameter greater than  $4.0\ \mu\text{m}$  are merged because they are rare.

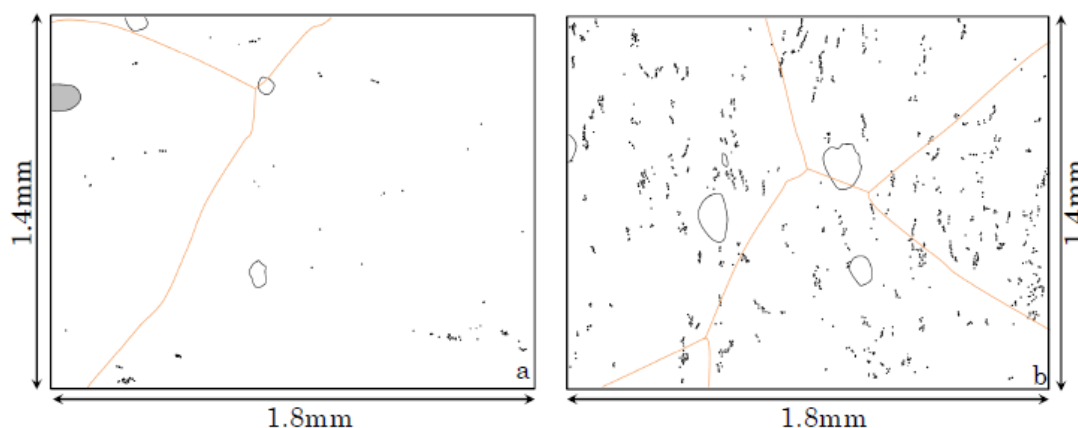


Figure 7.2. Spatial distribution of microparticles (black dots), clathrate hydrates (white regions), an air bubble (gray region), and grain boundaries (solid lines) in ice. Panel a) is a 1.4×1.8 mm section of 6.9 kyrBP ice, and b) is a similar section of 30.0 kyrBP ice. The thicknesses of the sections are 1.4 and 1.65 mm respectively.

### 7.3 Chemical form of microparticles

In the Raman spectra of the microparticles we found several sharp peaks. By comparing these data to the reference spectra of pure specimens, we can recognize some of these features. Below, we focus on  $\text{CaSO}_4 \cdot 2\text{H}_2\text{O}$  and  $\text{CaCO}_3$ , because calcium is the most abundant ion in GRIP ice.

Calcium sulfate ( $\text{CaSO}_4 \cdot 2\text{H}_2\text{O}$ ). In some inclusions, a sharp primary peak is detected at  $1009.05 \text{ cm}^{-1}$  with sub-peaks at 215.35, 414.23, 493.04, 620.75, and  $670.22 \text{ cm}^{-1}$  [Figures 7.3c,g]. Inclusions of this type were found at all five depths. The reference spectrum for  $\text{CaSO}_4 \cdot 2\text{H}_2\text{O}$  has its main peak at  $1007.84 \text{ cm}^{-1}$  (from the S-O symmetric stretching mode) and secondary peaks at 216.75, 413.60, 493.07, 620.78, and  $670.25 \text{ cm}^{-1}$  from other modes [Figures 7.3b,f]. The two Raman spectra correspond very well. Note that the 215.34 and  $216.75 \text{ cm}^{-1}$  peaks (Figures 7.3f,g) come from the ice itself (Figure 7.3a), as shown in Figure 7.3a,c. This analysis thus confirms the existence of  $\text{CaSO}_4 \cdot 2\text{H}_2\text{O}$  in the GRIP ice core.

Calcium carbonate ( $\text{CaCO}_3$ ). In the 30.0 kyrBP ice, some inclusions showed a sharp primary peak at  $1085.74 \text{ cm}^{-1}$  with sub-peaks at 215.38, 282.34 and  $711.70 \text{ cm}^{-1}$  [Figures 7.3e,i]. The reference spectrum of  $\text{CaCO}_3$  has its main peak at  $1085.74 \text{ cm}^{-1}$ , probably from the C-O symmetric stretching mode, and two sub-peaks at 281.66 and  $712.34 \text{ cm}^{-1}$  [Figures 7.3d,h]. Note that the  $215.38 \text{ cm}^{-1}$  [Figure 7.3.i] peak comes from the ice itself [Figure 7.3a]. The observed spectra thus clearly indicate the presence of  $\text{CaCO}_3$  in the GRIP ice core [Figures 7.3d,e,h,i].

## 7.4 SEM-EDS

Microparticles exposed by sublimation inside the SEM chamber (as described in the Methods section) were measured by EDS. SEM images of microparticles found in the 6.9 kyrBP and 30.0 kyrBP ice are shown in Figures 7.4d and e respectively. X-ray spectra of three microparticles observed in the 6.9 kyrBP and 30.0 kyrBP ice samples are shown in Figures 7.4a, b and c respectively. In the 6.9kyrBP samples (Figures 7.4a,b,d) both S and Ca were identified. An abundance of O was also measured, which mainly comes from ice. Microparticles having both S and Ca turned out to be  $\text{CaSO}_4 \cdot 2\text{H}_2\text{O}$ . In the 30.0 kyrBP sample, the microparticle contains C, O and Ca (Figures 7.4c,e). Such inclusions most likely consist of  $\text{CaCO}_3$ . The results of SEM-EDS analysis therefore support the Raman spectroscopy identification of  $\text{CaSO}_4 \cdot 2\text{H}_2\text{O}$  and  $\text{CaCO}_3$ .

Taking the micro-Raman spectroscopy and SEM-EDS results together, we can surely claim the first direct evidence that  $\text{CaSO}_4 \cdot 2\text{H}_2\text{O}$  and  $\text{CaCO}_3$  exist as solid phase microparticles in the GRIP ice core.

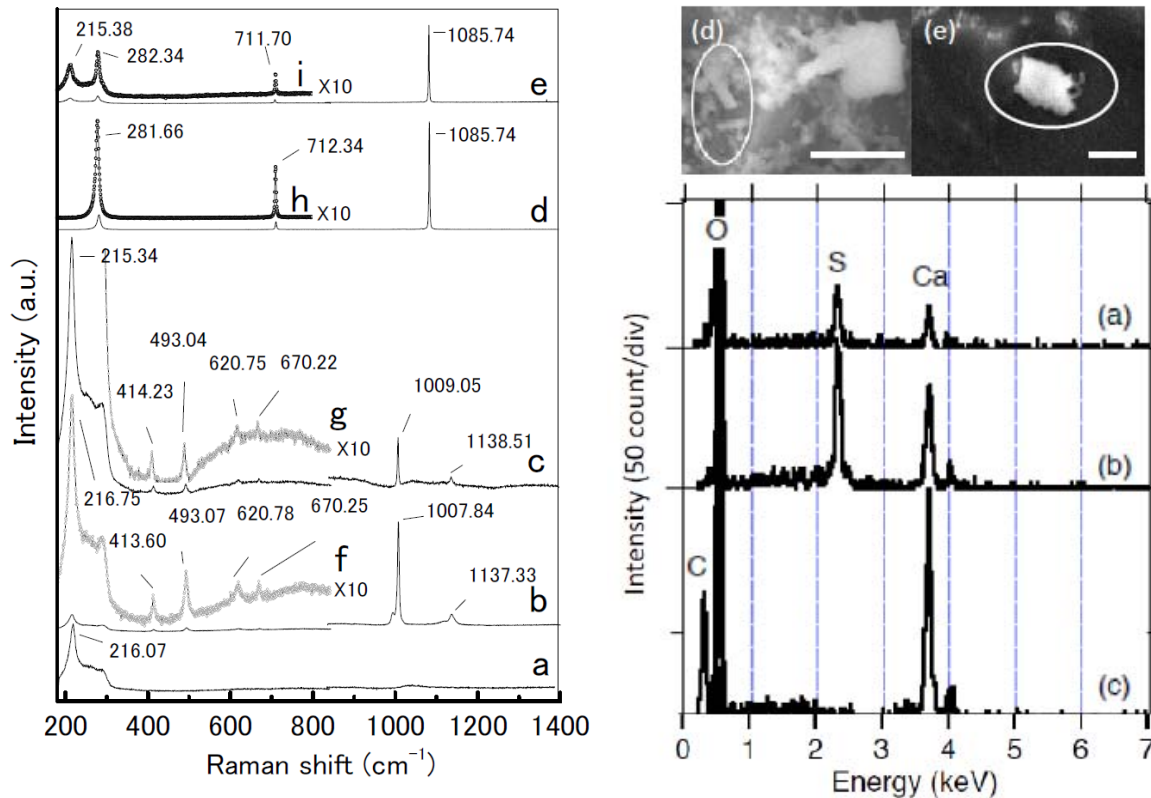


Figure 7.3. Raman spectra of reference specimens and the measured microparticles: (a) GRIP ice without inclusions, (b) pure specimen of  $\text{CaSO}_4 \cdot 2\text{H}_2\text{O}$  in ice prepared with ultrapure water, (c)  $\text{CaSO}_4 \cdot 2\text{H}_2\text{O}$  inclusion found in the GRIP ice core (the spectrum is from 9.8 kyrBP), (d) pure specimen of  $\text{CaCO}_3$ , (e)  $\text{CaCO}_3$  inclusion found in 30.0 kyrBP ice from the GRIP core. Curves (f) through (i) are magnifications (10 $\times$ ) of spectra (b) through (e) respectively, from 180 to 850  $\text{cm}^{-1}$ .

Figure 7.4. X-ray spectra of microparticles found in 6.9 kyrBP ice (a) and 30.0 kyrBP ice (b,c). Inclusions (a) and (b) are deduced to be  $\text{CaSO}_4 \cdot 2\text{H}_2\text{O}$  (containing oxygen, sulfur, and calcium). Inclusion (c) is deduced to be  $\text{CaCO}_3$  (containing oxygen, carbon, and calcium). (d) and (e) are pictures of the inclusions yielding spectra (a) and (c) respectively.

## 7.5 Ion chromatography

To further support the above results, we measured the concentrations of sodium, magnesium, calcium, chloride, nitrate, and sulfate ions in the same ice sections by ion chromatography (Table 7.1). In Holocene ice, we find fewer calcium ions than sulfate and nitrate ions: 0.58 vs. 1.58  $\mu\text{eq/L}$  at 6.9 kyrBP and 0.70 vs. 2.67  $\mu\text{eq/L}$  at 9.8 kyrBP, where the second figure is the total concentration of  $[\text{NO}_3^- + \text{SO}_4^{2-}]$ . On the other hand, in the 30.0 kyrBP section, we find a significant excess of calcium ions (7.17  $\mu\text{eq/L}$ ) compared to the sulfate and nitrate ions (totaling 2.98  $\mu\text{eq/L}$ ). The 43.1 kyrBP ice has a more modest excess of calcium ions (1.97  $\mu\text{eq/L}$ ) with respect to sulfate and nitrate ions (2.16  $\mu\text{eq/L}$ ).

These results can support a discussion of the chemical compounds present in ice [Iizuka et al., 2008]. The ion balance observed in Holocene ices (6.9 kyrBP and 9.8 kyrBP) suggests that the calcium ion could exist as both  $\text{CaSO}_4 \cdot 2\text{H}_2\text{O}$  and calcium nitrate. In the 30.0 kyrBP ice, the excess of calcium ions strongly suggests the presence of  $\text{CaCO}_3$ . In the 43.1 kyrBP ice, a more modest excess of calcium ions suggests that a small amount of  $\text{CaCO}_3$  should have remained. Although the existence of these compounds is inferred, the results support the findings of micro-Raman spectroscopy and SEM-EDS analysis. Note, however, that we did not find direct evidence of  $\text{CaCO}_3$  in the 43.1 kyrBP ice over the course of this analysis. This section must therefore have significantly less  $\text{CaCO}_3$  than the 30.0 kyr BP section. Analysis of more inclusions would probably reveal some, but the process is very time-consuming.

## 7.6 Microparticles identified by Raman spectroscopy

The number of microparticles measured by Raman spectroscopy is given in [Table 7.1](#). The number density includes both water-soluble and water-insoluble inclusions, as shown in [Figure 7.5](#). Among water-soluble inclusions, we expect to find sulfate, nitrate, and chloride salts given the results of ion chromatography (see [Section 3.3](#) and [Table 7.1](#)). As our earlier measurements of reference chemical compounds demonstrate, both sulfate and carbonate salts have strong symmetric stretching modes (S-O and C-O respectively). The nitrate salt also has a symmetric (N-O) stretching mode, but its response is relatively weak. We therefore could not find direct evidence for nitrate salts in the ice via Raman spectroscopy in this study. Chloride salts (e.g.  $\text{NaCl} \cdot 2\text{H}_2\text{O}$ ) can be identified by their hydrate (O-H) vibration mode in the range  $3100 - 3600\text{cm}^{-1}$  [[Dubessy et al. 1982](#)], but this signal may be hidden by the O-H vibration of ice in this measurement.

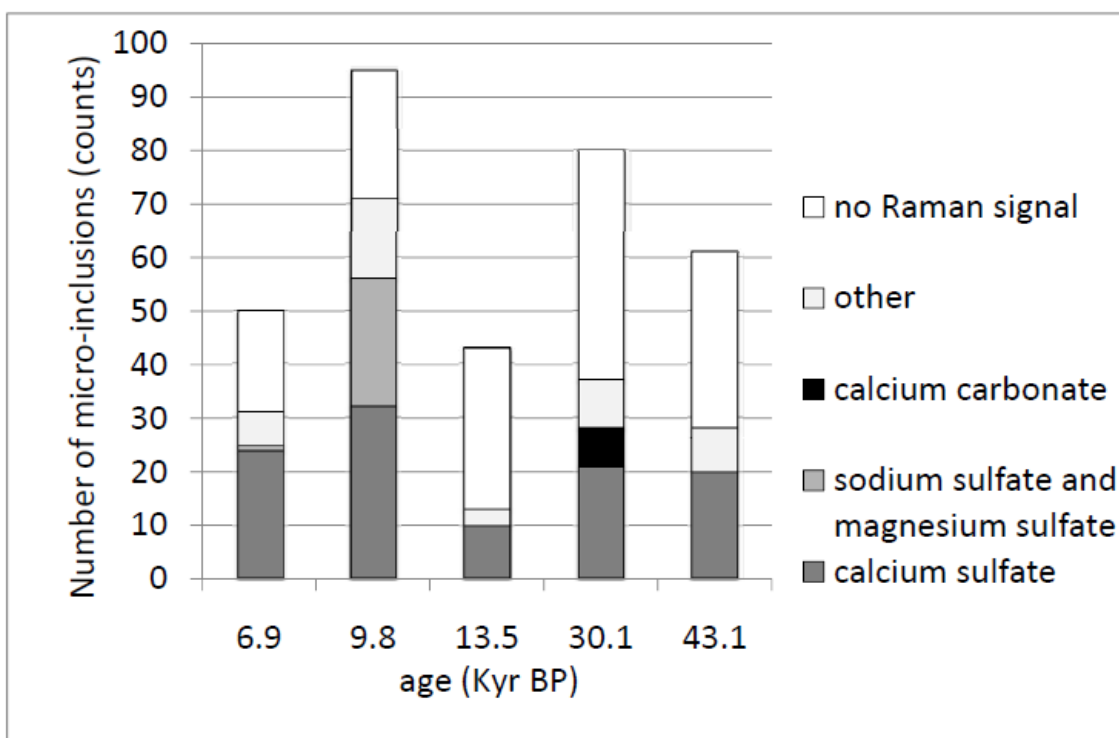


Figure 7.5. Number of microparticles identified as containing various compounds in the GRIP ice core.  $\text{CaSO}_4 \cdot 2\text{H}_2\text{O}$  is a major compound at all depths.  $\text{Na}_2\text{SO}_4 \cdot 10\text{H}_2\text{O}$  and  $\text{MgSO}_4 \cdot 11\text{H}_2\text{O}$  are difficult to distinguish ([Ohno et al., 2005, 2006](#)).  $\text{CaCO}_3$  is found only in the 30.0 kyrBP ice. Nitrate and quartz are also present, and classified in the “Other” category along with some spectra which have not yet been identified. Inclusions for which no spectral features other than those of ice could be detected are classified as “no Raman signal”.

A few water-insoluble microparticles (such as dust) were partly identified by their chemical compounds, while others could not be matched to reference spectra. The latter are classified as “Other” in [Figure 7.5](#). Microparticles with no Raman peaks except for the ice background are classified as “Undetectable”, although they may well possess a weak signal hidden by the ice. For all the reasons given above, only water-soluble inclusions containing sulfate and carbonate salts could be clearly identified by this method.

[Figure 7.5](#) shows that  $\text{CaSO}_4 \cdot 2\text{H}_2\text{O}$  exists not just in glacial period ice but also in Holocene ice. On the other hand,  $\text{Na}_2\text{SO}_4 \cdot 10\text{H}_2\text{O}$  and  $\text{MgSO}_4 \cdot 11\text{H}_2\text{O}$  were found only in Holocene ice sections (6.9 kyr BP and 9.8 kyr BP). The Raman spectra of  $\text{Na}_2\text{SO}_4 \cdot 10\text{H}_2\text{O}$  and  $\text{MgSO}_4 \cdot 11\text{H}_2\text{O}$  are difficult to distinguish from one another, because the molecules have very similar stretching modes. These sulfate salts have already been discussed in two of our previous papers [[Ohno et al., 2005, 2006](#)]. We found  $\text{CaCO}_3$  in the 30.0 kyr BP ice section, but could not find it in the 43.1 kyr BP ice section. As the ion chromatography results suggest, the amount of  $\text{CaCO}_3$  in the latter section is probably too small to measure easily [[Table 7.1](#)].

## 7.7 Importance of the findings of water-soluble microparticles in GRIP ice core

This study provides the first direct evidence that calcium sulfate ( $\text{CaSO}_4 \cdot 2\text{H}_2\text{O}$ ) and  $\text{CaCO}_3$  exist in solid form in the Greenland ice core, using micro-Raman spectroscopy and SEM-EDS analysis of individual inclusions to support the results of ion chromatography. The existence of  $\text{CaCO}_3$  and  $\text{CaSO}_4 \cdot 2\text{H}_2\text{O}$  in the Greenland ice core has previously been inferred from ion chromatography [[Mayewski et al., 1994](#); [Legrand et al., 1997](#)], and the existence of carbonate has previously been deduced by SEM-EDS [[Maggi, 1997](#); [Laj et al., 1997](#)]. Our own findings confirm the existence of both  $\text{CaCO}_3$  and  $\text{CaSO}_4 \cdot 2\text{H}_2\text{O}$  in GRIP ice. [Sala et al. \[2008\]](#) showed by Raman spectroscopy that the three type of calcium carbonates are found in the shallow ice of Antarctic ice sheet, such as  $\text{CaCO}_3$ ,  $\text{CaCO}_3 \cdot 2\text{H}_2\text{O}$ , and  $\text{CaCO}_3 \cdot 6\text{H}_2\text{O}$ . It can be distinguished very clearly by the micro-Raman spectroscopy. In this study, we could not find calcium carbonates except  $\text{CaCO}_3$ . We now discuss how ion concentrations can be estimated from the abundance of salt inclusions, the significance of excess carbon dioxide from  $\text{CaCO}_3$ , and the paleoclimatological impact of these results.

## 7.7.1 Ion concentration estimates based on microparticles volume

To determine the proportion of calcium ions originating from  $\text{CaSO}_4 \cdot 2\text{H}_2\text{O}$  and  $\text{CaCO}_3$  in the form of microparticles, we estimated the total mass of such inclusions in the ice section (see the last paragraph of Methods section). Because it is difficult to measure the particle volume, we treated all inclusions as spheres. In ice from the glacial period and Termination I, it is clear that  $\text{CaSO}_4 \cdot 2\text{H}_2\text{O}$  inclusions (and  $\text{CaCO}_3$ , especially in the 30.0 kyrBP section) make the most important contribution. The calcium ion abundance calculated from microparticles is comparable to that measured by ion chromatography [Table 7.1]: at least 74, 68, and 98% of calcium ions can be attributed to  $\text{CaSO}_4 \cdot 2\text{H}_2\text{O}$  in the 13.5, 30.0, and 43.1 kyrBP samples respectively. At least 8% of calcium ions come from  $\text{CaCO}_3$  in the 30.0 kyrBP sample. In Holocene ice, on the other hand,  $\text{CaSO}_4 \cdot 2\text{H}_2\text{O}$  contributes only 22 % (21 %) of calcium ions in the 6.9 (9.8) kyrBP sections respectively. The remaining ions probably come from other salts.

## 7.7.2 Significance of carbon dioxide

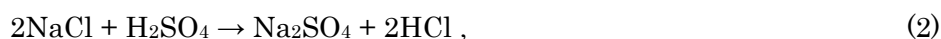
The amount of  $\text{CaCO}_3$  deduced to exist in the ice is sensitive to the measuring method. Anklin et al. [1995] compared two  $\text{CO}_2$  measurements in GRIP ice, obtained by melting-refreezing and dry extraction. In the first method,  $\text{CaCO}_3$  dissolves in the melted ice and probably reacts with acid in solution; this produces more  $\text{CO}_2$  than would be observed in a dry extraction process. The excess  $\text{CO}_2$  can be calculated from the chemical reaction, written as



This formula implies that one mol of  $\text{CaCO}_3$  produces one mol of excess  $\text{CO}_2$  and one mol of  $\text{Ca}^{2+}$ . We measured 0.28  $\mu\text{mol/L}$  (0.55  $\mu\text{eq/L}$ ) of  $\text{Ca}^{2+}$  in the form of  $\text{CaCO}_3$ ; hence only 0.28  $\mu\text{mol/L}$  (12.19ppb) of excess  $\text{CO}_2$  could be produced from our observed number density of  $\text{CaCO}_3$ . This could not explain the observed excess of  $\text{CO}_2$  that Anklin et al. [1995, 1997] suggested. This difference appears to suggest that we should have found more  $\text{CaCO}_3$  in the 30.0 kyrBP ice by Raman spectroscopy. Heterogeneous chemical reactions that take place during measurement might also have been active in the ice sheet and/or atmosphere when the layer was formed.

### 7.7.3 Significance of sulfate and carbonate salts

Equation 1 is strongly dependent on the acidity of the ice. For the GRIP ice core, this quantity has already been determined by electrical conductivity measurement (ECM) [Wolff et al., 1995, 1997]. In Holocene ice the existence of acid leads to the chemical reaction



which supports our findings for the existence of  $\text{Na}_2\text{SO}_4 \cdot 10\text{H}_2\text{O}$  and  $\text{MgSO}_4 \cdot 11\text{H}_2\text{O}$  in Holocene ice. In contrast, less acidity is expected in the glacial period ice due to the presence of  $\text{CaCO}_3$ .

The existence of sulfates and carbonates in the atmosphere is related to the process of radiative forcing. Jarzembski et al. [2003] showed that sulfate and carbonate salts have significantly different refractive indices of absorption from ultraviolet to infrared. The origins of calcium ions in various climate conditions have been previously discussed by several authors [Mayewsky et al., 1994, Legrand et al., 1997, Laj et al., 1997, De Angelis et al., 1997, Svensson et al., 2000]. A study of Sr and Nd isotopic compounds and rare earth concentrations suggests that eastern Asia was the main source of dust (including calcium ions) during the last glacial period [Svensson et al., 2000]. With respect to the Holocene, Dibb et al. [2007] found that most aerosols came from Asia and the Sahara desert. These studies suggest that sulfate and carbonate were transported by the atmosphere from Asia and/or the Sahara desert to the Greenland ice sheet.

It is still necessary to clarify which chemical reactions occurred during formation of the ice sheet, as well as quantifying their rates. Achieving this understanding will allow the paleoclimatology community to discuss how the radiative forcing of aerosols occurred in detail.

Depth (m)	Period (Kyr BP)	N	n (/mL)	d ( $\mu$ m)	thickness (mm)	Ion concentrations ( $\mu$ eq/L)					$\text{NO}_3^- + \text{SO}_4^{2-}$	
						$\text{Cl}^-$	$\text{NO}_3^-$	$\text{SO}_4^{2-}$	$\text{Na}^+$	$\text{Mg}^{2+}$		$\text{Ca}^{2+}$ ( $\text{Calc. Ca}^{2+}$ )
1200.35 – 1200.39	Holocene	14(50)	$0.06(\pm 0.01) \times 10^5$	$2.15(\pm 0.49)$	3.3(1.4)	0.66	0.99	0.59	1.08	0.14	0.58 (0.13)	1.58
1501.66 – 1501.70	Holocene	28(95)	$0.12(\pm 0.03) \times 10^5$	$2.05(\pm 0.45)$	2.8	0.94	1.23	1.44	0.91	0.24	0.70 (0.15)	2.67
1700.61 – 1700.65	Termination I	200(43)	$0.85(\pm 0.09) \times 10^5$	$1.74(\pm 0.31)$	5.0	1.16	1.19	1.20	1.06	0.36	1.84 (1.37)	2.40
2099.90 – 2099.95	Last Glacial Period	1017(80)	$4.3(\pm 0.5) \times 10^5$	$2.03(\pm 0.47)$	2.0(1.65)	1.99	0.93	2.05	1.76	1.03	7.17 (4.89)[0.55]	2.98
2300.65 – 2300.70	Last Glacial Period	500(61)	$2.1(\pm 0.4) \times 10^5$	$1.72(\pm 0.24)$	2.0	1.32	1.14	1.02	1.23	0.51	1.97 (1.92)	2.16

Table 7.1. Microparticle counts and ion concentrations in the five GRIP ice core sections. N is the total number of microparticles found by optical microscope in all 100 views (i.e., the whole  $1.8 \times 1.4 \times \text{thickness mm}^3$  sample, where one view is  $0.80.14 \times \text{thickness mm}^3$ ). The number of inclusions measured using Raman spectroscopy is given in parentheses. n is the number density of microparticles in the sample volume. d is the mean diameter of the microparticles. The thicknesses of the ice section analyzed are also shown. The number in parentheses is the thickness of the section which was re-sliced by microtome at the time the spatial distribution was measured, following measurement of the number density and mean diameter of the microparticles. The ion concentrations measured at each depth are averaged over five samples, and expressed in micro equivalents per liter.  $\text{Calc. Ca}^{2+}$  is calculated from the diameter and number density of  $\text{CaSO}_4 \cdot 2\text{H}_2\text{O}$  and  $\text{CaCO}_3$ . The sum of the two major anion concentrations [ $\text{NO}_3^- + \text{SO}_4^{2-}$ ] is also given.

# Chapter 8

## Summary

This chapter summarizes the main achievements of this research: (1) identifying the chemical forms of water-soluble microparticles in the Antarctic and Greenland ice cores, and describing their variation with climate; (2) analyzing the nature and behavior of water-soluble microparticles as a function of depth; (3) miscellaneous minor results; and (4) future prospects.

### **(1) Chemical forms of water-soluble microparticles in the Antarctic and Greenland ice cores as functions of climate.**

This study found that several salts exist as microparticles in the Antarctic and Greenland ice cores. The chemical forms of these microparticles are related to the concentrations of acids and  $\text{Ca}^{2+}$ .

In the Antarctic (Dome Fuji) ice core, for instance, we found that interglacial periods (including the Holocene) have higher acidity than the LGM ice. Evidence in the chemical form of microparticles using micro-Raman spectroscopy shows that  $\text{Na}_2\text{SO}_4 \cdot 10\text{H}_2\text{O}$  and  $\text{MgSO}_4 \cdot 11\text{H}_2\text{O}$  are abundant in the Holocene microparticles, while the presence of NaCl in LGM ice can be assumed from ion balance. This discrepancy must be related to the acidity of the ice. The chemical reaction of chloride salts with non-sea-salt sulfuric acid (originating from phytoplankton) allows the formation of  $\text{Na}_2\text{SO}_4 \cdot 10\text{H}_2\text{O}$  and  $\text{MgSO}_4 \cdot 11\text{H}_2\text{O}$  during interglacial periods. In contrast, the LGM ice has lower acidity because most of the  $\text{Ca}^{2+}$  ions combine with non-sea-salt sulfuric acid to form  $\text{CaSO}_4 \cdot 2\text{H}_2\text{O}$ . Thus, if the concentration of  $\text{Ca}^{2+}$  is high, then the acidity is low (see [Chapter 3](#)). This study also found  $(\text{CH}_3\text{SO}_3)_2\text{Mg} \cdot n\text{H}_2\text{O}$  in the LGM ice from Dome Fuji, supporting the evidence of lower acidity. During the LGM,  $(\text{CH}_3\text{SO}_3)_2\text{Mg} \cdot n\text{H}_2\text{O}$  could have formed in the atmosphere and/or along the edge of sea ice and later been transported as an aerosol to the surface of ice sheet, where it would have a chance to survive due to the low acidity of the ice (see [Chapter 4](#)).

In the Greenland ice core, on the other hand, ice from the last glacial period is much less acidic or even alkaline. Dust particles are also much more abundant in the Greenland ice than in the Antarctic ice. To explain these features, previous studies have suggested the existence of  $\text{CaCO}_3$  in the ice, a hypothesis confirmed by this study. The Holocene ice is more acidic than the last glacial period ice, so the chemical reaction of non-sea-salt sulfuric acid and chloride salts should have taken place to form

$\text{Na}_2\text{SO}_4 \cdot 10\text{H}_2\text{O}$  and  $\text{MgSO}_4 \cdot 11\text{H}_2\text{O}$  as with the Dome Fuji core. We did find these chemicals in Holocene ice of the Greenland core, under the same acidic conditions observed in Holocene ice of Dome Fuji ice core (see Chapter 7). To sum up, these discrepancies in the chemical forms of microparticles found in the Antarctic and Greenland ice cores can be fully explained by a variation in the concentrations of acid and  $\text{Ca}^{2+}$  with climate.

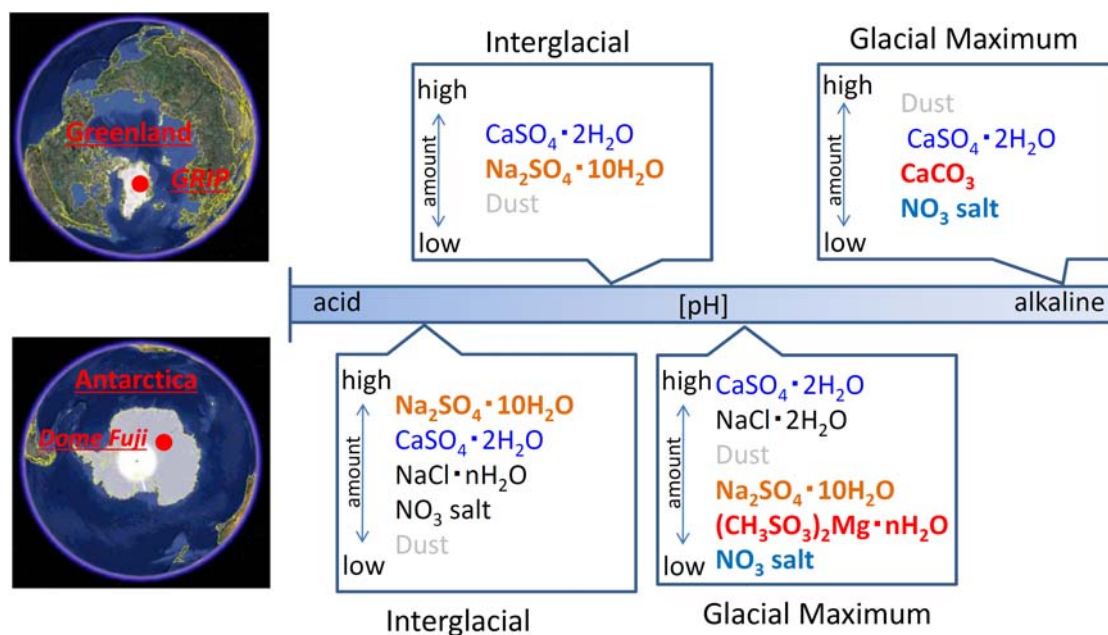


Figure 8.1 Relative abundance of water-soluble microparticles related to the acidity of the ice. Chemicals printed in color are confirmed directly by this research, while those printed in black are inferred from the observed ion balance.

## (2) Nature and behavior of water-soluble microparticles as a function of depth.

The chemical form of the ions found in ice cores has been debated for more than twenty years. Thermodynamic models imply that several acids, especially sulfuric acid, can diffuse through the vein network along ice grain boundaries and thereby disturb climate proxies. Our measurements reveal that while liquid sulfate does indeed form, it is not distributed over a network of veins. Rather, we find liquid sulfate in isolated microparticles consisting of the ternary phase  $\text{Na}_2\text{SO}_4 \cdot \text{HCl} \cdot \text{H}_2\text{O}$ , in equilibrium with the ice sheet. These *liquid sulfate microparticles* (including  $\text{Na}^+$ ,  $\text{SO}_4^{2-}$ ,  $\text{Cl}^-$ ,  $\text{H}^+$ ) are present even in the middle of the ice sheet (approximately 1500 m depth, for the Dome Fuji ice core) at a temperature of  $-37.4^\circ\text{C}$ . Below that depth, the phase transition of  $\text{Na}_2\text{SO}_4 \cdot 10\text{H}_2\text{O}$  to liquid sulfate ( $\text{Na}^+$ ,  $\text{SO}_4^{2-}$ ,  $\text{Cl}^-$ ,  $\text{H}^+$ ) and/or liquid sulfate ( $\text{SO}_4^{2-}$ ,  $\text{H}^+$ )

with  $\text{NaCl}\cdot n\text{H}_2\text{O}$  follows the solidus line in the ternary phase diagram, which strongly depends on the temperature and concentration of HCl. The ratio of liquid sulfate to all other kinds of microparticles tends to increase as a function of depth, as shown in Figure 8.2. Our results further suggest that the ions ( $\text{Na}^+$ ,  $\text{SO}_4^{2-}$ ,  $\text{Cl}^-$ ) should exist as liquid particles even at the grain boundary, because the energy of the liquid sulfate-ice interface is greater than half of the grain boundary energy. This evidence is particularly relevant to research reconstructing the oldest climate histories from deep ice cores (see Chapter 5). Further study is needed to quantify the interface energies between ice and liquid sulfate and between grain boundaries as a function of depth, and the latter's dependence on the degree of orientation among adjacent grains of ice.

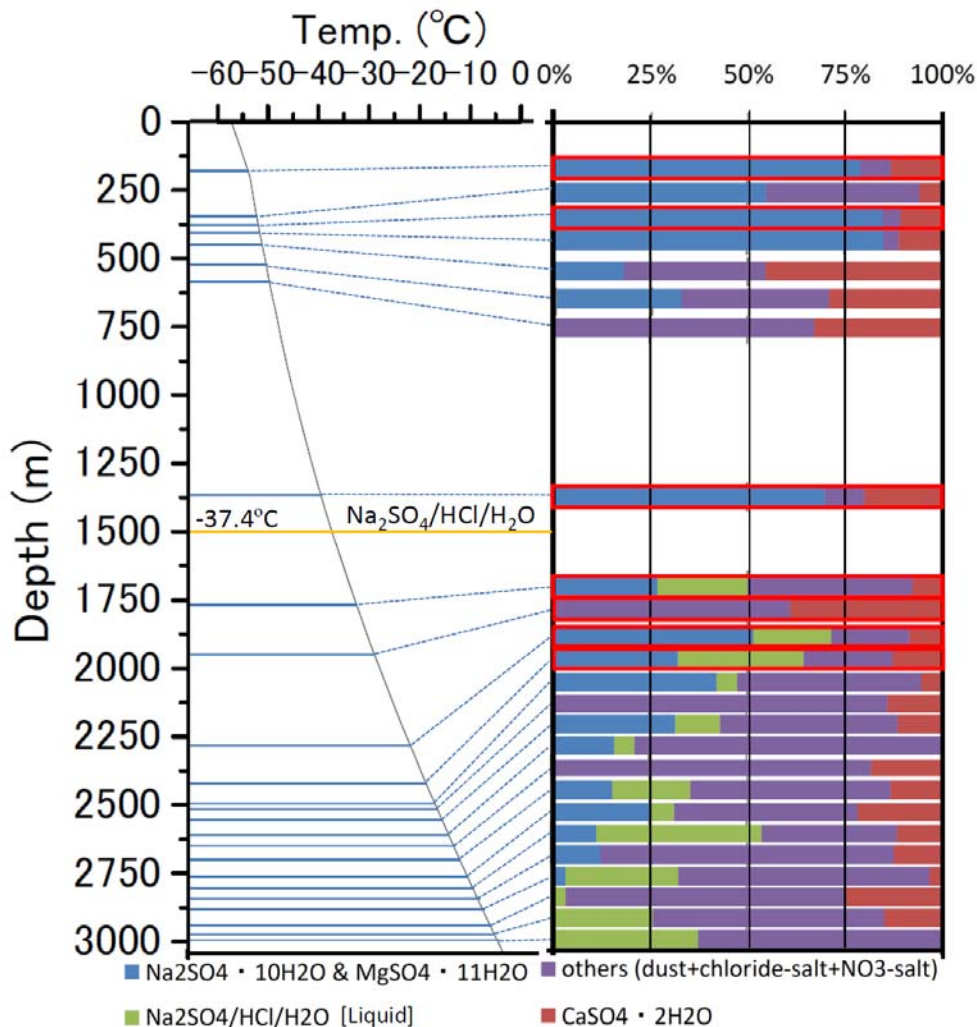


Figure 8.2. The chemical compositions of water-soluble microparticles at various depths in the Dome Fuji ice core. The depth marked in yellow is at  $-37.4^\circ\text{C}$ , the eutectic temperature of  $\text{Na}_2\text{SO}_4\text{-HCl-H}_2\text{O}$  (Chapter 5). The red frame displays the original data, from Ohno et al. [2006].

A previous study reported that most of the microparticles at shallow depths of Dome Fuji ice core are located within the ice grains [Ohno et al., 2005]. The same study clarified that in deep ice, microparticles (including liquids and solids) are also preserved at the grain boundaries due to their tendency to aggregate (and their larger size). In the deepest part of the ice, almost 30% of microparticles are located on the air hydrates. In other words, the air hydrates play an important role as reservoirs of microparticles in the deep ice sheet. Thus, while the past climate history can be reliably reconstructed from ions and dust particles, the time resolution must take into account not only the grain size (i.e., the distribution of grain boundaries) but also the distribution of air hydrates. These findings are significant with respect to the resolution of reliable proxies in ice cores for the reconstruction of Earth's environmental history (see [Chapter 6](#)).

### (3) Miscellaneous remarks

In the deepest part of the ice sheet, the temperature is very close to the melting point of ice and we can assume that most of the water-soluble microparticles are melted.

At a depth of 3019.5 m (716.506 kyr B.P.) in the Dome Fuji ice core, we observed a crack with a diameter of approximately 1 cm ([Figure 8.3\(1\) A](#)). In the polarized image, both the ice grain and the grain boundary appear to originate from the crack ([Figure 8.3\(2\) A](#)). Using an optical microscope, we observed a string of particles along the grain boundary originating from the crack for a distance of several millimeters (hereafter referred to as the “linear system”) ([Figure 8.3\(1\)c](#)). We also see many micro-bubbles within the linear system. We obtained several Raman spectra from these particles. [Figure 8.3\(3\)a](#) shows a plate-like inclusion near the linear system. Its Raman spectra did not have any peaks except those expected from pure ice ([Figure 8.3\(5\)a](#)).

The Raman spectra of N<sub>2</sub> and O<sub>2</sub> gases in the air hydrates and the air bubbles were studied previously in a symmetric stretching mode [e.g., [Ikeda et al., 2000](#)], and those of N<sub>2</sub> and O<sub>2</sub> gases in air bubbles were studied using the low-frequency rotation mode [[de Boer et al., 1994](#)]. The latter measurements produced Raman spectra with several sharp spikes around 50 cm<sup>-1</sup> ([Figures 8.3\(5\)b, c, and d](#); [broken circle](#)). The rotation features were relatively intense compared to the symmetric stretching mode of N<sub>2</sub> and O<sub>2</sub> in air bubbles at 2329.03 and 1555.07 cm<sup>-1</sup> respectively.

Raman spectra from crystalline particles in the linear system (e.g., [Figure 8.3\(3\)f](#)) are shown in [Figures 8.3\(5\)c, d, and f](#). The spectra display S–O symmetric

stretching modes around 989 and 1009  $\text{cm}^{-1}$ , the former indicating the presence of  $\text{Na}_2\text{SO}_4 \cdot 10\text{H}_2\text{O}$  and/or  $\text{MgSO}_4 \cdot 11\text{H}_2\text{O}$ , and the latter  $\text{CaSO}_4 \cdot 2\text{H}_2\text{O}$ . These particles were distributed over almost the entire length of the linear system. On the other hand, several hundred micrometers away from the linear system, we found air hydrates several tens of micrometers in diameter (Figure 8.3(4)). Within the air hydrates, we found liquid sulfates (Figure 8.3(5)g).

In general, this study has shown that sulfates exist as liquid microparticles in equilibrium with and containing HCl in the deep ice sheet (Chapter 5). However, the discovery of solid sulfates at 3019.5m shows a different mechanism at work. Just above this depth, at 2996.5 m, we found that most of the sulfates do exist in liquid form. This discrepancy can be explained by the presence of the grain boundary, which caused sulfates to aggregate and solidify in a nonequilibrium state. In other words, the solid sulfates along the grain boundary may have formed during the drilling procedure or under *in situ* conditions, but their distribution is clearly different from what is typical for the core. However, the phenomenon cannot be explained in detail based on the available data; further study is necessary to interpret it.

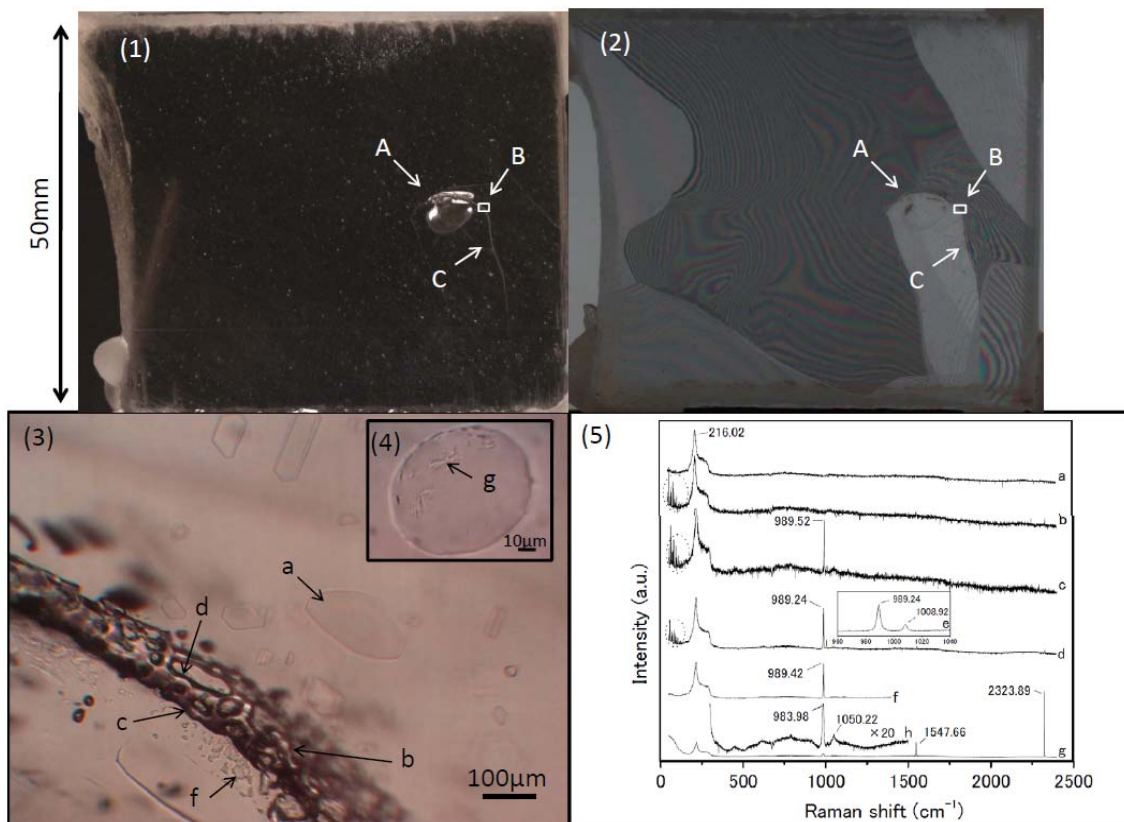


Figure 8.3 Impurities found on a grain boundary at the depth of 3019.5m. (1) non-polarized image,

(2) polarized image, (3) optical microscope image. In (3), several features are labeled: (a) cleavage crack, (b) gas ( $N_2$ ,  $O_2$ ), (c) and (d) gas with solid sulfates, and (f) solid sulfate crystal. The inset (4) shows liquid sulfate on an air hydrate (g). Panel (5) shows the Raman spectra of these features.

#### (4) Future prospects

This research demonstrates that it is possible to reconstruct both water-soluble and water-insoluble aerosols from the present day to 720 thousand years B.P. (see [Chapters 3 and 5](#)), albeit with limited time resolution in the deepest parts of the ice sheet (see [Chapters 5 and 6](#)). Please note that this does not mean that whole aerosols can be reconstructed, because some problems remain. For example, the original aerosols may have reacted with acids and chloride salts in the firn and/or atmosphere (see [Chapter 3](#)).

In principle, the radiative forcing of aerosols can be modeled given the number density and morphology of the particles, the latter aspect comprising refractive index, scattering angle, and size. (For the moment, I am speaking only of the direct effect of radiation on aerosol particles, not indirect effects such as cloud nucleation.) Thus, continued study of these samples should focus on the morphologies of each compound present (salts and solid acids), which are not yet fully understood. [IPCC \[2007\]](#) reported that the radiative forcing of sulfate shows negative feedback. Because  $(NH_4)_2SO_4$  is the dominant sulfate in the present urban atmosphere, and  $Na_2SO_4$  is assumed to be dominant in the maritime atmosphere as well, their report attracted much attention [e.g., [Shettle and Fenn, 1979](#), [Tang et al., 1995](#), [Hess, 1998](#), [Penner et al., 2001](#)]. However, little is known about the other sulfates (e.g.,  $H_2SO_4 \cdot nH_2O$ ,  $Na_2SO_4 \cdot 10H_2O$ ,  $MgSO_4 \cdot 11H_2O$ , and  $CaSO_4 \cdot 2H_2O$ ) and other aerosols (including salts and acids), which form numerous hydrates ([Figure 8.4](#)).

We know that  $H_2O$  absorbs in the infrared band. Thus, we can assume that hydrated aerosols should also absorb infrared light. In other words, we can surmise that the water-soluble aerosols, especially sulfates, do not always give negative feedback during glacial-interglacial cycles and during the present time period. Further study of the morphology of aerosols is important to understand the direct effects of radiative forcing.

Moreover, to truly clarify the mechanism of glacial-interglacial cycles, we have to take into account not only the direct effect of radiative forcing of aerosols but also the indirect effect, i.e., aerosols acting as cloud condensation nuclei [e.g., [Hudson and Da, 1996](#)]. Deglaciation is significant, but glaciations are much more important to

understand the Earth's future prospects. From this point of view, it is important to ask how hydrated aerosols directly and indirectly affect radiative forcing during both glaciations and deglaciations. I hope that further research on the morphology of solid salt particles and the radiative forcing of water-soluble aerosols will eventually resolve the underlying mechanism of glacial-interglacial cycles.

In order to calculate the effects of radiative forcing on past and present atmospheric aerosols in Antarctica, however, we should not just understand every glacial and interglacial period from inland ice cores. It is equally important to clarify the concentrations of past atmospheric aerosols in coastal Antarctica, other inland locations on the ice sheet, and Greenland. Given the success of our ion balance calculations, I imagine that similar rules exist to reconstruct the past atmospheric water-soluble aerosols over the whole continent of Antarctica as well as in Greenland.

I wish to emphasize the point that we still do not know how the direct and indirect radiative forcing of water-soluble aerosols in the past atmosphere governs the glacial-interglacial cycles. This problem is tractable, however, and will be an important aspect of my future research!

#### Possibility of aerosol (solid)

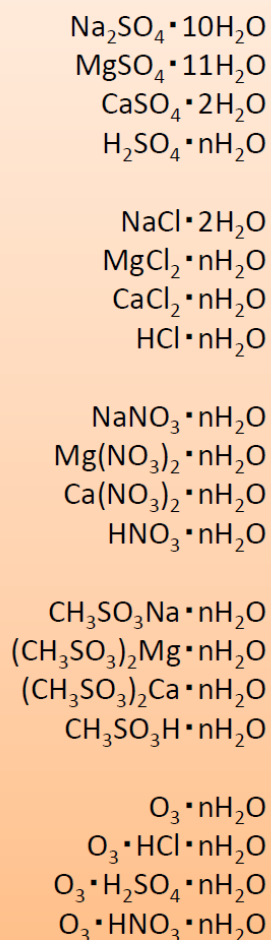


Figure 8.4 Diversity of aerosols in the past atmosphere. All of these chemical forms of acids and salts could have existed in past atmospheres. However, most of the solids are still not fully understood because their chemical forms can include any number of hydrates, and because metastable states can form in the atmosphere. For instance, if the atmospheric temperature is lower than the temperature of eutectic concentration of  $\text{MgSO}_4\text{-H}_2\text{O}$ , then  $\text{MgSO}_4\cdot 11\text{H}_2\text{O}$  is a stable phase but  $\text{MgSO}_4\cdot 7\text{H}_2\text{O}$  is metastable [unpublished data, Genceli et al., 2007]. The sulfuric acid forms  $\text{H}_2\text{SO}_4\cdot 4\text{H}_2\text{O}$  and  $\text{H}_2\text{SO}_4\cdot 8\text{H}_2\text{O}$ , however, are both stable [Beyer et al., 2003]. If we wish to discuss the radiative forcing of aerosols in past atmospheres, the boundary between metastability and stability should be clarified immediately. For ozone hydrates [Vysokikh et al., 2008], it is also important to study the chemical reactions that lead to ozone holes at high altitude.



# Acknowledgements

I would like to express sincere gratitude to my supervisor Takeo Hondoh, professor at the Institute of Low Temperature Science and vice-president of Hokkaido University, for providing me with the precious opportunity to serve as a student in his laboratory, and his boundless guidance and support. I would also like to express appreciation to my technical supervisor, Assistant Professor Yoshinori Iizuka, for guidance, encouragement and invaluable discussions. I wish to thank Professor Yoshinori Furukawa of the Institute of Low Temperature Science for valuable comments on this thesis and guiding me through the basics of snow and ice physics. Finally, I gratefully acknowledge Associate Professor Tsutomu Uchida of the Graduate School of Engineering for helpful advice and encouragement throughout my studies.

I would like to express my appreciation to the drilling teams of the Dome Fuji, GRIP, and EDML ice cores. I am deeply grateful to Professors Sigfús Johnsen, Dorthe Dahl-Jensen, and Jørgen Peder Steffensen at the Niels Bohr Institute of Astronomy (Copenhagen, Denmark) and Chief Researcher Sepp Kipfstuhl at the Alfred-Wegener Institute for Polar and Marine Research (Germany). Their work provided this precious opportunity to study water-soluble microparticles in the GRIP and EDML ice cores.

I would like to thank Associate Professor Shuji Fujita at the National Institute of Polar Research for helpful discussions, kindly sharing his data, and for leading to international exposure. I would like to thank Dr. Hiroshi Ohno (National Research Council, Canada) for teaching me the fundamental techniques to measure water-soluble microparticles in ice. I am grateful to Associate Professor Akira Hori (Kitami Institute of Technology) for valuable discussions, to Dr. Atsushi Miyamoto (Institute of Low Temperature Science) for guidance on basic ice core studies, to Dr. Shinichiro Horikawa (Nagoya University) for helpful discussions and guidance on measurement techniques, to Dr. Junichi Okuyama (IHI Inc.) for general scientific guidance, and to all four for helpful discussions of polar ice core studies while I was a research student at the Institute of Low Temperature Science. I also wish to thank the Glacier and Ice sheet Research Group at the Institute of Low Temperature Science for creating such a supportive and stimulating environment.

Special thanks are due to Chief researcher Teruo Aoki at the Meteorological Research Institute, Professor Ralf Greve at the Institute of Low Temperature Science,

Professor Akira Kouchi (the President of the Institute of Low Temperature Science), Professor Akira Tsuchiyama (Osaka University), and Professor Werner F. Kuhs (University Göttingen, Germany) for valuable advice.

I also thank Assistant Professor Atsushi Tani (Osaka University), Assistant Professor Elif Genceli-Guner (Delft University of Technology, Netherlands), and Lecturer Sergio H. Faria, (University Göttingen, Germany) for advice, help, and encouragement. I am grateful to Professor Manabu Fukui, vice-President of the Institute of Low Temperature Science, for academic and career counseling. I extend special thanks to Dr. Ben Mathiesen for English correction and editing of my scientific papers.

Last but not least, I would like to thank my parents, my wife, Megumi Sakurai, and my son, Koichi Sakurai, for their continuous and unfailing support, which has been of vital importance.

# References

- Abbatt, J.P.D., K.D.Beyer,A.F. Fucaloro, J.R. McMahon, P.J. Wooldridge, R. Zhang, and M.J. Molina, 1992. Interaction of HCl vapor with water-ice: Implications for the Stratosphere, *J. Geophys. Res.* 97(D14), 15,819-15,826.
- Alley, R.B., J.H. Porepezko, and C.R. Bentley, 1986. Grain growth in polar ice: I. Theory, *J. Glaciol.*, 32(112), 415-433.
- Anklin, M., J-M. Barnola, J. Schwander, B. Stauffer, and D. Raynaud, 1995. Processes affecting the CO<sub>2</sub> concentrations measured in Greenland ice, *Tellus*, 47B, 461-470.
- Anklin, M., J. Schwander, B. Stauffer, J. Tschumi, and A. Fuchs, 1997. CO<sub>2</sub> record between 40 and 8 kyr B.P. from the Greenland Ice Core Project ice core, *J. Geophys. Res.*, 102(C12), 26539-26545.
- Azuma, N., and A. Higashi, 1983. Effects of hydrostatic pressure on the rate of grain growth in Antarctic polycrystalline ice, *J. Phys. Chem.*, 87(21), 4060-4064.
- Baker, I., and D. Cullen, 2003. SEM/EDS observations of impurities in polar ice: artifacts or not?, *J. Glaciol.*, 49 (165), 184-190.
- Barletta, R.E., B.N. Gros and M.P. Herring. 2009. Analysis of marine biogenic sulfur compounds using Raman spectroscopy: dimethyl sulfide and methane sulfonic acid. *J. Raman Spectrosc.*, 40, 972-981.
- Barnes, P.R.F., R. Mulvaney, E.W. Wolff, and K. Robinson, 2002. A technique for the examination of polar ice using the scanning electron microscope, *J. Microscopy*, 205, 118-124.
- Barnes, P.R.F., E.W. Wolff, H.M. Mader, R. Udisti, E. Castellano, and R. Röthlisberger, 2003. Evolution of chemical peak shapes in the Dome C, Antarctica, ice core, *J. Geophys. Res.*, 108(D3), 4126, doi:10.1029/2002JD002538.
- Beaudon, E. and J. Moore. 2009. Frost flower chemical signature in winter snow on

- Vestfonna ice cap. *The Cryosphere Discuss.*, **3**, 159 - 180.
- Beyer, K.D., A.R. Hansen, M. Poston, 2003. The search for sulfuric acid octahydrate: Experimental evidence. *J. Phys. Chem. A* **107**. 2025 - 2032.
- Burgess, C.P., and K. Zuber, 2000. Footprints of the newly discovered Vela supernova in Antarctic ice cores?, *Astropart. Phys.*, **14**, 1-6.
- Charlson, R.J., J.E. Lovelock, M.O. Andreae and S.G. Warren, 1987. Oceanic phytoplankton, atmospheric sulphur, cloud albedo and climate, *Nature*, **326**, 655-661.
- Charsley, E.L. 1993. Introduction to the work of the ICTAC Committee on standardization, *J. Thermal Anal.*, **40**, 1399-1404.
- Chylek P., and U. Lohmann, 2008. Aerosol radiative forcing and climate sensitivity deduced from the Last Glacial Maximum to Holocene transition, *Geophys. Res. Lett.*, **35**, L04804, doi:10.1029/2007GL032759.
- Claquin, T., et al. 2003. Radiative forcing of climate by ice-age atmospheric dust, *Clim. Dynam.*, **20**, 193-202.
- CRC Handbook of chemistry and physics, 2000-2001.
- Curran, M.A.J., T.D. van Ommen, V.I. Morgan, K.L. Phillips and A.S. Palmer. 2003. Ice Core Evidence for Antarctic Sea Ice Decline Since the 1950s. *Science*, **302**, 1203-1206.
- de Angelis, M., J.P. Steffensen, M. Legrand, H. Clausen and C. Hammer, 1997. Primary aerosol (sea salt and soil dust) deposited in Greenland ice during the last climatic cycle: Comparison with east Antarctic records, *J. Geophys. Res.*, **102**(C12), 26681-26698.
- de Angelis, M., J.R. Petit, J. Savarino, R. Souchez, and M.H. Thiemens, 2004. Contributions of an ancient evaporitic-type reservoir to subglacial Lake Vostok chemistry, *Earth and Planet. Sci. Lett.*, **222**, 751-765.
- de Angelis, M., M-C. Morel-Fourcade, J-M. Barnola, J. Susini, and P. Duval 2005. Brine micro-droplets and solid inclusions in accreted ice from Lake Vostok (East

- Antarctica), *Geophys. Res. Lett.*, **32**, L12501, doi:10.1029/2005GL022460.
- de Boer, R.C., P.H.M. van Loosdrecht, and H.L.M. Meekes, 1994. Identification of gaseous oxygen and nitrogen in bubble inclusion in  $\text{Bi}_4(\text{GeO}_4)_3(\text{BGO})$  crystals by means of Raman spectroscopy, *J. Cryst. Growth*, **140**, 361-364.
- de Gennes, P.G., 1985. Wetting: statics and dynamics, *Rev. Mod. Phys.*, **57**, 827-863.
- Delmas, R.J., P. Wagnon, K. Goto-Azuma, K. Kamiyama and O. Watanabe. 2003. Evidence for the loss of snow-deposited MSA to the interstitial gaseous phase in central Antarctic firn. *Tellus*, **55B**, 71-79.
- Dibb, J.E., S.I. Whitlow and M. Arsenault, 2007. Seasonal variations in the soluble ion content of snow at Summit, Greenland: Constraints from three years of daily surface snow samples, *Atmos. Environ.*, **41**, 5007-5019.
- Dome-F Deep Coring Group, Deep ice-core drilling at Dome Fuji and glaciological studies in east Dronning Maud Land, Antarctica, *Ann. Glaciol.*, **27**, (1998) 333-337.
- Dreschhoff, G.A.M., and C.M. Laird, 2006. Evidence for a stratigraphic record of supernovae in polar ice, *Adv. Space Res.*, **38**, 1307-1311.
- Dubessy, J., D. Audeoud, R. Wilkins and C. Kosztolanyi, 1982. The use of the Raman microprobe mole in the determination of the electrolytes dissolved in the aqueous phase of fluid inclusions, *Chem. Geol.*, **37**, 137-150.
- Durand, G., et al., 2006. Effect of impurities on grain growth in cold ice sheets, *J. Geophys. Res.*, **111**, F01015:1-18.
- Durig, J.R., L. Zhou, T. Schwartz and T. Gounev. 2000. Fourier transform Raman spectrum, vibrational assignment and *ab initio* calculation of methanesulfonic acid in the gas and liquid phases. *J. Raman Spectrosc.*, **31**, 193-202.
- EPICA community members. 2004. Eight glacial cycles from an Antarctic ice core. *Nature* **429**, 623 - 628.
- Fattori, I., S. Becagli, S. Bellandi, E. Castellano, M. Innocenti, A. Mannini, M. Severi, V. Vitale, and R. Udisti, 2005. Chemical composition and physical features of

- summer aerosol at Terra Nova Bay and Dome C, Antarctica, *J. Environ. Monit.*, **7**, 1265-1274.
- Finlayson-Pitts, B.J., and J.N. Pitts, 2000. *Chemistry of the upper and lower atmosphere: Theory, experiments and applications*, pp. 969, Academic Press, San Diego, California.
- Fletcher, N.H., 1970. *The chemical physics of ice*, Cambridge at the University Press.
- Fujii, Y., M. Kohno, S. Matoba, H. Motoyama, O. Watanabe, A 320 k-year record of microparticles in the Dome Fuji, Antarctica ice core measured by laser-light scattering, *Mem. Natl Inst. Polar Res.*, **57** (2003), 46-62.
- Fujita, S., et al., 2002. Linear and non-linear relations between the high-frequency-limit conductivity, AC-ECM signals and ECM signals of Dome F Antarctic ice core from a laboratory experiment, *Ann. Glaciol.*, **35**, 321-328.
- Fukazawa, H., K. Sugiyama, S. Mae, H. Narita, and T. Hondoh, 1998. Acid ions at triple junction of Antarctic ice observed by Raman scattering, *Geophys. Res. Lett.*, vol.25(15), 2845-2848.
- Gao, C., L. Oman, A. Robock, and G.L. Stenchikov, 2007. Atmospheric volcanic loading derived from bipolar ice cores: Accounting for the spatial distribution of volcanic deposition, *J. Geophys. Res.*, **112**, D09109, doi:10.1029/2006JD007461.
- Genceli, F.E, M. Lutz, A.L. Spek and G.J. Witkamp. 2007. Crystallization and characterization of a new magnesium sulfate hydrate  $MgSO_4 \cdot 11H_2O$ , *Cryst. Growth Des.*, **7**(12), 2460-2466.
- Genceli, E.F., S. Horikawa, Y. Iizuka, T. Sakurai, T. Hondoh, T. Kawamura, G-J. Witkamp, 2009. Meridianiite detected in ice, *J. Glaciol.*, **55**(189), 117-122.
- Greenland Ice-core Project (GRIP) members, 1993. Climate instability during the last interglacial period recorded in the GRIP ice core, *Nature*, **364**, 203-207.
- Hara, K., K. Osada, M. Kido, M. Hayashi, K. Matsunaga, Y. Iwasaka, T. Yamanouchi, G. Hashida, T. Fukatsu, 2004. Chemistry of sea-salt particles and inorganic halogen species in Antarctic regions: Compositional differences between coastal

- and inland station, *J. Geophys. Res.*, 109 (D20), D20208.
- Hall, C., and A. Hamilton, The heptahydrate of sodium sulfate: Does it have a role in terrestrial and planetary geochemistry?, *Icarus*, 198 (2008), 277-279.
- Hamilton, A., and C. Hall, Sodium sulfate heptahydrate: a synchrotron energy-dispersive diffraction study of an elusive metastable hydrated salt, *J. Anal. At. Spectrom.*, 23 (2008) 840-844.
- Hess, M., P. Koepke, and I. Schult, 1998. Optical properties of aerosols and clouds: the software package OPAC, *B. Am. Meteorol. Soc.*, 79(5), 831-844.
- Higashi, A., 1978. Structure and behavior of grain boundaries in polycrystalline ice, *J. Glaciol.*, 21(85), 589-605.
- Hillig, W.B., 1998. Measurement of interfacial free energy for ice/water system, *J. Cryst. Growth*, 183(3), 463-468.
- Hondoh, T., A. Higashi, 1978. X-ray diffraction topographic observations of the large-angle grain boundary in ice under deformation, *J. Glaciol.*, 21(85), 629-638.
- Hondoh, T., A. Higashi, 1979. Anisotropy of migration and faceting of large-angle grain boundaries in ice bicrystals, *Phil. Mag. A*, 31, 138.
- Hondoh, T., H. Shoji, O. Watanabe, A.N. Salamatin and V.Ya. Lipenkov. 2002. Depth-age and temperature prediction at Dome Fuji station, East Antarctica. *Ann. Glaciol.*, **35**, 384-390.
- Hynes, A.J., P.H. Wine and D.H. Semmes. 1986. Kinetics and mechanisms of OH reactions with organic sulfides. *J. Phys. Chem.*, **90**, 4148-4156.
- IPCC, 2007. Summary for Policymakers. In: Solomon, S, D. Qin, M. Manning, Z. Chen, M. Marquis, K.B. Averyt, M. Tignor, H.L. Miller (Eds.), *Climate Change 2007: the Physical Science Basis. Contribution of Working Group I to the Fourth Assessment Report of the Intergovernmental Panel on Climate Change*. Cambridge University Press, Cambridge, UK and New York, NY, USA.
- Iizuka, Y., M. Takata, T. Hondoh, Y. Fujii, 2004. High-time-resolution profiles of soluble ions in the last glacial period of a Dome Fuji (Antarctica) deep ice core,

- Ann. Glaciol.*, 39, 452-456.
- Iizuka, Y., T. Hondoh, Y. Fujii, 2006. Na<sub>2</sub>SO<sub>4</sub> and MgSO<sub>4</sub> salts during the Holocene period derived by high-resolution depth analysis of a Dome Fuji ice core, *J. Glaciol.*, 52, 58-64.
- Iizuka, Y., T. Hondoh, and Y. Fujii, 2008a. Antarctic sea ice extent during the Holocene reconstructed from inland ice core evidence, *J. Geophys. Res.*, 113, D15114, doi:10.1029/2007JD009326.
- Iizuka, Y., S. Horikawa, T. Sakurai, S. Johnsen, D. Dahl-Jensen, J.P. Steffensen, and T. Hondoh, 2008b. A relationship between ion balance and the chemical compounds of salt particles found in the Greenland Ice Core Project and Dome Fuji ice cores, *J. Geophys. Res.*, 113, doi:10.1029/2007JD009018.
- Ikeda-Fukazawa, T., and T. Hondoh, 2001. Variation in N<sub>2</sub>/O<sub>2</sub> ratio of occluded air in Dome Fuji Antarctic ice, *J. Geophys. Res.*, 106(D16), 17,799-17,810.
- Jaffrezo, J.L., C.I. Davidson, M. Legrand and J.E. Dibb. 1994. Sulfate and MSA in the air and snow on the Greenland Ice Sheet. *J. Geophys. Res.*, **99**(D1), 1241-1253.
- Jarzembski, M.A., M.L. Norman, K.A. Fuller, V. Srivastava and D.R. Cutten, 2003. Complex refractive index of ammonium nitrate in the 2-20 $\mu$ m spectral range, *Appl. Optics*, **42**(6), 922-930.
- Jayaraman, A., D.L. Wood, R.G. Maines, Sr., 1987. High-pressure Raman study of the vibrational mode in AlPO<sub>4</sub> and SiO<sub>2</sub> ( $\alpha$ -quartz), *Phys. Rev. B*, 35, 8316-8321.
- Johnsen, S.J., D. Dahl-Jensen, W. Dansgaard and N.S. Gundestrup, 1995. Greenland paleotemperatures derived from GRIP borehole temperature and ice core isotope profiles, *Tellus*, 47B(5), 624-629.
- Johnsen, S.J., H.B. Clausen, W. Dansgaard, N. Gundestrup, C.U. Hammer, U. Andersen, K.K. Andersen, C.S. Hvidberg, D. Dahl-Jensen, J.P. Steffensen, H. Shoji, A.E. Sveinbjörnsdóttir, J. White, J. Jouzel and D. Fisher. 1997. The  $\delta^{18}\text{O}$  record along the Greenland Ice Core Project deep ice core and the problem of possible Eemian climatic instability, *J. Geophys. Res.*, **102**(C12), 26397 - 26410.

- Kargel, J.S., 1991. Brine volcanism and the interior structures of asteroids and icy satellites, *Icarus*, 94, 368-390.
- Laj, P., G. Ghermandi, R. Cecchi, V. Maggi, C. Riontino, S. Hong, J-P. Candelone and C. Boutron, 1997. Distribution of Ca, Fe, K, and S between soluble and insoluble material in the Greenland Ice Core Project ice core, *J. Geophys. Res.*, **102**(C12), 26615 - 26623.
- Lambert F., et al., Dust-climate couplings over the past 800,000 years from the EPICA Dome C ice core, *Nature*, vol.452 (2008), 616 – 619.
- Legrand, M., C. Feniet-Saigne, E.S. Saltzman, C. Germain, N.I. Barkov and V.N. Petrov. 1991A. Ice-core record of oceanic emissions of dimethylsulphide during the last climate cycle. *Nature*, **350**, 144-146.
- Legrand, M. and C. Feniet-Saigne. 1991B. Strong El Niño revealed by methanesulphonic acid in South Polar snow layers. *Geophys. Res. Lett.*, **21**, 187-190.
- Legrand M., C. Feniet-Saigne, E.S. Saltzman and C. Germain. 1992. Spatial and temporal variations of methanesulfonic acid and non sea salt sulphate in Antarctic ice. *J. Atmos. Chem.*, **14**, 245-260.
- Legrand, M., M. De Angelis, and F. Maupetit, 1993. Field investigation of major and minor ions along summit (Central Greenland) ice cores by Ion Chromatography, *J. Chromatogr.*, **640** (1-2), 251-258.
- Legrand, M., C. Hammer, M. De Angelis, J. Savarino, R. Delmas, H. Clausen, and S.J. Johnsen, 1997. Sulfur-containing species (methanesulfonate and SO<sub>4</sub>) over the last climatic cycle in the Greenland Ice Core Project (central Greenland) ice core, *J. Geophys. Res.*, **102**(C12), 26663-26679.
- Liu, Y., and P.H. Daum, 2008. Relationship of refractive index to mass density and self-consistency of mixing rules for multicomponent mixtures like ambient aerosols, *Aerosol Sci.*, 39, 974-986.
- Lu, H., S.A. McCartney, V. Sadtchenko, 2009. H/D exchange kinetics in pure and HCl

- doped polycrystalline ice at temperatures near its melting point: Structure, chemical transport, and phase transitions at grain boundaries. *J. Chem. Phys.* **130**, 054501.
- Marion, G.M., R.E. Farren and A.J. Komrowski. 1999. Alternative pathways for seawater freezing. *Cold Reg. Sci. Technol.*, **29**, 259 - 266.
- Matrai, P.A., L. Tranvik, C. Leck, and J.C. Knulst, 2008. Are high Arctic surface microlayers a potential source of aerosol organic precursors?, *Mar. Chem.*, 108, 109-122.
- Maggi, V. 1997. Mineralogy of atmospheric microparticles deposited along the Greenland Ice Core Project ice core, *J. Geophys. Res.*, **102**(C12), 26725-26734.
- Mayewski, P.A., L.D. Meeker, S. Whitlow, M.S. Twickler, M.C. Morrison, P. Bloomfield, G.C. Bond, R.B. Alley, A.J. Gow, P.M. Grootes, D.A. Meese, M. Ram, K.C. Taylor and W. Wumkes. 1994. Changes in atmospheric circulation and ocean ice cover over the North Atlantic during the last 41,000 years, *Science*, **263**, 1747-1751.
- McKeown, D.A., 2005. Raman spectroscopy and vibrational analyses of albite: From 25°C through the melting temperature, *Am. Mineral.*, 90, 1506-1517.
- McMorrow, A., T.D. van Ommen, V. Morgan and M.A.J. Curran. 2004. Ultra-high-resolution seasonality of trace-ion species and oxygen isotope ratios in Antarctic firn over four annual cycles. *Ann. Glaciol.*, **39**, 34-40.
- Mizoguchi, K., Hori, Y., Tominaga, Y., 1992. Study on dynamical structure in water and heavy water by low-frequency Raman spectroscopy. *J. Chem. Phys.* **97** (3), 1961 - 1968.
- Mulvaney, R., E.W. Wolff, and K. Oates, 1988. Sulphuric acid at grain boundaries in Antarctic ice, *Nature*, 331, 247-249.
- Mulvaney, R., E.C. Pasteur, D.A. Peel, S. Saltzman and P.Y. Whung. 1992. The ratio of MSA to non-sea-salt sulphate in Antarctic Peninsula ice cores. *Tellus*, **44B**, 295-303.
- Nye, J.F., and S. Mae, 1972. The effect of non-hydrostatic stress on intergranular water

- veins and lenses in ice, *J. Glaciol.*, 11(61), 81-101.
- Ohno, H., M. Igarashi and T. Hondoh. 2005. Salt particles in polar ice core: Location and chemical form of water-soluble impurities. *Earth Planet. Sci. Lett.*, **232**, 171-178.
- Ohno, H., M. Igarashi and T. Hondoh. 2006. Characteristics of salt particles in polar ice from Dome Fuji, East Antarctica. *Geophys. Res. Lett.*, **33**, doi:10.1029/2006GL025774.
- Oswald, I.D.H., A. Hamilton, C. Hall, W.G. Marshall, T.J. Prior, and C.R. Pulham 2008. In situ characterization of elusive salt hydrates - The crystal structures of the heptahydrate and octahydrate of sodium sulfate, *J. Am. Chem. Soc.*, 130, 17795-17800.
- Pasteur, E. C. and R. Mulvaney. 1999. Laboratory study of the migration of methane sulphonate in firn. *J. Glaciol.*, **45**, 214-218.
- Pasteur, E.C. and R. Mulvaney. 2000. Migration of methanesulphonate in Antarctic firn and ice. *J. Geophys. Res.*, **105**(D9), 11525-11534.
- Paterson, W.S.B., 1994. *The physics of Glaciers*, 3<sup>rd</sup> edition, Elsevier Science Ltd., pp.192-203.
- Penner, J.E., et al., 2001: Aerosols, their direct and indirect effects. In: *Climate Change 2001: The Scientific Basis. Contribution of Working Group I to the Third Assessment Report of the Intergovernmental Panel on Climate Change* [Houghton, J.T., et al. (eds.)]. Cambridge University Press, Cambridge, United Kingdom and New York, NY, USA, pp. 289-348.
- Petit, J.R., Jouzel, J., Raynaud, D., Barkov, N.I., Barnola, J.-M., Basile, I., Bender, M., Chappellaz, J., Davis, M., Delaygue, G., Delmotte, M., Kotlyakov, V.M., Legrand, M., Lipenkov, V.Y., Lorius, C., Pepin, L., Ritz, C., Saltzman, E., Stievenard, M., 1999. Climate and atmospheric history of the past 420,000 years from the Vostok ice core, Antarctica. *Nature* **399**, 426 - 436.
- Rankin, A.M., E.W. Wolff and S. Martin. 2002. Frost flowers: Implication for

- tropospheric chemistry and ice core interpretation. *J. Geophys. Res.*, **107**(D23), doi:10.1029/2002JD002492.
- Rempel, A.W., E.D. Waddington, J.S. Wettlaufer, and M.G. Worster, 2001. Possible displacement of the climate signal in ancient ice by premelting and anomalous diffusion, *Nature*, 411, 568-571.
- Rempel, A.W., and J.S. Wettlaufer, 2002. Anomalous diffusion of multiple impurity species: Predicted implication for the ice core climate records, *J. Geophys. Res.*, **107**(B12), 2330, doi: 10.1029/2002JB001857.
- Ruth, U., D. Wagenbach, R. Mulvaney, H. Oerter, W. Graf, H. Pulz and G. Littot, 2005. Comprehensive 1000 year climatic history from an intermediate-depth ice core from the south dome of Berkner Island, Antarctica: methods, dating and first results. *Ann. Glaciol.*, **39**, 146-154.
- Röthlisberger, R., R. Mulvaney, E.W. Wolff, M.A. Hutterli, M. Bigler, M. de Angelis, M.E. Hansson, J.P. Steffensen and R. Udisti. 2003. Limited dechlorination of sea-salt aerosols during the last glacial period: Evidence from the European Project for Ice Coring in Antarctica (EPICA) Dome C ice core. *J. Geophys. Res.*, **108**(D16), 4526, doi:10.1029/2003JD003604.
- Saigne, C. and M. Legrand. 1987. Measurements of methanesulphonic acid in Antarctic ice. *Nature*, **330**, 240-242.
- Sakurai, T., et al., 2009. Direct observation of salts as micro-inclusions in the Greenland GRIP ice core, *J. Glaciol.*, **55**(193), 777-783.
- Sala, M., et al. 2008. Evidence of calcium carbonates in coastal (Talos Dome and Ross Sea area) East Antarctica snow and firn: Environmental and climatic implications, *Earth and Planet. Sci. Lett.*, **271**, 43-52.
- Saltelli, A. and J. Hjorth. 1995. Uncertainty and sensitivity analyses of OH-initiated Dimethylsulfide (DMS) oxidation kinetics. *J. Atmos. Chem.*, **21**, 187-221.
- Savarino, J., J. Kaiser, S. Morin, D.M. Sigman, and M.H. Thiemens, 2007. Nitrogen and oxygen isotopic constraints on the origin of atmospheric nitrate in coastal

- Antarctica, *Atmos. Chem. Phys.*, **7**, 1925-1945.
- Schubnell, M. 2000. Temperature and heat flow calibration of a DSC-instrument in the temperature range between -100 and 160°C. *J. Therm. Anal. Calorim.*, **61**, 91-98.
- Schweiger, G., 1987. *In-situ* determination of the molecular composition of aerosol particles in a monodisperse model aerosol. *Part. Character.*, **4**, 67.
- Schweiger, G., 1991. Raman scattering on microparticles: size dependence. *J. Opt. Soc. Am.*, **B**, **8**, 1770-1778.
- Shettle, E.P., R.W. Fenn, 1979. *Models for the aerosols of the lower atmosphere and the effects of humidity variations on their optical properties*, AFGL-TR-79-0214, Air Force Geophysics Laboratory.
- Smith, B., T. D. van Ommen and M.A.J. Curran. 2004. Methanesulphonic acid movement in solid ice cores. *Ann. Glaciol.*, **39**, 540-544.
- Socrates, G. 2001. *Infrared and Raman characteristic group frequencies: table and charts*, 3<sup>rd</sup> ed., John Wiley & Sons Ltd., Chichester, Table 22.1.
- Steffensen, J.P. 1997. The size distribution of microparticles from selected segments of the Greenland Ice Core Project ice core representing different climatic periods, *J. Geophys. Res.*, **102**(C12), 26755-26763.
- Svensson, A., P.E. Biscaye, and F.E. Grousset, 2000. Characterization of late glacial continental dust in the Greenland Ice Core Project ice core, *J. Geophys. Res.*, **105**(D4), 4637-4656.
- Takahashi, S., T. Kameda, H. Enomoto, T. Shiraiwa, Y. Kodama, S. Fujita and H. Motoyama. 1998. Automatic weather station program during Dome Fuji Project by JARE in east Dronning Maud, Antarctica. *Ann. Glaciol.*, **27**, 528 - 534.
- Takei, I., and N. Maeno, 1997. Dielectric low-frequency dispersion and crossover phenomena of HCl-doped ice, *J. Phys. Chem. B*, **101**, 6234-6236.
- Tang, I.N., K.H. Fung, D.G. Imre, and H.R. Munkelwitz, 1995. Phase transformation and metastability of hygroscopic microparticles, *Aerosol Sci. Tech.*, **23**:3, 443-453.

- Tsuchimoto, 2010. *Analysis of chemical composition of nonvolatile micro impurities in surface snow of the Dome Fuji, Antarctica*. Master thesis.
- Turner, J., S.A. Harangozo, J.C. King W.M. Connolley, T.A. Lachlan-Cope and G.J. Marshall. 2003. An exceptional winter sea-ice retreat / Advance in the Bellingshausen Sea, Antarctica. *Atmos. Ocean*, **41**(2), 171-185.
- Uzdowski, E., M. Dietzel, 1998. *Atlas and Data of Solid-Solution Equilibria of Marine Evaporites*, Springer.
- Vehring, R., H. Moritz, D. Niekamp, G. Schweiger, and P. Heinrich, 1995. Linear Raman spectroscopy on droplet chains: A new experimental method for the analysis of fast transport processes and reaction on microparticles. *Appl. Spectro.*, **49**, 1215-1224.
- von Glasow, R., R. von Kuhlmann, M.G. Lawrence, U. Platt, and P.J. Crutzen, 2004. Impact of reactive bromine chemistry in the troposphere, *Atmos. Chem. Phys.*, **4**, 2481-2497.
- Videnova-Adrabinska, V., 1990. Polarized IR and Raman study of the  $\text{Na}_3\text{H}(\text{SO}_4)_2$  single crystal, *J. Mol. Struct.*, **237**, 367-388.
- Vysokikh, T.A., T.V. Yagodovskaya, S.V. Savilov, and V.V. Lunin, 2008. Experimental modeling of the processes of ozone hydrate clathrate formation, *Russian J. Phys. Chem. A.*, **82**(4), 686-689.
- Wagnon, P., R.J. Delmas and M. Legrand. 1999. Loss of volatile acid species from upperfirn layers at Vostok, Antarctica. *J. Geophys. Res.*, **104**(D3), 3423-3431.
- Watanabe, O., J. Jouzel, S. Johnsen, F. Parrenin, H. Shoji and N. Yoshida. 2003. Homogeneous climate variability across East Antarctica over the past three glacial cycles, *Nature*, **422**, 509 - 512.
- Wolff, E.W., J.G. Paren, 1984. A two-phase model of electrical conduction in polar ice sheets, *J. Geophys. Res.*, Vol.89 (B11), 9433-9438.
- Wolff, E.W., J.C. Moore, H.B. Clausen, C.U. Hammer, J. Kipfstuhl and K. Fuhrer, 1995. Long-term changes in the acid and salt concentrations of the Greenland Ice

- Core Project ice core from electrical stratigraphy, *J. Geophys. Res.*, **100**(D8), 16249-16263.
- Wolff, E.W., J.C. Moore, H.B. Clausen and C.U. Hammer, 1997. Climatic implications of background acidity and other chemistry derived from electrical studies of the Greenland Ice Core Project ice core, *J. Geophys. Res.*, **102**(C12), 26325-26332.
- Wolff, E.W., et al., 2006. Southern Ocean sea-ice extent, productivity and iron flux over the past eight glacial cycles, *Nature*, 440, 491-496.
- Yamanouchi T., N. Hirasawa, M. Hayashi, S. Takahashi and S. Kaneto. 2003. Meteorological characteristics of Antarctic inland station, Dome Fuji, *Mem. Natl Inst. Polar Res.*, **57**, 94 - 104.
- Zhang, W.F., Y.L. He, M.S. Zhang, Z. Yin, Q. Chen, 2000. Raman scattering study on anatase TiO<sub>2</sub> nanocrystals, *J. Phys. D: Appl. Phys.*, **33**, 912-916.